



Universiteit
Leiden
The Netherlands

Low-temperature spectroscopic studies of single molecules in 3-D and on 2-D hosts

Smit, R.

Citation

Smit, R. (2024, June 12). *Low-temperature spectroscopic studies of single molecules in 3-D and on 2-D hosts*. Retrieved from <https://hdl.handle.net/1887/3762935>

Version: Publisher's Version

License: [Licence agreement concerning inclusion of doctoral thesis in the Institutional Repository of the University of Leiden](#)

Downloaded from: <https://hdl.handle.net/1887/3762935>

Note: To cite this publication please use the final published version (if applicable).

Low-temperature spectroscopic studies of single molecules in 3-D and on 2-D hosts

by Robert Smit

Low-temperature spectroscopic studies of single molecules in 3-D and on 2-D hosts

Proefschrift

ter verkrijging van
de graad van doctor aan de Universiteit Leiden,
op gezag van rector magnificus prof.dr.ir. H. Bijl,
volgens besluit van het college voor promoties
te verdedigen op woensdag 12 juni 2024
klokke 15.00 uur

door

Robert Smit

geboren te Velsen
in 1990

Promotor Prof. dr. M.A.G.J. Orrit

Co-promotor Prof. dr. ir. H.S.J. van der Zant (TU Delft)

Promotiecommissie Prof. dr. V. Sandoghdar (Max Planck Institute Erlangen)
Dr. C. Toninelli (Istituto Nazionale di Ottica)
Prof. dr. J. Aarts
Prof. dr. M. van Exter
Prof. dr. J.M. van Ruitenbeek



Universiteit
Leiden



An electronic copy of this dissertation is available at
<https://scholarlypublications.universiteitleiden.nl/>.

CONTENTS

Summary	ix
Samenvatting	xi
1. Introduction to single-molecule spectroscopy	1
1.1. Low-temperature spectroscopy	1
1.1.1. Line-narrowing spectroscopy	1
1.1.2. The 0-0 zero-phonon line (ZPL)	5
1.1.3. Inhomogeneous broadening	5
1.1.4. Nanosensing	6
1.1.5. Tunneling two-level systems	8
1.1.6. Triplet states	8
1.2. Outline of the thesis	10
2. Reverse intersystem crossing in a single perylene molecule	15
2.1. Introduction	16
2.1.1. Motivation for exploring a new host for perylene	16
2.1.2. The matrix: dibenzothiophene	17
2.2. Experimental	18
2.2.1. Preparation of the matrix	18
2.2.2. Setup	19
2.3. Results and discussion	20
2.3.1. Ensemble spectroscopy	20
2.3.2. Single-molecule studies	21
2.3.3. A model for the enhanced brightness of single molecules	24
2.4. Conclusion and Outlook	32
3. The phosphorescence of perylene	37
3.1. Introduction	38
3.1.1. Scheme for phosphorescence detection	38
3.2. Experimental	39
3.2.1. Phosphoroscope setup	39
3.3. Results and discussion	42
3.3.1. Phosphorescence of dibenzothiophene	42
3.3.2. Phosphorescence of perylene	43
3.3.3. Possible existence of multiple sites	49
3.4. Conclusion and Outlook	50

4. Single molecules in a 2-D electric field	53
4.1. Introduction	54
4.1.1. The Stark effect	54
4.2. Experimental	55
4.2.1. Crystal preparation and transfer	55
4.2.2. Preparation of quadrupole electrodes	55
4.2.3. Confocal fluorescence microscopy setup	56
4.3. Results and discussion	56
4.3.1. Line-narrowing spectroscopy	56
4.3.2. Photophysical properties of terrylene in BTBT	58
4.3.3. Determination of dipole vectors with a 2-D electric field	63
4.3.4. The transition dipole moment of terrylene	67
4.3.5. Proposed insertion sites	69
4.4. Conclusion	72
5. Hexagonal boron nitride: a universal host matrix?	77
5.1. Introduction	78
5.1.1. Hexagonal boron nitride	78
5.1.2. Low-temperature spectroscopy on surfaces	79
5.2. Experimental	80
5.2.1. Sample preparation	80
5.3. Results and discussion	80
5.3.1. Properties of the hBN flakes	80
5.3.2. Room-temperature fluorescence measurements	82
5.3.3. Low-temperature spectra of terrylene on hBN	85
5.3.4. Spectral diffusion	92
5.3.5. Resonant excitation of the 0-0 ZPL	95
5.4. Beyond terrylene: other molecules on hBN	101
5.4.1. Molecule X	101
5.4.2. Graphene Quantum Dots	102
5.5. Encapsulation of terrylene	104
5.5.1. Transfer of large area hBN	104
5.5.2. Flake-on-flake encapsulation	105
5.6. What can we learn from the literature on hBN 'defects'?	108
5.7. Conclusion and Outlook	111
6. A double-resonance experiment on perylene	119
6.1. Introduction	120
6.1.1. Experiments on triplet states	120
6.1.2. Theoretical description of a three-level system	121
6.1.3. Experimental conditions: continuous wave excitation	126
6.1.4. Pulsed excitation	128
6.2. Experimental details	129
6.3. Results and discussion	131
6.3.1. Experiments with strong reverse intersystem crossing	131
6.4. Conclusion and Outlook	135

A. Appendix 1	139
Acknowledgements	143
Curriculum Vitae	145
List of Publications	147

SUMMARY

Spectroscopic studies of fluorescent single molecules in organic condensed matter do not only provide information about the molecule itself, but also about its near environment. By suppression of phonon-induced broadening of spectral lines through cooling to low temperatures, small changes in the spectral lines' position can be uncovered in response to weak variations in local electric fields. These variations can for instance be caused by rearrangements of charges or minute changes in the crystal lattice around the molecule. Therefore, molecules are sensitive sensors for the study of physical phenomena at the nanoscale.

This sensitivity of molecules to subtle changes in their near environment only works when the spectral lines are narrow enough. At best the linewidths reach the absolute minimum, dictated by the excited state's lifetime. It is, however, not a given that every fluorescent molecule in a random organic crystal will have narrow spectral linewidths at low temperature. So far, there are in fact only very few combinations of fluorescent molecules in organic crystals that displayed narrow spectral linewidths. Then, what makes a good combination? As a rule of thumb it is important that the electronic energy levels of the crystal lattice are higher in energy than those of the embedded fluorescent molecules, in order to assure there is no loss of excitations due to transfer of energy. In the case of efficient energy transfer, there will be significant loss of fluorescence from the molecule. Furthermore, the crystal lattice must be stable at low temperature, while also a weak coupling of the fluorescent molecule to lattice vibrations is desired for. Lastly, it is empirically important that the fluorescent molecule and the molecules of the organic crystal are similar in shape and size, such that the fluorescent molecule can be well embedded into the crystal. However, a clear theory that describes what works well and what does not is absent at the moment. Moreover, even though a combination satisfies the above conditions, the crystal can still have far reaching implications on the properties of the fluorescent molecule that it incorporates.

To have more examples of combinations that give rise to narrow linewidths, we have studied two new organic crystals with the embedded fluorescent molecules perylene (Chapter 2) and terrylene (Chapter 4). In both cases, the fluorescent molecules show narrow spectral lines at low temperature, whose widths closely reach the absolute limit dictated by the lifetime of the excitation. The measured properties of the molecules are however strongly influenced by the crystal lattice around them. For instance, in Chapter 2 we report that perylene molecules in a dibenzothiophene crystal show a stronger-than-normal fluorescence signal upon strong excitation. At weak excitation perylene's fluorescence displays normal intermittency in the fluorescence signal due to transitions to a non-fluorescent state, namely the triplet state. Through stronger excitation, the time that perylene resides in the triplet state can be shortened by a few orders of magnitude, leading to a higher fluorescence output. Although this effect of reverse intersystem crossing is known, the effect had not been observed

before at liquid-helium temperatures of below 4 K. For terrylene in Chapter 4, we observed that the sensitivity of spectral lines to electric fields is enhanced. This is a consequence of the crystal lattice that surrounds the terrylene molecule and influences the charge distribution within the molecule in the ground state and excited state, and effectively creates a static dipole moment. The induced dipole moment causes terrylene to couple efficiently to electric fields and that makes this combination interesting for mapping electric fields or tracing single charges. To make the process of mapping electric fields as efficient as possible, we fabricated a chip that allowed us to measure for each molecule independently the orientation of the dipole moment, such that not only an electric field magnitude, but also field orientation can be measured.

The two described crystals in Chapter 2 and Chapter 4 possess a three-dimensional structure, but since the discovery of graphene a large number of examples of two-dimensional crystals have been explored. One of them is hexagonal boron nitride (hBN). The electronic and structural properties of hBN makes this material a promising substrate for single fluorescent molecules. We have tested this hypothesis in detail with the fluorescent molecule terrylene, as described in Chapter 5. At low temperature, we observe narrow spectral lines that are about 10-20 times wider than the absolute lifetime limit. In addition, the spectral lines show a spectral diffusion due to coupling to dynamical processes in the near environment of the molecule. Furthermore, we observed that by heating the hBN before deposition of the molecules and therefore cleaning the surface from most organic contamination, the so-called annealing, we can make the spectral lines more stable. Apart from terrylene, we also tested if other molecules could be deposited onto the hBN substrate. We tried this with large graphene molecules, which are normally difficult to incorporate into a three-dimensional crystal. Also for these molecules we observed narrow spectral lines, which gave us direct insight into the vibrational spectrum of these newly-developed molecules.

In the remaining Chapter 3 and Chapter 6 we worked on studies beyond fluorescence, namely on the light emitted from the triplet state, which is usually called phosphorescence. In Chapter 3 we used the crystal described in Chapter 2 to detect the phosphorescence of perylene. In order to be able to detect this very weak signal we created triplet excitations within the crystal itself, so that they could migrate to the limited number of perylene molecules within this crystal. With the phosphorescence spectrum as a result, we could estimate the energy of the triplet state. In Chapter 6 we continued building up an experiment that would allow us to perform a direct excitation from the ground state to the triplet state, where the energy of the laser would be scanned around a bandwidth that is given by the phosphorescence spectrum and its uncertainty. Eventually, this could give us the possibility to study excitations to the triplet state at the single-molecule level, in order to measure the quantum mechanical properties of this state, such as coupling to nuclear spins within the near environment of the molecule. This would make it possible to not only use the molecules as sensors for electric fields, but also magnetic fields.

SAMENVATTING

Spectroscopische studies aan enkele fluorescerende moleculen in organische gecondenseerde materie geven niet alleen informatie over het molecuul zelf, maar ook over zijn directe omgeving. Met name bij lage temperaturen, waarbij door trillingen geïnduceerde verbreding van de spectraallijnen onderdrukt worden, kunnen door middel van het volgen van de nauwe spectraallijnen variaties in lokale elektrische velden waargenomen worden. Deze variaties kunnen bijvoorbeeld plaatsvinden door subtiele veranderingen in de lokale ladingsverdeling of minieme veranderingen in het kristalrooster. De moleculen zijn daarom gevoelige sensoren voor het bestuderen van natuurkundige processen op nanoschaal.

Deze gevoeligheid van spectraallijnen voor minieme veranderingen in de directe omgeving van het molecuul werkt alleen wanneer deze spectraallijnen nauw genoeg zijn. In het beste geval bereiken ze een minimale lijnbreedte gedictieerd door de vervaltijd van de excitatie. Het is echter verre van het geval dat ieder fluorescerend molecuul in een willekeurig organisch materiaal deze nauwe spectraallijnen zal geven bij lage temperatuur. Tot zover zijn er maar een zeer beperkt aantal combinaties van fluorescerende moleculen in organische kristallen bekend die daadwerkelijk nauwe spectraallijnen geven. Wat maakt dan een goede combinatie? Een belangrijke vuistregel is dat de elektronische energieniveaus van het kristalrooster ver van die van het fluorescerend molecuul liggen, zodat er geen energie van de excitatie van het molecuul verloren gaat door overdracht. Dit zal leiden tot verlies van fluorescentie. Daarnaast moet het kristalrooster stabiel zijn en is een zwakke koppeling van het fluorescerende molecuul aan de roostertrillingen gewenst. Als laatste is het empirisch gezien een vereiste dat het fluorescerende molecuul en de moleculen van het kristalrooster in grootte en vorm redelijk met elkaar overeenstemmen, zodat het fluorescerende molecuul op een stabiele manier ingekapseld kan worden in het kristal. Een duidelijke wet die beschrijft wat wel en niet werkt is echter nog niet voorhanden. Bovendien kan, wanneer aan bovenstaande eisen is voldaan, het kristal nog vergaande invloed hebben op de eigenschappen van het ingekapselde fluorescerende molecuul.

Om meer voorbeelden te vinden van combinaties die nauwe spectraallijnen geven van de moleculen die er in vast zitten, heb ik in dit proefschrift twee nieuwe organische kristallen bestudeerd voor de incorporatie van de fluorescerende moleculen peryleen (hoofdstuk 2) en terryleen (hoofdstuk 4). In beide gevallen geven de fluorescerende moleculen nauwe spectraallijnen, die vrijwel de lijnbreedte bereiken die wordt gesteld door de vervaltijd van de excitatie. De gemeten eigenschappen van deze moleculen worden echter ook beïnvloed door het kristalrooster zelf. Zo vinden we in hoofdstuk 2 dat peryleen in een kristal van dibenzothiofeen bij een sterke excitatie een stabielere fluorescentie geeft dan normaliter het geval is. Bij zwakke excitatie vertoont peryleen zoals gebruikelijk lange onderbrekingen in de fluorescentie door geregeld naar een niet-fluorescerende toestand over te gaan, namelijk de triplet-toestand. Door sterke excitatie wordt echter de duur van verblijf in deze

triplet-toestand sterk verlaagd, waardoor netto meer fluorescentie uit het molecuul behaald kan worden. Hoewel dit effect bekend is van andere onderzoeken, is het nog niet eerder waargenomen bij een dergelijk lage temperatuur van onder de 4 Kelvin. Voor terryleen in hoofdstuk 4 heb ik vastgesteld dat de gevoeligheid van de spectraallijnen voor elektrische velden versterkt is. Dit blijkt het gevolg te zijn van een asymmetrische verdeling van moleculen in het kristal om terryleen heen. Het kristal beïnvloedt hierdoor de ladingsverdeling in de grondtoestand en geëxciteerde toestand van terryleen, waardoor er een effectief dipoolmoment ontstaat. Het ontstane dipoolmoment zorgt ervoor dat terryleen's spectraallijnen duidelijk verschuiven door elektrische velden en maakt dit kristal daardoor met name interessant voor het in kaart brengen van elektrische velden of het traceren van enkele ladingen. Om echter het in kaart brengen van elektrische velden zo betrouwbaar mogelijk te kunnen doen, heb ik een chip gefabriceerd waarmee voor ieder terryleen molecuul de oriëntatie van zijn dipoolmoment gemeten kan worden, zodat niet alleen de veldsterkte, maar ook de richting van het elektrische veld dat er aan koppelt bepaald kan worden.

De twee bestudeerde kristallen in hoofdstuk 2 en hoofdstuk 4 hebben een driedimensionale structuur, maar sinds de ontdekking van grafen zijn er legio voorbeelden van tweedimensionale kristallen. Één daarvan is hexagonaal boornitride (hBN). De elektronische en structurele eigenschappen van hBN maken het materiaal een veelbelovend substraat voor fluorescerende moleculen. Dit hebben we uitvoerig getest voor het fluorescerende molecuul terryleen, zoals beschreven in hoofdstuk 5. Bij lage temperatuur observeren we nauwe spectraallijnen met een breedte die ongeveer 10 à 20 keer wijder zijn dan de door de levensduur van de excitatie bepaalde limiet. Ook vertonen de spectraallijnen een diffusie door koppeling aan dynamische processen in de directe omgeving van het molecuul. Door het hBN voor de depositie van de moleculen te verhitten en daardoor te ontdoen van de meeste verontreinigingen, het zogenaamde ontharden, kunnen we de spectraallijnen stabiliseren. Naast terryleen, onderzochten we ook of het mogelijk was andere moleculen op het hBN substraat te leggen. Dit deden we met grafen quantum dots, die moeilijk te incorporeren zijn in driedimensionale kristallen. Ook hier namen we nauwe spectraallijnen waar, die mede inzicht gaven in het vibrationele spectrum van deze nieuw ontwikkelde moleculen.

In resterende hoofdstukken 3 en 6 rapporteer ik over onze studies die niet alleen het licht uit de fluorescerende toestand omvatten, namelijk de geëxciteerde singlet-toestand, maar die uit de triplet-toestand, ook wel bekend als fosforescentie. In hoofdstuk 3 gebruikte ik het onderzochte kristal uit hoofdstuk 2 om de fosforescentie van peryleene te kunnen detecteren. Om dit zwakke signaal te kunnen meten, maakten we triplet-excitaties in het kristal zelf, zodat deze konden migreren naar de beperkte hoeveelheid peryleene moleculen in het kristal. Met het fosforescentiespectrum als resultaat kon ik de energie van de triplet-toestand nauwkeurig bepalen. In hoofdstuk 6 ga ik vervolgens verder met de opbouw van een experiment waarmee vanuit de grondtoestand een directe excitatie naar de triplet-toestand gedaan zou kunnen worden. De energie van de gebruikte laser moet hierbij afgestemd worden over een bandbreedte die gegeven wordt door het fosforescentie spectrum en de onzekerheid daarin. Uiteindelijk kan dit de mogelijkheid geven om op een enkel molecuul niveau overgangen naar de triplet-toestand te kunnen meten. Zo kunnen de kwantummechanische eigenschappen van deze toestand bestudeerd worden, bijvoorbeeld die van koppeling met kernspins rondom het molecuul. Dit zou bovendien de mogelijkheid geven om de moleculen te gebruiken als sensoren voor niet alleen elektrische, maar ook magnetische velden.

1

INTRODUCTION TO SINGLE-MOLECULE SPECTROSCOPY

1.1. LOW-TEMPERATURE SPECTROSCOPY

1.1.1. LINE-NARROWING SPECTROSCOPY

The discovery of liquid helium in 1908 by Leiden's Heike Kamerlingh Onnes fueled a plethora of experiments that has led to today's status of the field of low-temperature spectroscopy. Four decades after Heike's discovery, the Russian scientist Eduard Shpol'skii observed that fluorescent aromatic molecules frozen into *n*-alkane crystals showed significant line narrowing in the absorption and emission spectra at liquid-helium temperatures, which made it possible to study the vibrational and electronic structure of molecules. His method became known as Shpol'skii spectroscopy.^{1,2} Since then, the bases of the experiments have not changed considerably. The experiments on single molecules still require a host matrix that can be doped with fluorescent molecules to induce immobilization of the otherwise rapidly-diffusing molecules. Although the spectroscopy of ensembles of molecules in solids became very common, it took a couple of decades before the signal of a single molecule was detected in a host medium, namely in 1989 by W.E. Moerner³ and 1990 by M. Orrit,⁴ both for single pentacene molecules in a *p*-terphenyl host matrix. The ensemble-average-free detection method found by Orrit is today still the dominant method, namely through their emitted fluorescence signal. Nowadays, single-molecule spectroscopy, not restricted to low temperature, has developed into a broad field of research, stretching from applications in the sub-diffraction-limited imaging of (bio)structures through super-resolution microscopy,⁵ applications in quantum optics⁶ up to employing molecules for sensing at the nanoscale (see section 1.1.4).

The fluorescent molecules that are studied in low-temperature spectroscopy generally belong to the class of polycyclic aromatic hydrocarbons, which includes molecules such

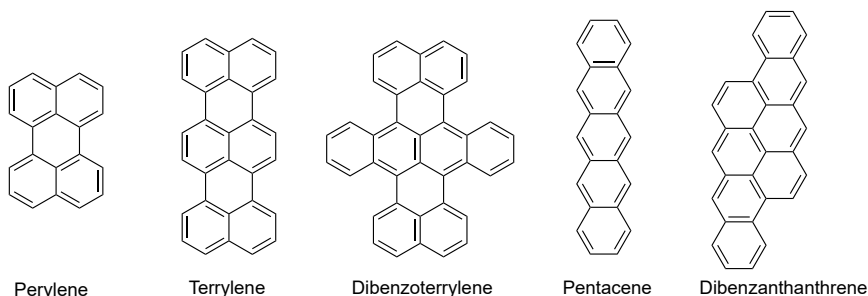


Figure 1.1.: Chemical structures of the most-used fluorescent molecules in low-temperature single-molecule spectroscopy.

as perylene, terrylene, pentacene, dibenzoterrylene and dibenzanthanthrene (see chemical structures in Figure 1.1). These molecules are typically studied inside aromatic host matrices such as anthracene, naphthalene or *p*-terphenyl. Apart from these three host matrices there are many more, but the number of guests molecules is rather limited, as they require favorable spectroscopic properties, such as a strong and stable fluorescence output. A schematic energy level structure of a guest molecule, embedded into a solid host, is depicted in Figure 1.2. First of all, there are the electronic states of the molecule, which are the singlet ground (S_0) and singlet excited state (S_1), usually separated by 1.5-3 eV, corresponding to the region of visible light. Another excited state exists in between the two singlets, which is the triplet state (T_1) and consists, as its name implies, of three sublevels with the three allowed spin quantum numbers, as total spin amounts to 1. Coupled to these electronic states are the molecular vibrations, which have energies in the order of 30-300 meV. In addition, since the molecule is in a solid medium, the electronic states also couple to low-frequency modes or phonons, which are typically low energy bands (up to 10-20 meV in bandwidth). A transition between the singlet ground and singlet excited state is highly allowed and does not violate spin or parity selection rules. Since it is highly allowed, the decay rate is also fast and typically in the order of nanoseconds. This decay can involve two processes, namely through excitation of multiple vibrational quanta, called internal conversion, or the emission of a photon, leading to fluorescence. For highly-fluorescent molecules, the radiative decay rate largely exceeds the internal conversion or non-radiative decay rate, yielding a high quantum yield of fluorescence. The molecules depicted in Figure 1.1 all have a high fluorescence quantum yield.

A transition from the singlet to the triplet is spin-forbidden, as one of the electrons has to flip a spin. However, the transition can occur with a very low probability through intersystem crossing (ISC) and is a combination of a spin-flip and internal conversion (blue and red dashed arrow in Figure 1.2). Once the molecule is in the triplet state it cannot emit fluorescence anymore and this leads to quantum jumps in the fluorescence.⁷ The blinking can for some molecules extend to a relatively long time scale of milliseconds up to seconds (see for example the triplet state of dibenzothiophene

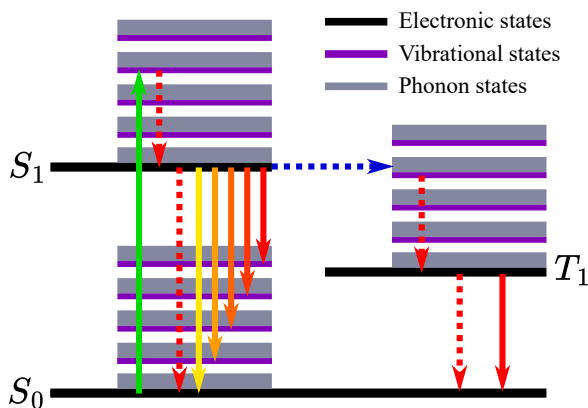


Figure 1.2.: Jablonski diagram of the three-level system of an aromatic molecule. The black bars indicate the electronic states, the purple bars the vibrational states and grey bars indicate the phonon bands. Excitation to one of the vibrational levels in the electronic excited state leads to quick dissipation of the vibrational energy. From there, the molecule can decay into one of the vibrational and/or phonon states, leading to red-shifted emission, or non-radiatively decay into the triplet state (intersystem crossing). Both pathways lead eventually back to the ground state singlet. Non-radiative processes are indicated by a dashed red arrow, intersystem crossing by a blue dashed arrow and processes involving the absorption or emission of a photon are given by a solid arrow.

in Chapter 3). The decay back to the ground state is often dominated by non-radiative decay instead of the emission of a photon, for which the latter process is called phosphorescence (see phosphorescence studies in Chapter 3). For most of the molecules in Figure 1.1, the triplet yield through intersystem crossing is very low: its probability is in the order of $10^{-6} - 10^{-7}$ per excitation. Hence, these molecules can be effectively described as two-level systems. In case the molecule remains only shortly in the triplet state, such as applies to dibenzoterrylene (around $40 \mu\text{s}$ ⁸), the overall loss of fluorescence, due to infrequent visits to the triplet state, is also limited, leading to a very stable fluorescence signal. In Chapter 2, I will show a process that can partly overcome fluorescence loss by ISC, namely through the inverse of ISC, called reverse intersystem crossing.

The fluorescence occurs by cycles through the two singlet states, shown in Figure 1.2, when continuously excited with a light source whose photon energy matches the transition's energy gap, i.e. is resonant with the transition. Resonant photons can excite the molecule to either the purely electronic state or some vibrational state. An excited vibrational state is usually short-lived, with typical lifetimes of (tens of) picoseconds⁹ and therefore we end up in the vibrational ground state of the excited singlet. It is also possible to excite to a higher singlet state, but the internal conversion would

again quickly relax the molecule back to the first excited singlet, a process known as Kasha's rule¹⁰ (with some notable exceptions, such as Azulene¹¹). After relaxation, the molecule falls back to the ground state and emits a photon. The decay can excite one (or more) vibration(s), either a molecular vibration and/or phonon, which translates into an energy loss of the photon and leads to red-shifted emission. In case the electronic states of the molecule couple weakly to the phonon states of the medium, we obtain a fluorescence emission spectrum that consists of zero-phonon lines (ZPL) with weak phonon side bands (Figure 1.3). The zero-phonon lines correspond to emission from the purely electronic transition (called the 0-0 zero-phonon line) and emission into any of the vibrational states (0-N zero-phonon line for the N-th vibrational state).

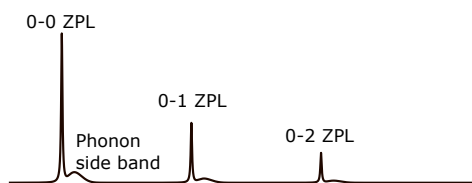


Figure 1.3.: Schematic fluorescence emission spectrum with the purely electronic transition (0-0 ZPL) and two red-shifted peaks that are due to an additional excitation of a vibrational state. Next to the ZPL peaks there are weak phonon side bands.

The intensity of the phonon side band compared to emission into the 0-0 ZPL depends on the strength of the electron-phonon coupling of the host-guest system. A careful choice of the host can give rise to weak phonon side bands in the spectrum. A typical number used for describing the intensity of the phonon side bands is the Debye-Waller factor $\alpha_{DW} = I_{ZPL}/(I_{ZPL} + I_{PSB})$. In the best host/guest systems this value can be up to 0.9. The intensity of the vibrational peaks, the 0-N ZPLs, is for the most part a property of the molecule itself and does not vary significantly by host. It relies on the coupling of the ground state vibrational wavefunction, in the excited electronic state, to the vibrational wavefunctions coupled to the ground electronic state. This is governed by overlap integrals, which are called the Franck-Condon factors. These overlap integrals determine the weights of the 0-N ZPLs in the fluorescence emission spectrum. The sum of these Franck-Condon factors compared to the intensity of the 0-0 ZPL, will be called α_{FC} . The total emission into the 0-0 ZPL as compared to the whole spectrum is the product of α_{DW} and α_{FC} , sometimes denoted as the branching ratio. In best cases, branching ratios of up to 0.55 have been found for dibenzoterrylene in *p*-terphenyl.¹² The high branching ratios for dibenzoterrylene have made this a model molecule for studies in quantum optics, which aim to employ single molecules as single photon sources, with high photon indistinguishability (scales with branching ratio).¹³ In Chapter 5, an unconventional host matrix for terrylene is studied, namely two-dimensional hexagonal boron nitride, in which it is possible to find molecules with branching ratios that exceed record values that have been found for (dibenzo)terrylene in other host matrices.

1.1.2. THE 0-0 ZERO-PHONON LINE (ZPL)

In low-temperature single-molecule spectroscopy, the focus is usually on the narrow purely-electronic transition or the 0-0 ZPL. The width of this line is determined by quantum mechanics and is derived from Heisenberg's uncertainty relation:

$$\Gamma_0 = \frac{1}{\pi T_2} = \frac{1}{2\pi T_1} + \frac{1}{\pi T_2^*}. \quad (1.1)$$

The quantity T_1 is the excited state lifetime and T_2 is the decoherence time, which is essentially the time scale over which the molecule can be considered as not interacting with the environment and is left unperturbed. At best, the decoherence time is twice T_1 , the timescale at which the excited state (spontaneously) decays. Any other interactions with the environment, that are occurring on a faster time scale than the excited state lifetime, will lead to additional decoherence. This is captured by T_2^* , which compared to twice T_1 , decreases the coherence time and broadens the linewidth. This is for example the source of linewidth broadening that occurs at higher than liquid-helium temperatures, when phonons are populated and with their motion are perturbing the environment around the molecule. However, if all decoherence mechanisms are eliminated, for example phonons are depopulated, the linewidth can reach its minimum set by equation 1.1, called the lifetime (or Fourier) limit. In the case of molecules, with lifetimes in the order of a few ns, the lifetime-limited linewidth is on the order of few tens of MHz and is presented as the full-width-at-half-maximum of a Lorentzian line shape of the resonance. For comparison, at room temperature the linewidths are typically few tens of THz.¹² Hence, the million times narrower linewidth at low temperature becomes very sensitive to quantum effects that can change the resonance's energy, caused for example through coupling to weak (static) fields. The narrow width of the 0-0 ZPL is therefore a useful tool to perform sensing at the nanoscale. In fact, 0-0 ZPLs of many molecules can be used as nano sensors at the same time, due to existence of inhomogeneous broadening.

1.1.3. INHOMOGENEOUS BROADENING

As a molecule is very sensitive to its environment in the host matrix, the inhomogeneity of the environment among many molecules can shift the electronic transition noticeably when compared to the (homogeneous) linewidth of the molecule itself. In real-world non-ideal host crystals there are always impurities, disorder and boundaries in the crystallinity, different isotopes and other mechanisms that lead to a different environment from molecule to molecule. The many molecules with lifetime-limited linewidths, but slightly shifted in energy, that can be present inside a diffraction-limited laser spot of typically 1 μm in width, lead to the formation of a much broader band of fluorescence, called the inhomogeneous band. In typical crystals this band extends from 10-100 GHz in width (see Figure 1.4b), but can be less than 1 GHz broad for extremely pure single crystals.¹⁴ By reducing the concentration of molecules, single molecules can have resonances that are isolated within the inhomogeneous distribution. With a narrow-linewidth tunable laser these molecules can be selectively excited, through their Lorentzian resonances as shown in Figure 1.4a and 1.4c.

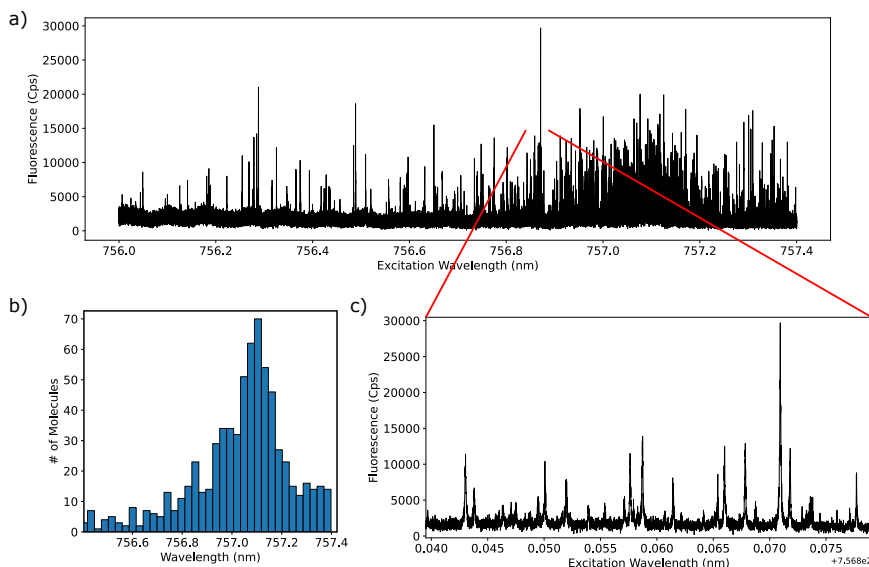


Figure 1.4.: Panel (a) shows a 1.4 nm wide scan of an excitation laser that reveals resonances of single molecules at different wavelengths, detected by the red-shifted fluorescence of dibenzoterrylene molecules in a 2,3-dibromonaphthalene crystal. In panel (b) the positions of the molecules are plotted by incidence into a histogram and reveals the inhomogeneous distribution around a center wavelength of 757.1 nm, with a width of about 0.2 nm (approximately 100 GHz). Panel (c) shows a small segment of the scan corresponding to the area between the two red lines and shows more clearly the Lorentzian line shapes of the resonances from the single molecules. The horizontal axis displays the difference in wavelength with respect to 756.8 nm.

1.1.4. NANOSENSING

Each single molecule within the inhomogeneous broadening is a potential sensor for effects on the nanoscale. One such frequently-studied effect is the Stark effect, which arises due to coupling of the electronic states with an electric field. The shift of the optical resonance itself becomes apparent when the electronic states do not shift equally, increasing or decreasing the singlet energy gap (Figure 1.5a). This difference in frequency can be expressed in the first two orders of perturbation theory as:

$$h\Delta\nu = -\Delta\vec{\mu}\cdot\vec{E} - \frac{1}{2}\vec{E}\cdot\Delta\overset{\leftrightarrow}{\alpha}\cdot\vec{E}, \quad (1.2)$$

where $\Delta\vec{\mu}$ (a vector) is the difference in permanent dipole moment between ground and excited state and likewise $\Delta\overset{\leftrightarrow}{\alpha}$ (a tensor) is the difference in polarizability between

ground and excited state. The first term is called the linear Stark effect and the second is called the quadratic Stark effect. If the molecule is centrosymmetric and the environment of the molecule leaves this centrosymmetry unchanged, then the quadratic term will be dominant. However, with the quadratic Stark effect the molecule can in most cases only shift downward in frequency, due to a higher polarizability in the excited state, and the shift typically becomes noticeable at strong electric fields of more than 10 kV/cm. That the overall shift can be very large was for instance observed for dibenzoterrylene in anthracene, where the molecules could be shifted by more than 400 GHz.¹⁵ In case the centrosymmetry is broken (see Chapter 4), the linear Stark effect can dominate in equation 1.2. Even at relatively weak electric fields, a large shift of the resonance line can be obtained. A linear Stark shift coefficient of 1.5 GHz/kVcm⁻¹ was for example observed for dibenzoterrylene in a 2,3-dibromonaphthalene matrix.¹⁶ Although this shift is strong enough to detect the field of a single charge,¹⁷ the coupling of a single charge to a single molecule remains to be demonstrated.

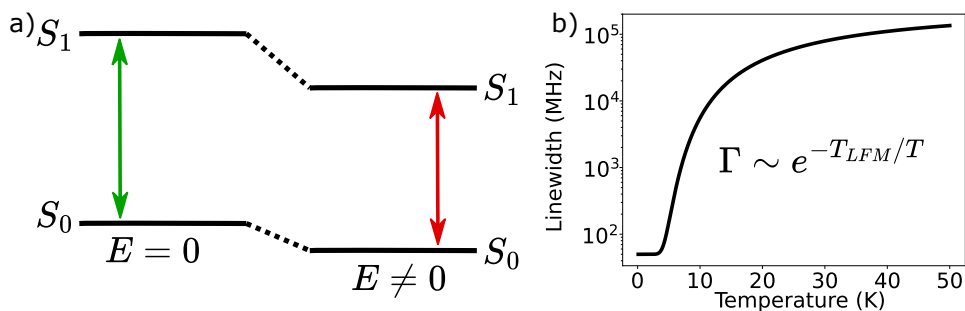


Figure 1.5.: Panel (a) shows the principle of the Stark effect. A nonzero electric field on the right side of the panel leads to shifts of both the ground and excited state singlet. When they shift by a different amount, the energy gap between the levels reduces (or may increase if a difference in dipole is present), leading to a noticeable shift of the optical resonance. Panel (b) shows schematically the line broadening observed in many organic matrices. The broadening is purely induced by decoherence through the population of (low-frequency) phonons and follows an Arrhenius law, shown in the displayed equation. The onset of the broadening is determined by phonon energies of the guest/host system, typically captured by the effective temperature of activation of low-frequency phonon modes (LFMs). This effective temperature is for organic matrices usually in the order of 40 K.¹⁸

In the past years, the Stark effect has been used for example to study the dipole-dipole coupling between two molecules whose resonances were shifted on top of each other and were spatially separated by less than 20 nm.¹⁹ In other cases, the Stark effect was used to create a single-molecule tunable light source in order to perform spectroscopy on the fine structure of a sodium vapor.²⁰ In another work it was found that in some

cases a persistent Stark shift could be obtained by using an off-resonant light source with a high intensity, likely causing separation of charges within the host crystal.²¹

Apart from the Stark effect, other sensing applications are for example strain. An experiment with an anthracene crystal mounted on top of a tuning fork displayed line broadening when the tuning fork was excited at resonance.²² A recent work showed that single molecules can also be used as sensitive thermometers at low temperature by measuring the linewidth as a function of temperature for calibration purposes.²³ The linewidths of single molecules typically broadens with an Arrhenius law due to pure phonon-induced decoherence and is shown schematically in Figure 1.5b. However, there might be additional broadening mechanisms available, namely due to tunneling two-level systems, which will be introduced in the next section and are also studied in Chapter 5.

1.1.5. TUNNELING TWO-LEVEL SYSTEMS

In some cases, molecules are sensing perturbations in their environment that are not intentionally activated. These can occur from dynamics inside the host crystal or around it (adsorbents). The model is typically described as a group of atoms tunneling between two spatial positions, the so-called tunneling two-level systems (TLSs), represented by a double well potential, schematically shown in Figure 1.6. They occur frequently in poorly-crystallized systems, such as glasses, and can explain the additional heat capacity that exists in these materials.²⁴ Even at the low temperatures that we work at, the TLSs can be active and couple to the molecule's resonance. This leads to spectral jumps and/or fast spectral diffusion,²⁵ in the case there are many of these TLSs. In well-crystallized systems, these TLSs are generally not present or minimally present. The presence of TLSs has also consequences on the typical broadening curve shown in Figure 1.5b. In general, the activation of TLSs by increasing temperature leads to additional broadening of the linewidth, in the form of a linear term added to the equation in Figure 1.5b. Apart from molecular crystals, TLSs are still subject to intensive study for quantum devices that contain superconducting qubits, as they are a primary source of decoherence for these type of qubits.²⁶

1.1.6. TRIPLET STATES

Although most of the spectroscopic measurements are performed on singlet states, the triplet states can be used as sensors as well. Triplet states are not only highly sensitive to their environment, but also to the inner structure of the molecule itself, namely its isotopic composition. As the triplet states often do not provide any measurable signal – phosphorescence is extremely weak – they have to be measured indirectly in the fluorescence signal. A common way to do that is by a scheme called optically-detected magnetic resonance (ODMR, see Figure 1.7). In order to understand this scheme we have to first consider the triplet sublevels. The three triplet sublevels are denoted as T_x , T_y and T_z .²⁷ In general, the two states T_x and T_y have similar lifetimes and are therefore difficult to separate from each other in measurements of quantum jumps in fluorescence. However, the state T_z typically has a longer lifetime. As the molecule cycles through the singlet states through continuous excitation, it naturally

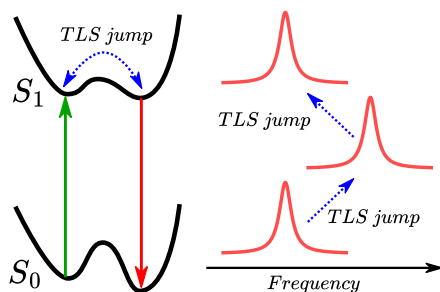


Figure 1.6.: Schematic of the standard model for tunneling two-level systems. The TLS is represented by a double-well potential of possibly two conformational states of a ‘group of atoms’. The TLS couples to the optical transition of the molecule and this may induce a jump from one to the other conformation, leading to a frequency shift of the optical transition. The TLSs are typically observed as single discrete jumps. In the case of many two-level systems discrete jumps are not observed anymore and the optical resonance will rather display spectral diffusion. Moreover, TLSs can couple to each other and a jump in one of them can induce a jump in the other.

populates these triplet sublevels levels through intersystem crossing, leading to loss of fluorescence signal. On average, the signal is therefore weaker than what it could have been without intersystem crossing. This loss is especially influenced by the longer lived T_z state and therefore shifting the triplet population from T_x or T_y to T_z will lead to more fluorescence loss. Shifting this population can be done with microwaves that are resonant with the corresponding transitions.²⁸ This resonance exists due to the zero-field splitting present between the sublevels. Moreover, the splitting can be modified by an external magnetic field due to the Zeeman effect and that makes the triplet sublevels sensitive probes for (local) magnetic fields. In addition, the triplet states couple to any other spins in their environment and most strongly to the spins present within the molecule itself. That can be for instance a nuclear spin of a carbon-13 isotope²⁹ or single hydrogen nuclei present in the molecule.³⁰ Experiments in the past showed that it was possible to even reveal at what site a particular isotope was most likely located.³¹ Moreover, the triplets are very sensitive to proton spins, for example the hydrogens that terminate the molecule. Replacing these hydrogens by deuterium reduces the hyperfine coupling thanks to the deuterium’s six times weaker gyromagnetic ratio as compared to hydrogen. As a consequence the observed resonances of the triplet in ODMR can be as narrow as 100 kHz. However, reaching lifetime-limited linewidths at standard liquid-helium temperatures is impossible, as other spins, such as the hydrogens or deuteriums and natural abundance of carbon-13 (1.1%), are always present in the molecule’s inner and outer environment. The coupling of these nuclear spins are responsible for the assymetric lineshape observed in the ODMR spectra as their random flipping narrows the energy gap between $T_y - T_z$, while broadening the

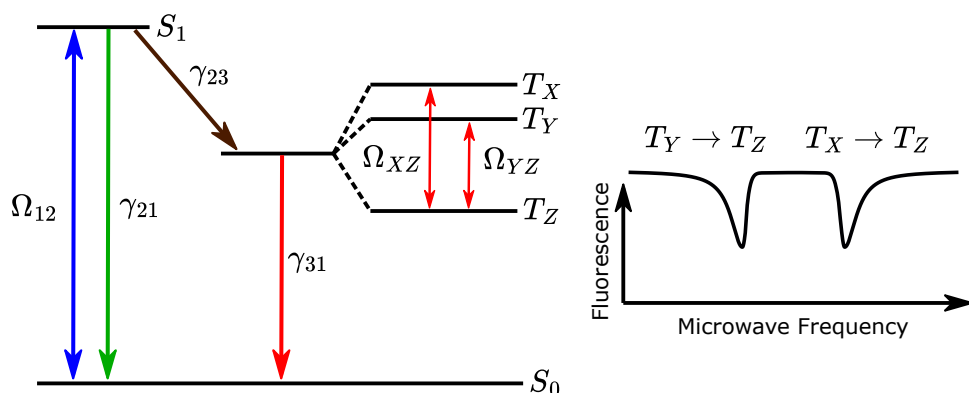


Figure 1.7.: Schematic of the optically-detected magnetic resonance experiment on a single molecule. A laser is in resonance with the singlet transition (Rabi frequency Ω_{12}) inducing fluorescence (with decay rate γ_{21}). With low probability the molecule decays into the triplet state through intersystem crossing (rate γ_{23}) and populates one of the three sublevels that are slightly apart from each other in frequency due to zero-field splitting. With a microwave that is resonant with transitions between the sublevels (with Rabi frequencies Ω_{XZ} and Ω_{YZ}), the population can be transferred from the short-lived T_x and T_y sublevels to the longer-lived T_z sublevel. The transition is observed as a decrease in the fluorescence signal, as the molecule is shelved for a longer period in the triplet state. The resonance line shapes of the electronic spin levels are asymmetric due to hyperfine interactions with nuclear spins (hydrogen, deuterium and carbon-13 atoms or other impurities).

gap between $T_x - T_z$ (see schematic in Figure 1.7b). Even though ODMR experiments allowed in-depth study of triplet states on single molecules, an all-optical approach, where the molecule is excited into the triplet from the ground state, remains to be demonstrated. In Chapter 6, I will discuss the theoretical and experimental framework of such an experiment.

1.2. OUTLINE OF THE THESIS

Although many host/guest systems have been studied in the past, the continuous exploration of new host matrices for guest molecules, such as the molecules shown in Figure 1.1, may lead to a better understanding of the modified properties of a guest molecule inside a host matrix. In these new systems, surprising effects can occasionally emerge. In the case of Chapter 2, a new host matrix is studied for (perdeuterated) perylene, namely dibenzothiophene. In this host matrix, a novel effect for single molecules was found in the form of reverse intersystem crossing, which was never observed before for (near) lifetime-limited linewidths. This effect allows for the tuning

of the photoblinking of the single molecule and the enhancement of the fluorescence signal.

The studies on this new host matrix for perylene are continued in Chapter 3. In that Chapter, we recorded the phosphorescence spectrum of perylene in order to find the energy of the triplet state. As the approximate location of the triplet state is known from the phosphorescence spectrum, an all-optical scheme, comparable to the discussed ODMR experiments, can be used to manipulate spin states in (and outside) a single molecule. The first attempts that we have performed to this end will be covered in Chapter 6.

In Chapter 4, we study another organic host matrix for single terrylene molecules. In this host matrix we observe a moderate linear Stark effect. As the mapping of electric fields, by use of the Stark effect, can be complicated by inhomogeneities in the coupling strength from molecule to molecule, we employ a method to deduce the dipole vector for each molecule individually. In addition, we use our measurements to propose a possible insertion of terrylene in the host matrix by use of quantum chemistry models.

Finally, in Chapter 5, we study an unconventional host matrix for single molecules, namely the two-dimensional material hexagonal boron nitride (hBN). With molecules on the surface of this host, we have shown for the first time that it is possible to record narrow zero-phonon lines of single molecules on a surface, rather than in the bulk of a host crystal. Our studies on hBN, which possesses much higher phonon energies than typical organic matrices, may make it in future possible to suppress linewidth broadening by temperature. Moreover, this host material may, unlike organic matrices, be applicable to a large variety of guest molecules.

REFERENCES

- (1) Shpol'skii, E. *Dokl. Akad. Nauk SSSR* **1952**, 87.
- (2) Shpol'skii, É. V. *Soviet Physics Uspekhi* **1960**, 3, 372.
- (3) Moerner, W. E.; Kador, L. *Physical Review Letters* **1989**, 62, 2535–2538.
- (4) Orrit, M.; Bernard, J. *Physical Review Letters* **1990**, 65, 2716–2719.
- (5) Reinhardt, S. C. M.; Masullo, L. A.; Baudrexel, I.; Steen, P. R.; Kowalewski, R.; Eklund, A. S.; Strauss, S.; Unterauer, E. M.; Schlichthaerle, T.; Strauss, M. T.; Klein, C.; Jungmann, R. *Nature* **2023**, 617, 711–716.
- (6) Toninelli, C.; Gerhardt, I.; Clark, A. S.; Reserbat-Plantey, A.; Götzinger, S.; Ristanović, Z.; Colautti, M.; Lombardi, P.; Major, K. D.; Deperasińska, I.; Pernice, W. H.; Koppens, F. H. L.; Kozankiewicz, B.; Gourdon, A.; Sandoghdar, V.; Orrit, M. *Nature Materials* **2021**, DOI: 10.1038/s41563-021-00987-4.
- (7) Basché, T.; Kummer, S.; Bräuchle, C. *Nature* **1995**, 373, 132–134.
- (8) Nicolet, A. A. L.; Hofmann, C.; Kol'chenko, M. A.; Kozankiewicz, B.; Orrit, M. *ChemPhysChem* **2007**, 8, 1215–1220.
- (9) Zirkelbach, J.; Mirzaei, M.; Deperasińska, I.; Kozankiewicz, B.; Gurlek, B.; Shkarin, A.; Utikal, T.; Götzinger, S.; Sandoghdar, V. *The Journal of Chemical Physics* **2022**, 156, 104301.
- (10) Kasha, M. *Discussions of the Faraday Society* **1950**, 9, 14–19.
- (11) Dunlop, D.; Ludvíková, L.; Banerjee, A.; Ottosson, H.; Slanina, T. *Journal of the American Chemical Society* **2023**, 145, 21569–21575.
- (12) Schofield, R. C.; Burdekin, P.; Fasoulakis, A.; Devanz, L.; Bogusz, D. P.; Hoggarth, R. A.; Major, K. D.; Clark, A. S. *ChemPhysChem* **2022**, 23, e202100809.
- (13) Lombardi, P.; Colautti, M.; Duquennoy, R.; Murtaza, G.; Majumder, P.; Toninelli, C. *Applied Physics Letters* **2021**, 118, 204002.
- (14) Basché, T.; Kummer, S.; Bräuchle, C. *Chemical Physics Letters* **1994**, 225, 116–123.
- (15) Schädler, K. G.; Ciancico, C.; Pazzagli, S.; Lombardi, P.; Bachtold, A.; Toninelli, C.; Reserbat-Plantey, A.; Koppens, F. H. L. *Nano Letters* **2019**, 19, 3789–3795.
- (16) Moradi, A.; Ristanović, Z.; Orrit, M.; Deperasińska, I.; Kozankiewicz, B. *ChemPhysChem* **2019**, 20, 55–61.
- (17) Faez, S.; van der Molen, S. J.; Orrit, M. *Physical Review B* **2014**, 90, 205405.
- (18) Clear, C.; Schofield, R. C.; Major, K. D.; Iles-Smith, J.; Clark, A. S.; McCutcheon, D. P. S. *Physical Review Letters* **2020**, 124, 153602.

- (19) Trebbia, J.-B.; Deplano, Q.; Tamarat, P.; Lounis, B. *Nature Communications* **2022**, *13*, 2962.
- (20) Kiefer, W.; Rezai, M.; Wrachtrup, J.; Gerhardt, I. *Applied Physics B* **2016**, *122*, 38.
- (21) Colautti, M.; Piccioli, F. S.; Ristanović, Z.; Lombardi, P.; Moradi, A.; Adhikari, S.; Deperasinska, I.; Kozankiewicz, B.; Orrit, M.; Toninelli, C. *ACS Nano* **2020**, *14*, 13584–13592.
- (22) Tian, Y.; Navarro, P.; Orrit, M. *Physical Review Letters* **2014**, *113*, 135505.
- (23) Estes, V.; Duquennoy, R.; Ng, R.; Colautti, M.; Lombardi, P.; Arregui, G.; Chavez-Angel, E.; Sotomayor-Torres, C.; Garcia, P.; Hilke, M.; Toninelli, C. *PRX Quantum* **2023**, *4*, 040314.
- (24) Phillips, W. A. *Reports on Progress in Physics* **1987**, *50*, 1657.
- (25) Fleury, L.; Zumbusch, A.; Orrit, M.; Brown, R.; Bernard, J. *Journal of Luminescence* **1993**, *56*, 15–28.
- (26) De Graaf, S. E.; Faoro, L.; Ioffe, L. B.; Mahashabde, S.; Burnett, J. J.; Lindström, T.; Kubatkin, S. E.; Danilov, A. V.; Tzalenchuk, A. Y. *Science Advances* **2020**, *6*, eabc5055.
- (27) Lawetz, V.; Orlandi, G.; Siebrand, W. *The Journal of Chemical Physics* **1972**, *56*, 4058–4072.
- (28) Schmidt, J.; Veeman, W. S.; van der Waals, J. H. *Chemical Physics Letters* **1969**, *4*, 341–346.
- (29) Köhler, J.; Brouwer, A. C.; Groenen, E. J.; Schmidt, J. *Science (New York, N.Y.)* **1995**, *268*, 1457–1460.
- (30) Wrachtrup, J.; Gruber, A.; Fleury, L.; von Borczyskowski, C. *Chemical Physics Letters* **1997**, *267*, 179–185.
- (31) Brouwer, A. C. J.; Köhler, J.; Groenen, E. J. J.; Schmidt, J. *The Journal of Chemical Physics* **1996**, *105*, 2212–2222.

2

REVERSE INTERSYSTEM CROSSING IN A SINGLE PERYLENE MOLECULE

A novel host matrix for perylene, namely dibenzothiophene, is treated in this chapter. Our low-temperature studies on single perylene molecules in this matrix reveal near lifetime-limited emission with a reasonable long-term stability of their spectral lines. Moreover, the resonance fluorescence of perylene molecules reveals an effect that was not observed before at liquid-helium temperatures and with such narrow resonances. Instead of constant depopulation rates for the triplet states, the rates scale linearly with the light intensity of the probe laser, an effect known as reverse intersystem crossing. In this chapter, the observed anomalous behavior of fluorescence blinking will be explained using a model that incorporates all the relevant intramolecular rates. Finally, we show that reverse intersystem crossing helps to improve the stability of the fluorescence signal, which makes perylene competitive in terms of brightness with molecules that are fluorescing more stably in general and thus better approximate a two-level system, such as terrylene and dibenzoterrylene.

Parts of this chapter have been published in: R. Smit, Z. Ristanovic, B. Kozankiewicz and M. Orrit, 'Reverse Intersystem Crossing of Single Deuterated Perylene Molecules in a Dibenzothiophene Matrix', ChemPhysChem 2022, 23, e202100679

2.1. INTRODUCTION

2.1.1. MOTIVATION FOR EXPLORING A NEW HOST FOR PERYLENE

Studies of perylene in single-molecule spectroscopy have been largely overshadowed by much brighter emitters, such as terrylene and dibenzoterrylene, that behave more closely to two-level systems. Although perylene has an equally short fluorescence lifetime and an even higher radiative quantum yield than for instance dibenzoterrylene (DBT),¹ the fluorescence signal from a single molecule is less stable due to long-lived triplet states, having extended lifetimes by up to two or three orders of magnitude longer than those of DBT.² It is, however, the triplet state and specifically its energy that served as the motivation for this study. If the energy of the triplet state is known, a resonant excitation of the triplet would make it possible to prepare the molecule, on demand, in a state that carries spin, unlike the spin-less singlet states. These studies could be done on a single molecule level, avoiding ensemble-averaging.

There are several methods to acquire the position of the triplet state, for example by recording an absorption spectrum of the $S_0 \rightarrow T_1$ transition or by recording the phosphorescence resulting from intersystem crossing, both performed in ensembles. Several of these attempts have been pursued in our group, for perylene in host matrices, but were unsuccessful. The difficulty of these methods lies respectively in the weak absorption of the $S_0 \rightarrow T_1$ transition and in the low triplet yield of the perylene molecule by intersystem crossing, which is about 10^{-6} .³ In other words, 1 million of photons absorbed by a perylene molecule will likely produce a single triplet. Only a tiny fraction of these triplets will actually emit a photon due to a strong internal conversion. This internal conversion rate scales down exponentially with the triplet energy gap, according to the energy gap law.⁴ As perylene is the bluest of emitters among the list of terrylene, dibenzoterrylene and others, the internal conversion rate is expected to be the lowest. Considering that we work with fully-deuterated perylene, denoted as perylene-d12, the internal conversion rate is expected to decrease even slightly more,⁵ thanks to a weaker vibrationally-assisted relaxation via C-D vibrations, which are about a factor $\sqrt{2}$ lower in energy than C-H vibrations. The afore-mentioned reasons, together with the narrow and relatively stable emission found for perylene at low temperature in some matrices,^{3,6,7} rationalizes the choice of perylene for a search for the triplet state's location. However, despite the lower internal conversion, estimates, based on a radiative lifetime in the order of 30 s^{8,9} and a triplet lifetime of a few ms,³ still put the radiative quantum yield of the triplet state of perylene at a low 10^{-4} . Hence, 10 billion photons absorbed by the singlet of perylene will likely produce a single phosphorescence photon. Only a small fraction of these photons will actually be detected in our setup. In this chapter, we will show that the detection efficiency of our setup is in the order of 10^{-3} . Finally, a whopping 10 trillion cycles through the singlet manifold would likely give us only one detected phosphorescence photon! This extremely low signal of the phosphorescence makes it exceedingly difficult to detect. Hence, we need some alternative method that particularly bypasses the low triplet yield through intersystem crossing of perylene itself.

We searched for a host matrix that features an increased intersystem crossing rate and hence a higher triplet yield. Yet, these properties must not interfere with measurements

on the guest molecule itself. A first requirement is that the host's singlet excited state must be higher in energy than the singlet excited state of perylene, in order to avoid energy transfer to the host. Studies have also confirmed that a triplet state with a lower energy than the excited singlet state of the guest can lead to intermolecular intersystem crossing, and as a consequence can make fluorescence of a single molecule too weak to detect.¹⁰ Actually, this mechanism, which leads to an enhanced triplet yield of the guest molecules, is at the basis of the only known matrix (anthracene) where phosphorescence of perylene impurities was detected.⁶ However, the fluorescence signal of a single molecule was consequently too weak to detect. The second requirement is therefore that the host's triplet state should be higher in energy than perylene's singlet excited state. These two conditions for a host gave us a possible candidate: dibenzothiophene. This chapter will focus on the photophysical studies of perylene in this novel dibenzothiophene matrix, while the follow-up studies on the phosphorescence of perylene in this new matrix will be discussed in the next chapter.

2.1.2. THE MATRIX: DIBENZOTHIOPHENE

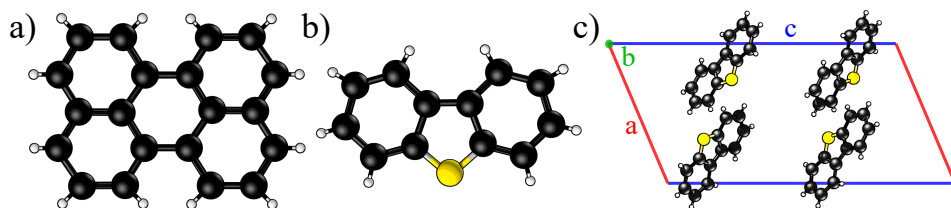


Figure 2.1.: Panel (a) shows the structure of perylene and panel (b) the structure of dibenzothiophene, along with the unit cell of dibenzothiophene in panel (c). The unit cell belongs to the $P_{21/c}$ space group. The insertion of perylene into the dibenzothiophene host matrix is unknown, but the relative sizes of the molecules would likely not permit the removal of more than two dibenzothiophene molecules per perylene guest molecule.

Dibenzothiophene is an organosulfur aromatic compound that consists of two fused benzene rings around a central thiophene unit (Figure 2.1b). Compared to the structurally similar compounds of fluorene, carbazole and dibenzofuran, the dibenzothiophene molecule was found to have a significantly higher ISC rate, which is likely caused by an enhanced spin-orbit coupling due to a heavy-atom effect of the central sulfur atom.¹¹ The electronic properties of dibenzothiophene have been studied before and it was found that the singlet transition lies around $29,923\text{ cm}^{-1}$ (334.3 nm) and the transition to the triplet at $24,292\text{ cm}^{-1}$ (411.8 nm).¹² This means that both excited states of dibenzothiophene lie well above the singlet excited state of perylene, which was found to be around $446 \pm 2\text{ nm}$ in *o*-DCB.³ In addition, the sizes of perylene and dibenzothiophene do not differ by much, which might make a stable site for insertion into the crystal lattice possible. Moreover, both perylene and dibenzothiophene crystallize according to the same space group: $P_{21/c}$. Despite their similarities, no

previous studies of dibenzothiophene as a host matrix for single molecules have been performed before.

2

2.2. EXPERIMENTAL

2.2.1. PREPARATION OF THE MATRIX

Dibenzothiophene was obtained commercially from Alfa Aesar, with a documented purity of about 98%. This starting material was further purified using zone-refining, performed by prof. Boleslaw Kozankiewicz from the Institute of Physics in Warsaw. After a few weeks, colored impurities gathered at the end of the zone-refining tube. Despite that some (colored) impurities were removed, it is known that impurities with a very similar structure to dibenzothiophene, such as phenanthrene, are difficult to remove with zone-refining.¹³ A more detailed study of some of the impurities that we found in the zone-refined dibenzothiophene are shown in Chapter 3, which were detected with high sensitivity through their phosphorescence signal.

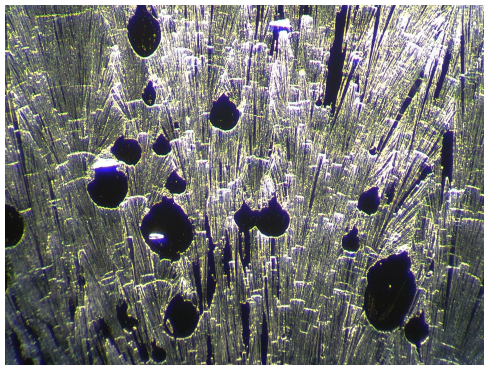


Figure 2.2.: Layer of freeze-quenched polycrystalline dibenzothiophene on a glass cover slip. The preferred crystallization is in the form of needles.

Perylene (Sigma-Aldrich, 98%), in fully-deuterated form, denoted as perylene-d₁₂, was diluted in toluene (Acros Organics, 99.85%). For bulk spectroscopy, a concentration of 10-100 ppm was prepared and for single-molecule experiments the concentration was further decreased to 0.1-10 ppb. Toluene would not be part of the final matrix, but would merely act as a transfer solvent and for a proper control of the concentration and solubility of the guest molecules. The perylene-d₁₂/toluene mixture was pipetted into molten dibenzothiophene (melting point of around 100 °C), while the toluene was allowed to evaporate from the hot liquid (boiling point 110.6 °C). For bulk spectroscopy, the liquid was subsequently sucked into a heated square borosilicate capillary (VitroTubes, 1 mm ID and 0.2 mm walls) and quickly immersed into liquid nitrogen to avoid expulsion of perylene-d₁₂ from the matrix. For single-molecule measurements, the liquid is pressed between two glass slides to form a thin layer and is again freeze-quenched in liquid nitrogen. The result of this preparation is shown in

Figure 2.2, where a dense configuration of dibenzothiophene needle-shaped crystals can be observed.

2.2.2. SETUP

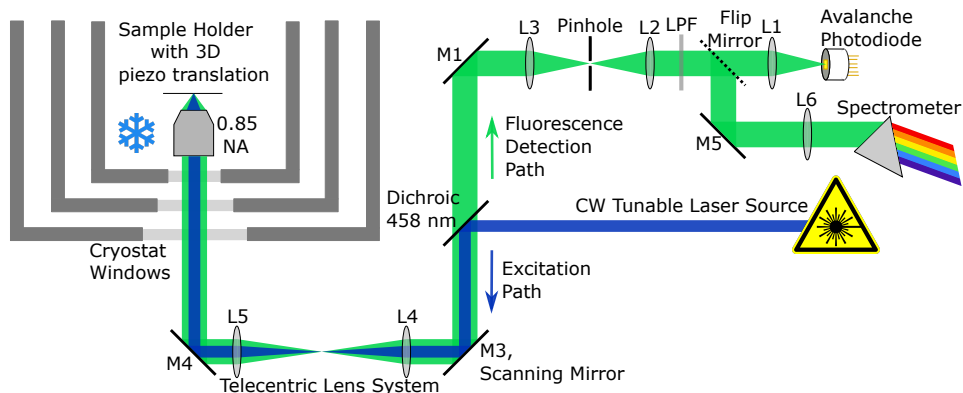


Figure 2.3.: Schematic of the confocal microscope setup used in the experiments. A dichroic separates excitation light from fluorescence and a flip mirror can switch from single-photon detection to the acquisition of spectra.

The samples were measured in a liquid helium flow cryostat (Janis, SVT-200-5) that can reach a working temperature of approximately 1.4 K. With an objective (0.85 NA, Edmund Optics) immersed in liquid helium, the cryostat forms part of a home-built confocal microscope (see schematic in Figure 2.3). A Ti:sapphire laser (M-squared SolsTiS) in combination with a frequency-doubling module (M-squared ECD-X) was used as a narrow bandwidth (< 1 MHz) tunable excitation source, operating in the 440–460 nm range. The output wavelength is monitored continuously with a wavemeter (High Finesse WS6-200), with a resolution of a few MHz. A dichroic mirror (Semrock, FF458-Di02-25x36) is used to separate fluorescence from the excitation light and further spectral filtering is done with a long-pass filter (Chroma, ET460lp). For the full recording of the emission spectrum of perylene-d12 we used a beam splitter instead of a dichroic mirror and made use of a 450 nm long-pass filter (Thor Labs, FEL0450) to remove the excitation light. The laser beam was scanned over the sample by a scanning mirror (Newport, FSM-300-01) and fluorescence was detected by an avalanche photodiode (Excelitas, SPCM-AQRH-16). Fluorescence spectra were recorded with a Horiba iHR320 spectrometer coupled to a liquid-nitrogen-cooled Symphony II CCD detector. The excitation intensity was measured with a power meter (Newport 1830-C), before the laser beam entered the cryostat.

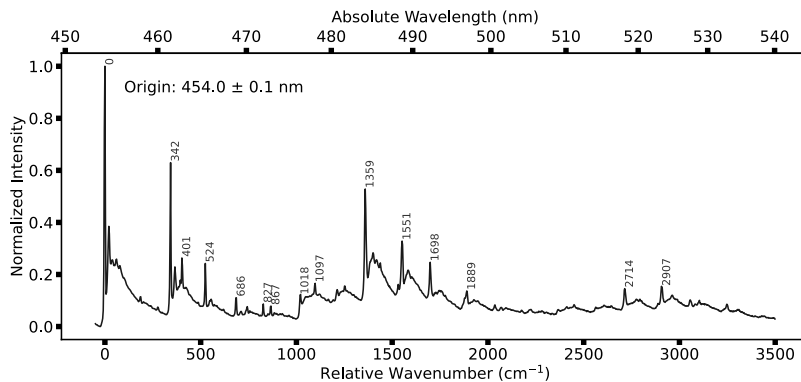


Figure 2.4.: Normalized fluorescence spectrum of an ensemble of perylene-d12 molecules in a dibenzothiophene crystal, measured at a temperature of 1.4 K. The origin of the emission is from the 0-0 zero-phonon line at 454.0 ± 0.1 nm. Some of the most prominent vibrational peaks are annotated. The excitation wavelength was 447.2 nm.

2.3. RESULTS AND DISCUSSION

2.3.1. ENSEMBLE SPECTROSCOPY

In the first experiment, we illuminated a capillary with perylene-d12-doped dibenzothiophene crystals to observe if there was fluorescence line-narrowing in the emission spectrum at low temperature. The recorded ensemble emission spectrum of perylene-d12 in the matrix, excited with a wavelength of 447.2 nm, is shown in Figure 2.4 and displays a narrow distribution of 0-0 zero-phonon lines (the peak at the origin of the spectrum), together with the vibrational fingerprint that can be attributed to perylene-d12, whose spectrum has been well-studied.^{14–17} The origin of the main site is located at 22033 ± 5 cm^{-1} (or 454.0 ± 0.1 nm) with an inhomogeneous broadening of approximately 10 ± 1 cm^{-1} . Only a single spectroscopic site is found in the emission spectrum at the chosen excitation wavelength. Other sites may exist, although none are visible in the spectrum of Figure 2.4, probably because these sites have no vibronic transition that coincides with the chosen excitation wavelength. The tunable range of the second harmonic, generated by the laser crystal, is merely 1 nm and for extended scans the angle of the crystal has to be readjusted manually. We also excited the host/guest matrix with a 405 nm laser, but the spectrum is complicated by an overlap with the phosphorescence spectrum of dibenzothiophene and possibly other impurities. Hence, we could not formally identify any other sites. However, with a tunable diode laser, used in the experiments of Chapter 3, we could identify close-by spectroscopic sites and they will be presented in the corresponding chapter.

As the main spectroscopic site is known from the ensemble spectrum in Figure 2.4, single molecules in the inhomogeneous band can be excited selectively with a

narrowband tunable laser and studied one-by-one.

2.3.2. SINGLE-MOLECULE STUDIES

The laser, used for ensemble spectroscopy, is also used for a resonant excitation of single molecules. However, we use a different crystal for the generation of the second harmonic, adjusted for the region around 454 nm. The confocal fluorescence images of thin crystals, shown in Figure 2.5a and 2.5b, show why it is necessary to freeze-quench the molten host molecules when doped with guest molecules. In samples that were freeze-quenched, the crystals showed a homogeneous distribution of isolated fluorescent spots (Figure 2.5b), whose activation strongly depends on the excitation frequency. In non-freeze-quenched samples, the fluorescence concentrates at the boundary of the crystals (Figure 2.5a), while the fluorescence signal itself was activated by a wider range of laser frequencies. The slow freezing of molten dibenzothiophene leads to the expulsion of perylene from the matrix, which is of course at the very core of the zone-refining technique, used to extract impurities.

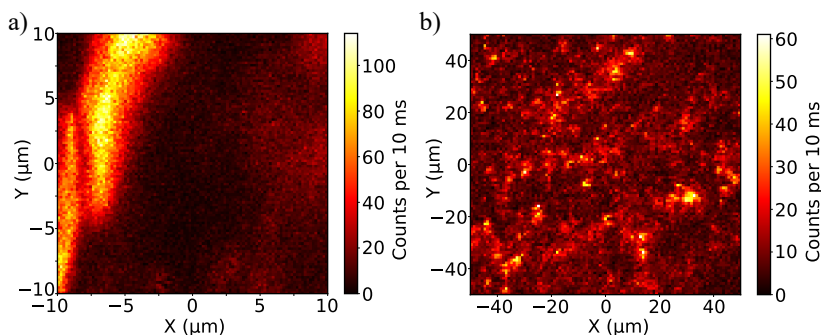


Figure 2.5.: Confocal fluorescence images that show the difference between non freeze-quenched crystals in panel (a) and freeze-quenched crystals in panel (b). In rapidly-frozen crystals, the expulsion of perylene to the boundaries of the crystals is prevented. The quenching results in a homogeneous distribution of molecules, visible as isolated spots. The concentration in both samples is relatively high and the measurement temperature is around 1.4 K.

The sample in Figure 2.5b is still very crowded with single molecules, which leads to a relatively strong background signal, while many molecules are observed in a scan range of 10 GHz. A further reduction of the concentration led to well-isolated single molecules in frequency space. This isolation made it possible to excite a single molecule using a (broad) vibronic transition around 447.1 nm (at the combined energy of the 0-0 ZPL and of the 344 cm^{-1} stretching mode) and record a full emission spectrum, as shown in Figure 2.6. From the ratio of the intensity of the 0-0 ZPL as compared to the combined intensity of the 0-0 ZPL and the phonon-side band (PSB), excluding vibrational peaks, we estimate the Debye-Waller factor to be around 0.40 ± 0.05 .

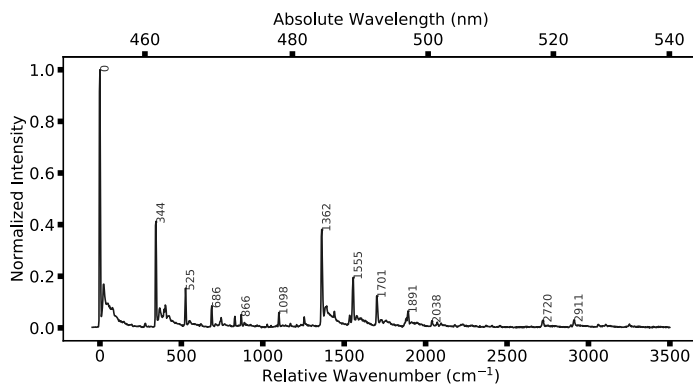


Figure 2.6.: Emission spectrum of a single molecule excited at 447.1 nm by a vibronic transition, given by the energy of the 0-0 ZPL and the 344 cm^{-1} vibration. The spectrum is recorded with a 1200 lines/mm grating and 0.1 mm slit size.

With a resonant excitation of the 0-0 ZPL, we followed single molecules for longer time to observe their frequency stability. Three examples of these time-resolved excitation spectra are shown in Figure 2.7. Here, the background is close to the dark count level of the detector, as the concentration of molecules was very low (1 per 10 GHz range around the center of the inhomogeneous band). At higher concentrations (>1 molecule per 10 GHz around the center of the inhomogeneous band) of molecules, the background was substantially stronger, which is likely fueled by the excitation of ill-inserted and/or spectrally-diffusing molecules. Nonetheless, apart from some small amount of spectral diffusion in Figure 2.7c, most molecules are in general stable. The inhomogeneous coloring of each trace does reveal a strong photoblinking of the fluorescence, related to intersystem crossing to the relatively long-lived triplet state.

For the remainder of this paragraph, the single-molecule measurements will focus on a model molecule for the studied system, denoted as molecule M1. At a low energy excitation, avoiding power-broadening of the spectral line, the linewidth of molecule M1 is found to be around 58 MHz, which is obtained from the Lorentzian fit to the data in Figure 2.8a. Note that the data points in Figure 2.8a are an average of ten single excitation spectra and thus laser jitter and/or spectral diffusion might contribute to the broadening of the measured linewidth. The averaging was necessary to obtain a clear Lorentzian distribution, as single excitation spectra displayed random shapes due to stochastic intersystem crossing, where dwell times in the triplet state could easily exceed the integration time of about 10 ms. The same averaging procedure was followed for the molecule excited at a wide range of laser intensities. The extracted linewidths show the expected broadening with excitation intensity and from the equation in Figure 2.8b, the saturation intensity could be extracted, and was estimated to $22 \pm 3 \text{ W/cm}^2$ at the focal point.

The homogeneous linewidth of 58 MHz, about the narrowest linewidth found in this

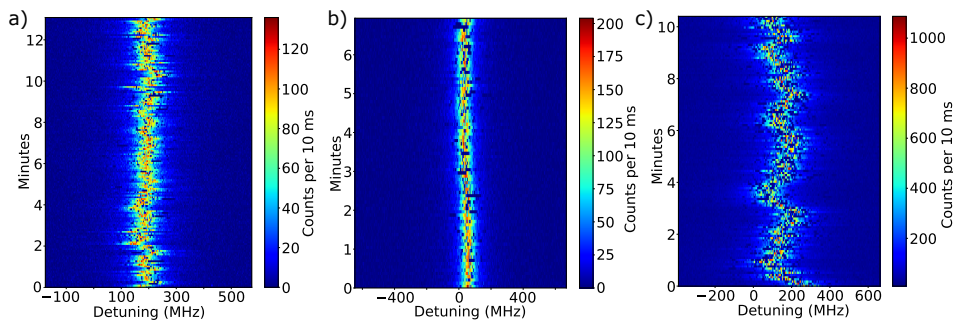


Figure 2.7.: Time-resolved excitation spectra of the 0-0 ZPL of single perylene-d12 molecules. The laser wavelength was monitored continuously using the wavemeter and laser drifts have been corrected, but some jitter in the laser's wavelength might still be present. The molecules show different degrees of stability. The blinking of fluorescence is also clear due to the chosen color scale.

matrix, is slightly broader than what was found for perylene in the Shpol'skii matrix *n*-nonane, where the distribution of linewidths revealed linewidths down to 28 MHz. However, the linewidths are very similar to observations for perylene in *o*-DCB.³ To determine whether these linewidths were limited by the lifetime of the excited state, we recorded fluorescence decays under a pulsed excitation at 392 nm. These decays were measured for both hydrogenated perylene (Figure 2.9a) and perdeuterated perylene (Figure 2.9b). The difference in the resulting lifetimes is striking, showcasing an increase of the lifetime by about one quarter when all hydrogens are replaced by deuterons. The difference might be explained by a weaker internal conversion, assisted by reduced Franck-Condon factors due to the lower energy of the CD-vibrations as compared to the CH-vibrations.⁹ The fluorescence lifetime for perylene-d12 points to a lifetime-limited linewidth of 34.3 ± 0.5 MHz, which is indeed smaller than the measured 58 MHz. Hence, there might be some broadening due to dephasing and/or spectral diffusion, while, as mentioned before, also laser jitter might contribute to the broadening.

Measurements at high excitation intensities reveal anomalous behavior. Close to the saturation intensity of the molecule, the photoblinking of the fluorescence is clearly resolved. Without the afore-mentioned averaging, a single excitation spectrum would show many events where the molecule turned dark, as can be observed in Figure 2.10a, where many points lie between background level and the border of a Lorentzian profile. At high laser intensities, beyond the saturation intensity, the fluorescence signal in Figure 2.10b stabilizes without a single point dropping to background level. As the molecule is saturated, the rate of intersystem crossing should likewise saturate and a lot of blinking should be observed. A possible explanation for the reduced blinking times is reverse intersystem crossing (abbreviated as rISC). In the next paragraph we will use a model that includes rISC to explain the light-induced reduction of the triplet lifetimes. With

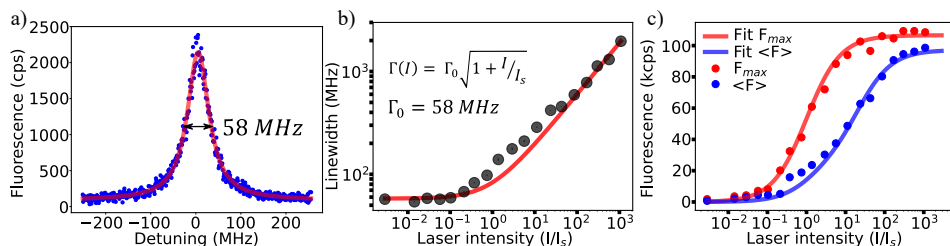


Figure 2.8.: Measurements of molecule M1. Panel (a) shows the averaged line shape of 10 single excitation spectra of a single molecule at 2% of the saturation intensity. The data points have been fitted to a Lorentzian distribution and this yields a full-width-at-half-maximum or homogeneous linewidth of 58 MHz. Panel (b) shows the measured linewidths at a broad range of laser intensities to observe the power broadening of the linewidth. The saturation power that was acquired from the fit is $0.35 \pm 0.04 \mu\text{W}$, which leads, when taking into account additional power losses before the light enters the objective, to a saturation intensity of $22 \pm 3 \text{ W/cm}^2$. Strong blinking of the molecules' fluorescence at middle-range powers attributed to an increased uncertainty of the Lorentzian fits, that together with additional broadening due to laser jitter and/or spectral diffusion, probably caused these points to deviate from the fitted line. Panel (c) shows red data points that represent the maximum fluorescence intensity recorded from the molecule at the specified laser intensity, in the cases the fluorescence signal was not or negligibly affected by triplet blinking. The blue data points do take the stochastic intersystem crossing into account and thus represents the average fluorescence signal at a given excitation intensity. The fits will be discussed in paragraph 2.3.3.

this model we will also explain the not yet discussed fit to Figure 2.8c, where it can be noticed that the average fluorescence signal approaches the maximum fluorescence signal that can be obtained from the molecule in case there would be no blinking within the measured time interval.

2.3.3. A MODEL FOR THE ENHANCED BRIGHTNESS OF SINGLE MOLECULES

Clear evidence of a reduced triplet lifetime is shown in fluorescence time traces, such as in Figure 2.11. The same time period, but acquired with a large difference in laser intensity yields totally different patterns in the fluorescence blinking. While at low laser intensities compared to the saturation intensity, the pattern shows long periods where the molecule remains dark, a higher laser intensity leads to strongly reduced dark times. In many cases the molecule returns to the bright state within the integration time of 1 ms.

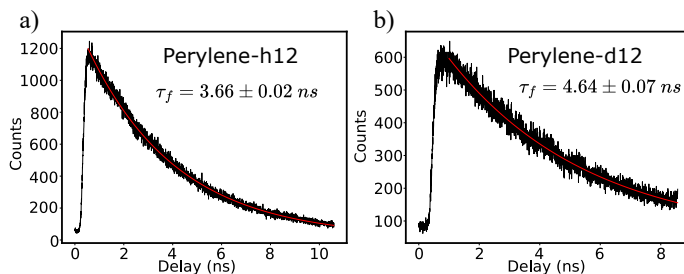


Figure 2.9.: Fluorescence decays of ensembles of perylene-h12 in panel (a) and perylene-d12 in panel (b), both recorded in a dibenzothiophene matrix. The data points fit well to a single exponential decay in both measurements. The excitation wavelength is 392 nm. The data was recorded by prof. Boleslaw Kozankiewicz from the Institute of Physics in Warsaw.

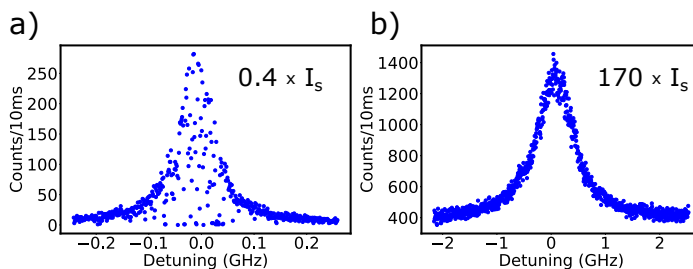


Figure 2.10.: Single excitation spectra of the 0-0 ZPL of molecule M1 at 40% of the saturation intensity in panel (a) and 170 times the saturation intensity in panel (b). Note that in (a) the shape of the Lorentzian is visible at the outer borders, but many points drop below this outer border and some all the way to the background, a signature of blinking. The highest point represents a red data point in Figure 2.8c.

The dynamics of fluorescence blinking can be studied in two ways. If the fluorescence signal is strong enough compared to the background, a threshold level between the on and off state can be determined. The on and off times can then be distributed and fitted to exponential decay(s).¹⁸ The characteristic off time(s) will equal the triplet lifetime(s), while the on times will change with the level of saturation of the molecule. However, at low excitation intensities the signal-to-background ratio is typically very low and at high excitation intensities the background can be strong. In addition, the reduced triplet lifetimes make it harder to distinguish between on and off periods. A powerful tool that overcomes these problems is the autocorrelation of the fluorescence signal, taken at resonance with the 0-0 zero-phonon line. The autocorrelation of the resonance-fluorescence signal can be equated to the second-order intensity correlation function as follows:

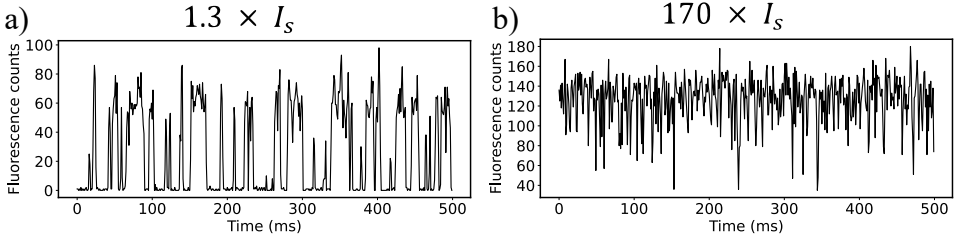


Figure 2.11.: Fluorescence time traces of molecule M1 over a time span of 500 ms, with a 1 ms integration time per point. A significant change in blinking dynamics can be observed between panel (a) representing a low excitation intensity and panel (b) a high excitation intensity. The reduction in dark times can be explained by a change in the triplet lifetime due to reverse intersystem crossing.

$$g^{(2)}(\tau) = \frac{\langle I(t)I(t+\tau) \rangle}{\langle I(t) \rangle^2} \quad (2.1)$$

Time series, such as in Figure 2.11, were recorded with an integration time of 10 μ s for a period of 60 s up to 120 s. The length of the series was enough to have a relatively good signal to noise ratio in the autocorrelations, while restricting file sizes to 100-200 MB. The recorded time series were autocorrelated for time delays up to 1 second. This resulted in an exponentially decaying time dependence (Figure 2.12).

From the rate equations and their solutions (see reference³) we fitted the autocorrelation $g^{(2)}(\tau)$ in equation 2.1 to:

$$g^{(2)}(\tau) = C_0 + C_1 e^{-\lambda_1 \tau} + C_2 e^{-\lambda_2 \tau} \quad (2.2)$$

The fitting of both exponentials worked well for autocorrelations obtained at low excitation intensities, although the contrast of the long-lived decay is very low compared to the short-lived decay (Figure 2.12a). With laser intensities above saturation it becomes increasingly difficult to fit to a combination of two exponential decays and at the highest intensities, the autocorrelation fits very well to a single exponential decay, as in Figure 2.12c. The parameter C_0 is in most cases very close to 1, which indicates that the autocorrelation is not significantly affected by stray correlations. However, mechanical vibrations of the vacuum pump coupling to the sample holder left a fingerprint in the autocorrelation, with a characteristic frequency of 100 Hz. To correct for this, we measured an autocorrelation of a background signal and divided out these contributions to the autocorrelation functions in equation 2.2. This correction has been done already for the autocorrelation curves in Figure 2.12. Apart from corrections arising from these mechanical vibrations in our setup, the contributions from the background need to be corrected as well, which affects the contrasts of the exponential decays.¹⁹ Corrections for the background-to-signal ratio can be taken into account by multiplying the individual

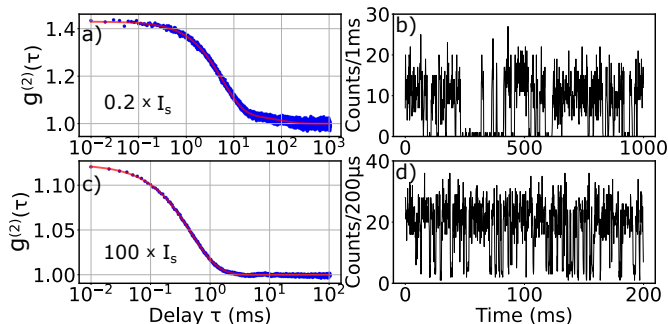


Figure 2.12.: Fits of the autocorrelation curves (left) and parts of the corresponding fluorescence time traces (right) of molecule M1 at a low excitation intensity of 20% of the saturation intensity in panel (a) and panel (b) and 100 times the saturation intensity in panel (c) and (d). Note that the time scales in (a) and (c) differ, while also the integration time for (b) is 1 ms and 200 μ s for (d). In addition, the fit in (a) is a sum of two exponentials, while (c) was fitted to a single exponential decay.

fits to equation 2.2 through a prefactor: $(1 + \frac{B}{S})^2$, where B is the background signal compared to the molecules' signal S . Hence, for each excitation intensity this $\frac{B}{S}$ ratio has to be determined. In general, the background never exceeded 40% of the total signal for the highest excitation intensity that was used in the experiments.

The existence of two well-separated exponential decays at low excitation intensities points to a distinguishability of two out of three triplet substates. Typically, the short-lived decays are attributed to the T_x and T_y substates, while the longer-lived decay is assigned to the T_z state.²⁰ The rate equations assign two rates for each of the two sets of substates - which we will distinguish with the labels xy and z - namely a population rate and a depopulation rate. The population rate of the triplet states is determined by the intersystem crossing rate and will be denoted as (k_{23}^{xy}, k_{23}^z) , see diagram in Figure 2.13. Since the population rate of the triplet state is affected by the level of saturation of the molecule, we will denote these as the effective ISC rates. These rates can then be expressed in terms of the intrinsic ISC rates $(\gamma_{23}^{xy}, \gamma_{23}^z)$ and of the excitation intensity as:

$$(k_{23}^{xy}(I), k_{23}^z(I)) = \frac{(\gamma_{23}^{xy}, \gamma_{23}^z)}{2} \frac{I}{1 + \frac{I}{I_s}}. \quad (2.3)$$

A populated triplet state will also be depopulated with a characteristic rate, which will be denoted as (k_{31}^{xy}, k_{31}^z) . In general, these rates are assumed to be independent of the excitation intensity, but surprisingly that is not the case for this host/guest matrix. Hence, at this point, the model will start to deviate from the standard model and we will include a rISC term. Similar to the ISC rates, the triplet depopulation rates will be denoted as the effective depopulation rates. However, there must be a power-independent intrinsic

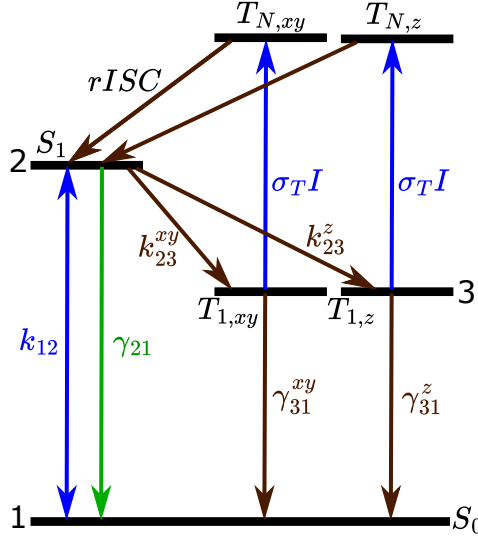


Figure 2.13.: Jablonski diagram of the energy level structure of perylene-d12. The intramolecular rates between the relevant energy levels are displayed next to the corresponding arrow of the transition. rISC is here depicted as a transition between T_1 and a higher excited triplet state T_N , of which the index is not known, followed by intersystem crossing back to the singlet excited state. The transition from T_1 to T_N is shown here with its associated absorption cross section σ_T , while the whole process of rISC will be captured by α (see equation 2.4).

depopulation rate, in case there is no contribution from rISC. The intrinsic depopulation rates will be called $(\gamma_{31}^{xy}, \gamma_{31}^z)$. To model the triplet depopulation rates on excitation intensity, a rISC term, α , is added as a secondary channel for the depopulation of the triplet state. We assume α to be the same for all three triplet sublevels. The effective depopulation rates will then become linearly-dependent on the light intensity:

$$(k_{31}^{xy}(I), k_{31}^z(I)) = (\gamma_{31}^{xy}, \gamma_{31}^z) + \alpha I. \quad (2.4)$$

Finally, using the standard model for the population rates, with the added rISC term in equation 2.4, we can describe the contrasts C_1 and C_2 and the decay parameters λ_1 and λ_2 of equation 2.2 in terms of the effective population and depopulation rates of the triplet states. Starting with the contrasts of the two exponentials, we have the following expression:

$$C_{1,2} = \frac{\lambda_{1,2}(k_{31}^{xy} - \lambda_{1,2})(k_{31}^z - \lambda_{1,2})}{k_{31}^{xy} k_{31}^z (\lambda_{1,2} - \lambda_{2,1})}, \quad (2.5)$$

where the decay parameters, λ_1 and λ_2 , are given by solutions of a characteristic equation:

$$\lambda_{1,2} = \frac{1}{2}(\Sigma \pm D), \quad (2.6)$$

with Σ the sum of all rates and D the discriminant of the characteristic equation, given by:

$$\Sigma = k_{23}^{xy} + k_{23}^z + k_{31}^{xy} + k_{31}^z, \quad (2.7)$$

$$D = \sqrt{\Sigma^2 - 4(k_{23}^{xy}k_{31}^z + k_{23}^zk_{31}^{xy} + k_{31}^{xy}k_{31}^z)}. \quad (2.8)$$

The cross-dependencies of equations 2.5, 2.6, 2.7 and 2.8 require that we have to fit all the parameters to the measurements at once. In addition, the dependence of equation 2.3 and 2.4 on respectively the saturation intensity and laser intensity adds more terms to fit. Hence, the equations for the fits in Figure 2.8b and 2.8c are included in the global fit to find the best matching parameters that satisfy the whole set of measurements. As we now have a model for rISC, the fit in Figure 2.8c can be discussed.

In general, the saturation of the fluorescence signal (F) from a single molecule follows a sigmoid-shaped curve, which has the following form:

$$F(I) = F_{\infty} \frac{\frac{I}{I_s}}{1 + \frac{I}{I_s}}. \quad (2.9)$$

This standard equation for saturation is used to describe the red data points and fit in Figure 2.8c, which traces the maximum fluorescence signal obtained from the single molecule, without blinking due to ISC. The saturation of a three-level system can also be described in terms of all intramolecular rates^{21,22}

$$F(I) = \eta \frac{\Phi_F \tau_F^{-1}}{2 + \frac{k_{23}^{xy}}{\gamma_{31}^{xy}} + \frac{k_{23}^z}{\gamma_{31}^z}} \frac{\frac{I}{I_s}}{1 + \frac{I}{I_s}}. \quad (2.10)$$

The parameter η is the detection efficiency of our setup, Φ_F is the fluorescence quantum yield and τ_F is the fluorescence lifetime. The fluorescence lifetime was already determined to be around 4.6 ± 0.1 ns using time-correlated single-photon counting under a pulsed excitation (Figure 2.9). A key difference between equation 2.9 and 2.10 is the inclusion of the ISC rates and triplet lifetimes, which are a limiting factor on the total fluorescence output. If the triplet depopulation rates would be constant with excitation intensity, the shape of the function, a sigmoid, would be preserved. However, the linear dependency of the depopulation rates on laser intensity captures the deviation of the saturation curve as observed for the blue points and fit curve in Figure 2.8c. As part of the global fit, we find a detection efficiency of our setup of around 9×10^{-4} , which is a typical value for our setup when assuming Φ_F to be close to unity (about 0.89²³). The relatively low detection efficiency is likely caused by a combination of a low NA objective, a lower quantum efficiency of our detector for the blue part of the spectrum and potential further losses in our cryogenic confocal setup, which is optimized for the near-infrared. Despite the low collection efficiency, the molecule is much brighter due to rISC, than it would have been in the absence of rISC. Based on the intrinsic

depopulation rates, the molecule would have saturated at a low 22 kcps, while with rISC we find a saturation intensity that is at least a four-fold higher, with about 100 kcps.

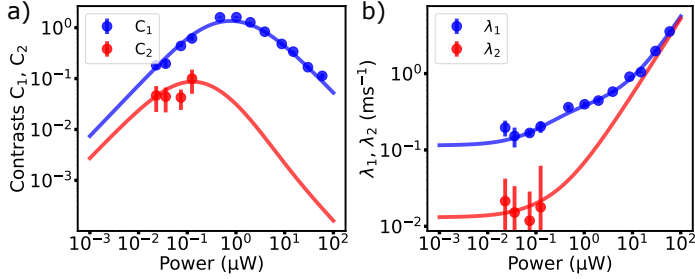


Figure 2.14.: Model fit for molecule M1. The points in panel (a) show the contrasts obtained from the individual fits to the autocorrelation curves, while the line is obtained from the global fit to equation 2.5. For panel (b) the points are given by the decay parameters obtained from the autocorrelation curves, while the line was obtained from the global fit to equation 2.6. Note that for the long-lived decay, the large difference between C_1 and C_2 from the fifth point and onwards made it difficult to distinguish two decays from the autocorrelation curve. Hence, from the fifth point and onwards we only fitted a single exponential decay.

Before we performed the global fit, all the recorded autocorrelation functions, such as in Figure 2.12, are fitted to equation 2.2 to obtain the contrasts C_1 and C_2 and decay parameters λ_1 and λ_2 . The resulting data is subsequently processed in a global fit, using equations 2.5-2.8. The data points for the contrasts and decay parameters and the result of the global fit are shown in Figure 2.14. The fit is logarithmically-weighted with the errors obtained from the individual fits of the autocorrelation curves. The optimal values that we find for the intrinsic population rates γ_{23}^{xy} and γ_{23}^z , the intrinsic depopulation rates γ_{31}^{xy} and γ_{31}^z and finally the rISC parameter α are shown in Table 2.1, for molecule M1 and two other molecules.

	$\gamma_{23}^{xy}(s^{-1})$	$\gamma_{31}^{xy}(s^{-1})$	$\gamma_{23}^z(s^{-1})$	$\gamma_{31}^z(s^{-1})$	$\alpha(\mu W^{-1} s^{-1})$	$I_s(Wcm^{-2})$	$F_\infty(kcps)$	$\Gamma_0(MHz)$	$\lambda(nm)$
M1	542 ± 25	114 ± 9	23 ± 6	13 ± 2	52.3 ± 0.8	22 ± 3	106 ± 1	58 ± 1	454.57
M2	550 ± 70	91 ± 7	76 ± 55	15 ± 11	14.2 ± 0.6	82 ± 20	51 ± 5	55 ± 2	454.38
M3	500 ± 27	146 ± 11	38 ± 13	19 ± 3	26.5 ± 0.9	59 ± 5	155 ± 2	59 ± 1	454.36

Table 2.1.: Reported results of the global fit for three individual molecules, for parameters as described in the text and Figure 2.13. The reported errors are standard deviations from the global fit.

From the intrinsic depopulation rate of the triplet state the triplet lifetime can be determined. For the average of the three molecules we find a triplet lifetime $(\gamma_{31}^{xy})^{-1}$ of the T_{xy} states of 8.5 ± 0.4 ms and for the T_z state a lifetime of 64 ± 12 ms. The average intersystem crossing rates are determined to be $532 \pm 26 s^{-1}$ for the

T_{xy} states and $46 \pm 19 \text{ s}^{-1}$ for the T_z state. The relatively large uncertainty of the parameters for the long-lived decay in Table 2.1 are likely related to the low photon counts of the measurements at low power, at which we were able to extract information about this state. At higher excitation intensities, the rISC parameter α dominated the statistics. Likely, the dominance of α leads to a convergence of the triplet depopulation rates of the T_{xy} and T_z substates, which causes the two exponential decays to start to overlap, becoming indistinguishable. Other variations between the results in Table 2.1 might be caused by heterogeneity of embedding sites, orientations and defects of the polycrystalline samples. When the rISC parameter α is corrected for the variations in saturation intensity, the average increase of the triplet depopulation rates is about 18 s^{-1} per saturation intensity.

The triplet lifetimes that we find are significantly longer than reported in the literature, i.e. 3.0 ms and 19 ms for non-deuterated perylene in *o*-DCB³ or $1.1 \pm 0.5 \text{ ms}$ in *n*-nonane.⁷ The increased lifetime is likely caused by the deuteration of the perylene molecule.²⁴ In general, the triplet lifetimes are reported to be longer for perdeuterated fluorophores compared to their non-deuterated analogues.²⁴ For perylene-d12 dissolved in PMMA, the triplet lifetime was found to increase by a factor of 2.3 (298 K) compared to perylene-h12.²⁴ Other parameters, such as triplet yield, are more comparable. From the ISC rate and the fluorescence lifetime we calculate a triplet yield by the equation $\Phi_T = \tau_F(k_{23}^{xy} + k_{23}^z)$ and we find a value in the order of 3×10^{-6} , which is equal to the triplet yield found for perylene-h12 in *o*-DCB.³

The reason for efficient rISC taking place in this particular matrix, as opposed to other matrices that have been used for perylene or many other guest molecules, remains unknown. Only for terrylene in *p*-terphenyl, rISC was observed at temperatures above 50 K, but was absent or negligible at lower temperatures.^{25,26} The most commonly proposed pathway for rISC involves an intramolecular intersystem crossing, i.e., a spin-flip process when the perylene molecule is in a high triplet level.^{27,28} In higher excited states, the density of vibrational states in both multiplicities makes it easy to achieve resonance between triplet and singlet levels, leading to relaxation to the lower singlet states. The large $T_1 - T_N$ energy gap and the energetic proximity of T_N and S_N could favor rISC over an internal conversion process from T_N to T_1 .²⁸ In addition, this internal conversion could be a bit more suppressed due to the deuteration of the molecule. There might be also a role of the matrix, such as that the relatively heavy sulfur atom of the matrix molecule could further help couple singlet and triplet states, particularly in the more delocalized orbitals of the higher excited states.²⁹ If this triplet-to-singlet transition is fast enough, the rISC rate would be dominated by the optical excitation of the T_{xy} and T_z states, leading to the same rISC rate for all the three triplet sublevels. Finally, the efficiency of rISC does not appear to vary significantly from molecule to molecule. However, the rISC process could be of use while doing spectroscopic studies on the excited triplet states by not using the optical fluorescence-exciting beam to induce rISC, but by using a secondary tunable beam²⁷ or a time-gated double excitation method to determine the quantum yields of the T_N to S_1 rISC²⁹ (see scheme in Figure 2.15). The rISC process might also be harnessed for a better control of triplet blinking in view of fluorescence super-resolution STORM schemes at low temperature.³⁰⁻³²

2.4. CONCLUSION AND OUTLOOK

In this chapter, we have demonstrated that dibenzothiophene is an appropriate matrix for perylene. The spectral lines of perylene are relatively stable and the 0-0 zero-phonon lines have a near lifetime-limited linewidth. Moreover, at higher excitation intensities, the fluorescence signal from single perylene molecules is on par with other bright systems commonly employed as lifetime-limited single-molecule emitters. That is a direct consequence of reverse intersystem crossing (rISC) that allows the recovery of the molecule from the long-lived triplet state and at least quadruples the detectable fluorescence rate. By studying the autocorrelations of fluorescence time traces we were able to estimate the intrinsic triplet lifetimes of deuterated perylene to be 8.5 ± 0.4 ms for the T_{xy} -states and 64 ± 12 ms for the T_z -state. In addition, we were able to quantify the effect of rISC on the depopulation rate of the triplet states.

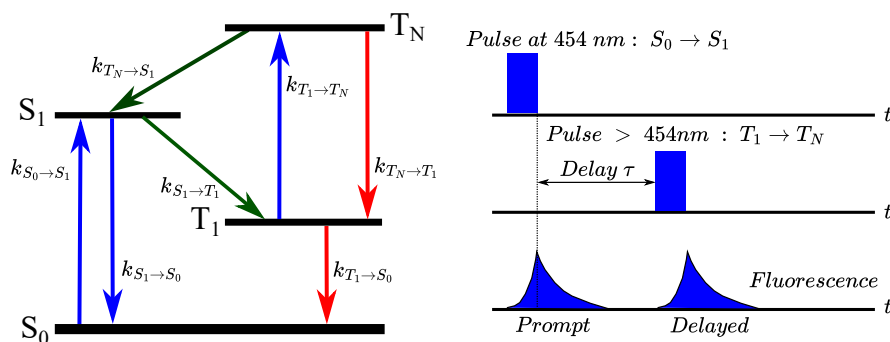


Figure 2.15.: Proposed pump-probe experiment on single perylene molecules or ensembles to determine rISC efficiency as a function of wavelength. The experiment starts with an initial laser pulse tuned to the resonance of the $S_0 \rightarrow S_1$ transition. Through intersystem crossing (part of) the molecule(s) end up in the triplet state T_1 . A second short pulse, off-resonant with the $S_0 \rightarrow S_1$ transition and delayed enough for prompt fluorescence to have decayed significantly, is used to probe resonances in the $T_1 \rightarrow T_N$ transition. Successful transfer of the population from $T_1 \rightarrow S_1$, through T_N , would give rise to delayed fluorescence, with near-unity quantum yield. This would in principle allow the measurement of a $T_1 \rightarrow T_N$ absorption spectrum as a function of the delayed fluorescence signal obtained through the rISC process. Separation of prompt and delayed fluorescence can be handled using an optical chopper as described in Chapter 3. When the rate of absorption in the triplet, $k_{T_1 \rightarrow T_N}$, and the rISC rate, $k_{T_1 \rightarrow S_1}$, are known, the non-radiative rate $k_{T_N \rightarrow T_1}$ could be determined from experiment.

The demonstrated effect of rISC, never observed at such low temperatures and with narrow resonances, could be used in the future to study the higher triplet states of perylene, by using a second tunable laser beam that probes the rISC efficiency as a

function of $T_1 \rightarrow T_N$ absorption, while similar to studies of anthracenes,²⁹ a time-gated double-excitation method as described in Figure 2.15, could be used to determine the quantum yields of rISC. Finally, it would be interesting to find out if rISC would be also present in hydrogenated perylene, in order to see if the change in vibrational energies between perdeuterated and hydrogenated perylene is a reason why rISC has never been observed before for perylene in other systems.

In the next chapter, we will proceed with our new host-guest system to find out whether we can detect phosphorescence from the triplet states.

REFERENCES

- (1) Erker, C.; Basché, T. *Journal of the American Chemical Society* **2022**, *144*, 14053–14056.
- (2) Nicolet, A. A. L.; Hofmann, C.; Kol'chenko, M. A.; Kozankiewicz, B.; Orrit, M. *ChemPhysChem* **2007**, *8*, 1215–1220.
- (3) Verhart, N. R.; Navarro, P.; Faez, S.; Orrit, M. *Physical Chemistry Chemical Physics* **2016**, *18*, 17655–17659.
- (4) Englman, R.; Jortner, J. *Molecular Physics* **1970**, *18*, 145–164.
- (5) Siebrand, W.; Williams, D. F. *The Journal of Chemical Physics* **1967**, *46*, 403–404.
- (6) Walla, P. J.; Jelezko, F.; Tamarat, P.; Lounis, B.; Orrit, M. *Chemical Physics* **1998**, *233*, 117–125.
- (7) Pirootta, M.; Renn, A.; Werts, M. H. V.; Wild, U. P. *Chemical Physics Letters* **1996**, *250*, 576–582.
- (8) Kellogg, R. E.; Bennett, R. G. *The Journal of Chemical Physics* **1964**, *41*, 3042–3045.
- (9) Siebrand, W. *The Journal of Chemical Physics* **1967**, *47*, 2411–2422.
- (10) Nicolet, A.; Kol'chenko, M. A.; Kozankiewicz, B.; Orrit, M. *The Journal of Chemical Physics* **2006**, *124*, 164711.
- (11) Goldacker, W.; Schweitzer, D.; Zimmermann, H. *Chemical Physics* **1979**, *36*, 15–26.
- (12) Bree, A.; Zwarich, R. *Spectrochimica Acta Part A: Molecular Spectroscopy* **1971**, *27*, 621–630.
- (13) McArdle, B. J.; Sherwood, J. N. **1974**, *22*, 193–200.
- (14) Abram, I. I.; Auerbach, R. A.; Birge, R. R.; Kohler, B. E.; Stevenson, J. M. *The Journal of Chemical Physics* **1975**, *63*, 2473–2478.
- (15) Unwin, P. J.; Jones, T. S. *Surface Science* **2003**, *532*, 1011–1016.
- (16) Suganuma, Y.; Kowaka, Y.; Ashizawa, N.; Nakayama, N.; Goto, H.; Ishimoto, T.; Nagashima, U.; Ueda, T.; Yamanaka, T.; Nishi, N.; Baba, M. *Molecular Physics* **2011**, *109*, 1831–1840.
- (17) Sulkes, M. *Chemical Physics* **1987**, *114*, 289–294.
- (18) Basché, T.; Kummer, S.; Bräuchle, C. *Nature* **1995**, *373*, 132–134.
- (19) Bernard, J.; Fleury, L.; Talon, H.; Orrit, M. *The Journal of Chemical Physics* **1993**, *98*, 850–859.

- (20) Lawetz, V.; Orlandi, G.; Siebrand, W. *The Journal of Chemical Physics* **1972**, *56*, 4058–4072.
- (21) De Vries, H.; Wiersma, D. A. *The Journal of Chemical Physics* **1980**, *72*, 1851–1863.
- (22) Ambrose, W. P.; Basché, T.; Moerner, W. E. *The Journal of Chemical Physics* **1991**, *95*, 7150–7163.
- (23) Birks, J. B.; Dyson, D. J.; Flowers, B. H. *Proceedings of the Royal Society of London. Series A. Mathematical and Physical Sciences* **1963**, *275*, 135–148.
- (24) Kellogg, R. E.; Wyeth, N. C. *The Journal of Chemical Physics* **1966**, *45*, 3156–3158.
- (25) Fleury, L.; Segura, J.-M.; Zumofen, G.; Hecht, B.; Wild, U. P. *Physical Review Letters* **2000**, *84*, 1148–1151.
- (26) Banasiewicz, M.; Morawski, O.; Wiącek, D.; Kozankiewicz, B. *Chemical Physics Letters* **2005**, *414*, 374–377.
- (27) Ringemann, C.; Schönle, A.; Giske, A.; Middendorff, C. v.; Hell, S. W.; Eggeling, C. *ChemPhysChem* **2008**, *9*, 612–624.
- (28) Hu, D.; Yao, L.; Yang, B.; Ma, Y. *Philosophical Transactions. Series A, Mathematical, Physical, and Engineering Sciences* **2015**, *373*, 20140318.
- (29) Kobayashi, S.; Kikuchi, K.; Kokubun, H. *Chemical Physics* **1978**, *27*, 399–407.
- (30) Hoffman, D. P.; Shtengel, G.; Xu, C. S.; Campbell, K. R.; Freeman, M.; Wang, L.; Milkie, D. E.; Pasolli, H. A.; Iyer, N.; Bogovic, J. A.; Stabley, D. R.; Shirinifard, A.; Pang, S.; Peale, D.; Schaefer, K.; Pomp, W.; Chang, C.-L.; Lippincott-Schwartz, J.; Kirchhausen, T.; Solecki, D. J.; Betzig, E.; Hess, H. F. *Science* **2020**, *367*, DOI: 10.1126/science.aaz5357.
- (31) Dahlberg, P. D.; Moerner, W. E. *Annual Review of Physical Chemistry* **2021**, *72*, 253–278.
- (32) Hulleman, C. N.; Li, W.; Gregor, I.; Rieger, B.; Enderlein, J. *ChemPhysChem* **2018**, *19*, 1774–1780.

3

THE PHOSPHORESCENCE OF PERYLENE

In this chapter, I will show how we used the dibenzothiophene host matrix to enhance the phosphorescence signal from embedded perylene-d12 molecules. We excited the host molecules with UV light from a mercury light source and we observed a strong phosphorescence signal due to strong intersystem crossing of the host at liquid helium temperatures. At a slightly raised temperature, the triplet excitons are found to transfer efficiently to impurities in the host matrix. With a high doping level of perylene-d12 in very pure dibenzothiophene, most of the triplet excitons found their way to perylene-d12, which resulted in a detectable phosphorescence signal. The triplet state of perylene-d12 is found to be around 784.2 nm (air) or 12,756 cm⁻¹ (vacuum) for the main spectroscopic site.

3.1. INTRODUCTION

3.1.1. SCHEME FOR PHOSPHORESCENCE DETECTION

In the previous chapter I introduced the new host/guest system of perylene-d12 in a dibenzothiophene crystal. In this chapter, I will continue with this matrix and report on the triplet state energy. As discussed in the previous chapter, interesting triplet dynamics are observed for this system in the form of reverse intersystem crossing (rISC), acting as a separate pathway for the depopulation of the triplet state. However, these particular dynamics could make it difficult to detect phosphorescence from intersystem crossing from the singlet excited state S_1 to the triplet state T_1 , as many triplets could be lost by rISC. Fortunately, the excitation scheme that we have in mind, shown in Figure 3.1, avoids this depletion channel by exciting the host molecules, rather than the guest molecule itself.

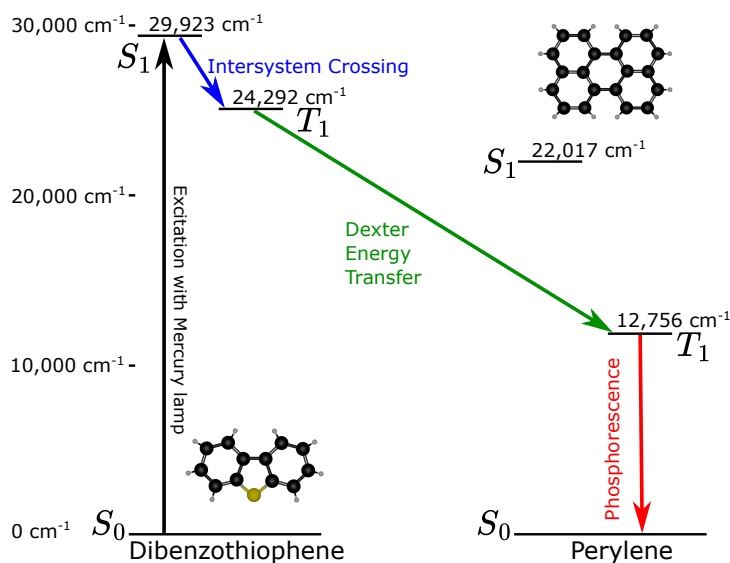


Figure 3.1.: Energy level scheme of perylene-d12 in dibenzothiophene. The energy levels of dibenzothiophene are known from the literature¹ The $S_0 - S_1$ energy gap of perylene-d12 was derived from the emission spectrum in Figure 2.4 of Chapter 2 and the $S_0 - T_1$ energy gap is derived from the phosphorescence spectrum in the present chapter. The excitation scheme relies on a UV excitation ($< 334 \text{ nm}$) of the singlet excited state of dibenzothiophene, followed by an intersystem crossing to the triplet state of dibenzothiophene. The excitonic energy may then be transferred to perylene through Dexter energy transfer, where upon the excited triplet of perylene may release a phosphorescence photon.

The excited singlets in the host may decay back to the ground state or form triplets by intersystem crossing (ISC). The ISC rate in dibenzothiophene was found to be

enhanced, likely due to a heavy-atom effect of the central sulfur atom and possibly helped by the relatively small $S_1 - T_1$ energy gap (about $5,632 \text{ cm}^{-1}$). For this reason, dibenzothiophene and related compounds have for instance been used in complexes to achieve efficient room-temperature phosphorescence.² After the formation of triplets, the triplets may be transferred by a Dexter energy exchange³ to the perylene molecule. The Dexter energy transfer decays exponentially with the distance between the perylene and dibenzothiophene molecule, due to its dependence on wavefunction overlap. Due to the very large gap between T_1 of dibenzothiophene and T_1 of perylene, found to be around $11,536 \text{ cm}^{-1}$, it is hard to predict whether this process will actually happen efficiently.

3.2. EXPERIMENTAL

3.2.1. PHOSPHOROSCOPE SETUP

As phosphorescence is a significantly weaker signal than fluorescence, the two signals have to be separated to avoid that fluorescence would saturate the spectrum. Fluorescence is typically very short lived, for perylene in the order of nanoseconds. The phosphorescence is much longer lived, and for example for perylene the triplet has about a 6 orders of magnitude longer lifetime than the singlet. Hence, imposing a short delay between the excitation signal and the detection signal can allow us to filter out the weak phosphorescence signal out of a very strong fluorescence background. The setup (usually called a phosphoroscope, see Figure 3.4) we built to this goal makes use of an optical chopper, which is a rotating wheel with open and closed parts. In our setup we made use of a very simple chopper wheel, that was modified to have a "pac-man" shape, having an opening of 25% of the surface area, while the rest blocks light. This design is shown in Figure 3.2.

The chopper module consists of a 418F optical chopper and control module from Bentham. This module optically measures the chopper frequency and has an internal circuit to balance the rotation frequency. In the configuration shown in Figure 3.2, the excitation and detection beam are positioned at each side of the chopper. With both beams at the same height, the excitation and detection windows are delayed by a fourth of a rotation cycle. Also, the duration of the excitation and detection windows are a fourth of a rotation cycle.

For the excitation we made use of a 100 W (electrical power) mercury lamp (Newport, 6281) that is fixed in a lamp housing (Oriel, 68810) and powered by a supply unit (Newport, 69911). The old lamp was replaced by a new one to make sure the UV part of the spectrum was not degraded. The lamp housing collects and collimates the light from the arc lamp using a concave mirror and collimation lenses at the output. The light intensity was measured in the 440-460 nm region using a power meter and indicated an integrated intensity of 2.5 mW. Unfortunately, the power meter could not measure UV, but the light could easily be seen as blue fluorescence from white paper. To separate the UV light from the rest of the spectrum, we used a FSR-U340 filter that has the best transmission below 340 nm. However, the filter transmission already starts to decay below 300 nm. The spectrum of the mercury lamp, as transmitted by the filter, is shown

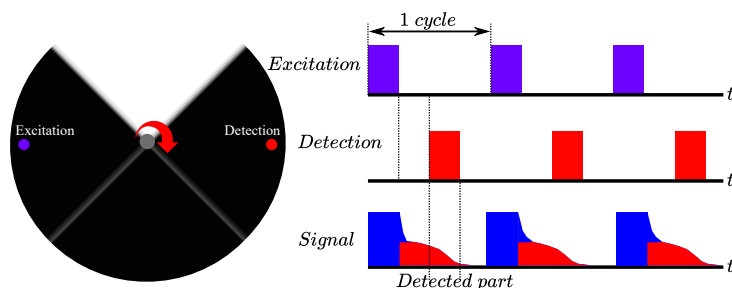


Figure 3.2.: Schematic of the optical chopper scheme. The excitation and detection beam are located at opposite sides of the chopper, which has an open part over a quarter of its area. The rotating chopper makes sure there is a delay of about $\frac{1}{4}$ of a full rotation between the excitation and detection windows to remove unwanted short-lived photoluminescence, in particular fluorescence. The excitation and detection cycles are shown in a square wave profile on the right. The signal, shown schematically in blue for fluorescence and red for phosphorescence is strongly exaggerated in terms of timescales, as the fluorescence decays six orders of magnitude faster than the phosphorescence of perylene.

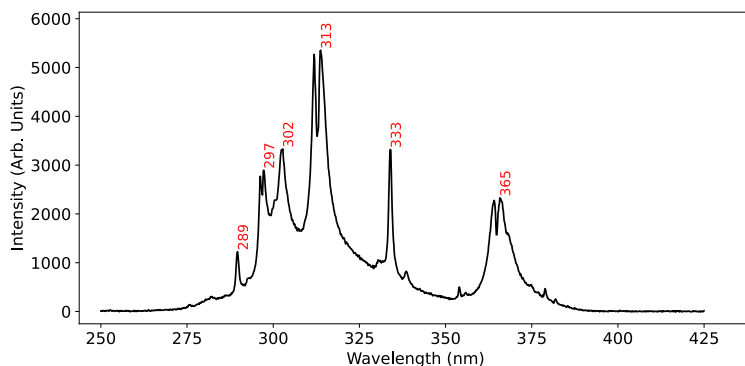


Figure 3.3.: Spectral lines of the mercury lamp that were transmitted by the filter that was used at the excitation side (FSR-U340). All the spectral lines below approximately 334 nm are used for the $S_0 \rightarrow S_1$ transition of dibenzothiophene. The spectral lines above 334 nm could still excite the much weaker $S_0 \rightarrow T_1$ transition of dibenzothiophene.

in Figure 3.3. For an excitation of the host's singlet we need light of a wavelength that is shorter than 334 nm. Thus, the set of spectral lines around 289 nm, 297 nm, 313 nm and 333 nm are likely the most efficient for the excitation of the singlet.

To minimize losses of UV light in the excitation path we made use of aluminum

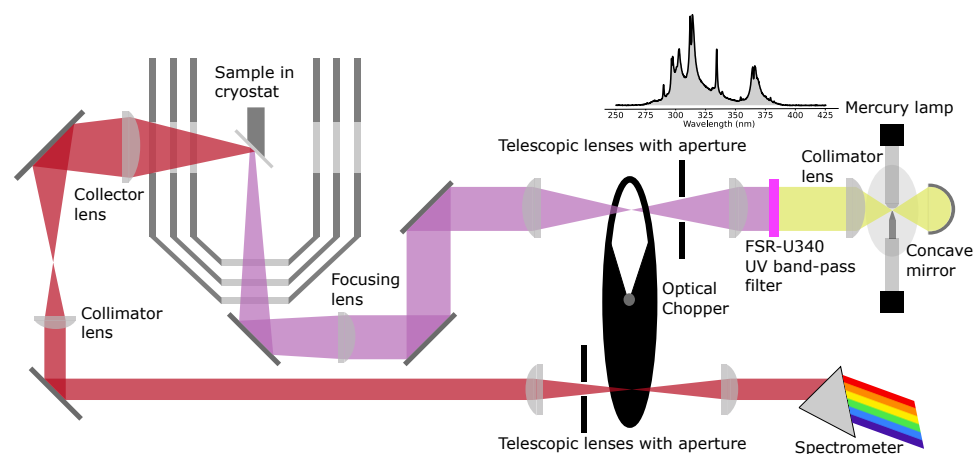


Figure 3.4.: Schematic of the phosphorescope. Starting from the top right: The collimated light from the mercury arc lamp is filtered to pass the part of the mercury spectrum as shown in Figure 3.3. The UV light is then focused on the chopper, while the beam is cleaned with an aperture. After a focusing lens, the light enters the cryostat from below, passes through the three fused silica windows, and hits the sample with a few mm beam shape. The phosphorescence is collected from the side of the cryostat by a large lens, where further on the emitted light is collimated and again focused onto the chopper and cleaned up by an aperture. Finally, the phosphorescence hits the detector of the spectrometer. Not shown here is the extensive shielding placed between the two light paths. It is important that no light leaks from the excitation path to the detection path, as it can blur weak phosphorescence signals on the spectrometer.

mirrors, which instead of silver has a higher reflectivity in the UV region. Similarly, we used fused-silica lenses to improve UV transmission. A set of two lenses of that type are used in the excitation path. The first lens is used to focus the light on the chopper wheel. The second lens refocuses the diverging beam towards the sample, where the UV light enters the cryostat via fused silica windows. In the detection path we made use of silver mirrors and lenses optimized for the NIR, which is the region where we expect the phosphorescence to be. The light is then focused on the slit of the spectrometer. A slit size of 0.1 mm and a 600 lines/mm grating were the standard settings used for the detection of phosphorescence.

3.3. RESULTS AND DISCUSSION

3.3.1. PHOSPHORESCENCE OF DIBENZOTHIOPHENE

At temperatures of liquid helium and lower, achieved by filling the sample chamber with helium and reducing the pressure, the phosphorescence signal of dibenzothiophene is clearly resolved. A high resolution spectrum of the delayed emission is shown in Figure 3.5. The spectrum is characterized by sharp lines (around 8 ± 2 cm^{-1} in width) and a clearly resolved vibronic structure, only weakly inhomogeneously broadened. The vibrational fingerprint of this spectrum has been assigned before.¹ The origin of the sharp lines is likely related to emission from isolated defect sites, sometimes called X-traps.^{1,4,5} It was reported though that the phosphorescence of high-quality crystals could be observed at temperatures up till 77 K, which was not the case for our crystals. This might be related to the doping of the crystals with perylene-d12, the poorer crystallization due to fast quenching and/or other impurities in the crystal. The poorer quality of our crystals is also reflected by the larger inhomogeneous broadening of the lines in Figure 3.5, which was reported to be around 1.5 cm^{-1} for high-quality crystals.⁴ The chemical origin of dibenzothiophene might be also different for the commercial dibenzothiophene that we used. In the literature, the dibenzothiophene was synthesized by a reaction of elemental sulfur with highly-purified biphenyl.⁴ This route may avoid the formation of some impurities that we have detected in our samples.

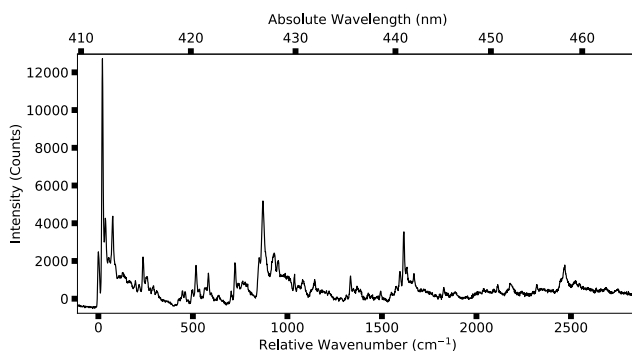


Figure 3.5.: Delayed emission spectrum of dibenzothiophene crystals doped with perylene-d12. The spectrum is recorded at 2 K, where the excited triplet remains trapped on the host molecule. The integration time of the spectrum is 6 minutes, taken with a 0.1 mm slit size and 1200 lines/mm grating. The spectrum is recorded in the second order of the grating to obtain a higher resolution. The first peak in the spectrum was chosen as the origin of the spectrum, with the relative energy of the vibrational peaks indicated in wavenumbers (cm^{-1}).

In addition to the high-resolution settings for the spectrum in Figure 3.5, we also recorded the dibenzothiophene phosphorescence spectrum with the same settings at which we would record the phosphorescence spectrum of perylene. The integrated intensity resulted in a signal on the order of 7.7 million counts per second. This

intensity was more than enough to record the phosphorescence decay over time with a single-photon counter. To record the decay of the phosphorescence signal, the chopper was removed and a mechanical shutter was placed in the excitation path. The measured decay of the phosphorescence signal in Figure 3.6 reveals that the triplet state is very long lived. The phosphorescence decay curve is best fitted with a sum of three exponentials, though two of them have quite close decay times. The short components in the decay curve have lifetimes of 0.24 ± 0.03 s and 0.68 ± 0.01 s, while the long decay has a lifetime of 4.7 ± 0.3 s. The two short lifetimes could be related to the T_x and T_y sublevels of the triplet, while the long lifetime likely belongs to the T_z sublevel. In the literature, the phosphorescence lifetimes of dibenzothiophene were measured to be 0.29 ± 0.02 s for T_x , 0.36 ± 0.02 s for T_y and 9.1 ± 0.8 s for T_z .⁴ These individual rates, with two of them very close in time, could be established by microwave-induced delayed phosphorescence (MIDP) experiments, which rely on the saturation of triplet sublevels by inducing a microwave transition to that particular sublevel.⁶ However, the close proximity of the T_x and T_y sublevels makes it unlikely that we can distinguish them from the phosphorescence decay and it might be possible that some impurity affects the decay curve, which is measured in the region of 440-460 nm, due to a lack of available filters in the violet region of the visible spectrum.

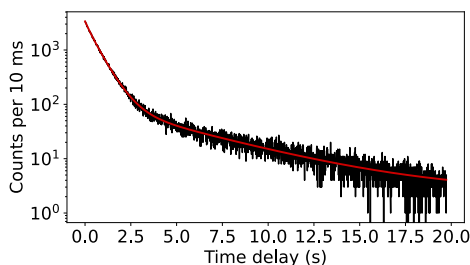


Figure 3.6.: Phosphorescence decay curve of dibenzothiophene crystals at 2 K. The integration time is 10 ms per point, measured in the spectral region determined by a band pass filter between 440-460 nm. The red curve is a fit by a sum of three exponential decays.

3.3.2. PHOSPHORESCENCE OF PERYLENE

Above the temperature of liquid helium, in the region of 4-8 K, the phosphorescence of dibenzothiophene starts to decrease. At this point, the excited triplets will behave as excitons and are able to migrate to deeper traps, which could be perylene molecules or other impurities. In fact, impurities are found to be a limiting factor in some of the experiments. Hence, the concentration of perylene with respect to the concentration of these impurities has to be optimal. Therefore we used a relatively high concentration of perylene-d12 dopant molecules, of around $100 \mu\text{mol/mol}$. The location of the dibenzothiophene material in the zone-refining tube was important as well, which is related to the gradients in impurity concentrations along the length of the tube. In

several experiments, the material came from a different position and led to very different results, as each time a different impurity was dominating. Only in the cleanest material were we able to detect the phosphorescence of perylene.

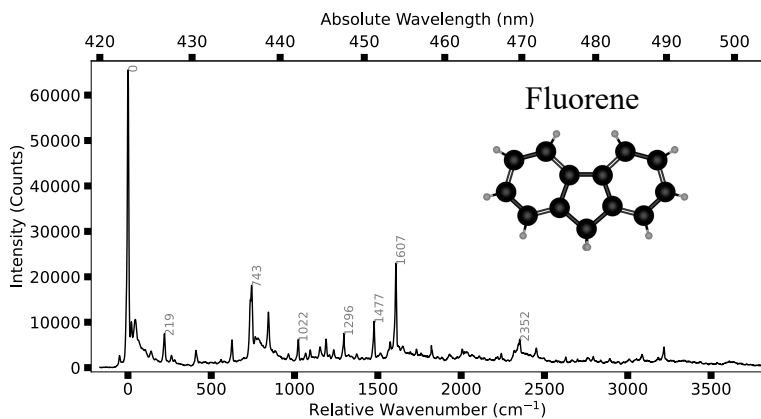


Figure 3.7.: Phosphorescence spectrum of an impurity of dibenzothiophene. Note that the structure of the spectrum is very similar to that of dibenzothiophene. Hence, this is likely a molecule with a related chemical structure. In fact, the vibrational fingerprint matches that of fluorene.⁷ The structure of fluorene is shown on the top right. Compared to dibenzothiophene, the central sulfur atom has been replaced with a carbon atom, terminated with two out of plane hydrogen atoms.

A phosphorescence spectrum of an impurity that we could identify is that of fluorene, shown in Figure 3.7. This impurity is not detected in any of the other samples. The dibenzothiophene material that was used in this experiment was extracted closer to the dirty end of the zone-refining tube. Similarly, in other experiments we found two unknown impurities that are phosphorescing. The spectra of these impurities are shown in Figure 3.8. The unidentified compound in Figure 3.8b shows phosphorescence in the most red-shifted region observed so far. The 0-0 zero-phonon line at 672.5 nm indicates that energy was transferred from dibenzothiophene's triplet to the triplet of this compound, bridging a gap of more than 9,400 cm⁻¹. Hence, it may seem possible that the even larger energy gap between the triplet state of dibenzothiophene and the triplet state of perylene-d12 could be crossed as well.

With material from the purest part of the zone-refining tube, we again prepared a high-concentration sample and repeated the measurement. In the phosphorescence spectrum of this sample only an impurity phosphorescing around 475 nm was found (Figure 3.8a), different from the impurities obtained in previous experiments. Although a part of the triplet excitons are lost to this impurity, a relatively good signal could be detected in the expected region of the perylene triplet. The measured spectrum, obtained over the course of 45 minutes, is shown in Figure 3.9. This spectrum was superimposed

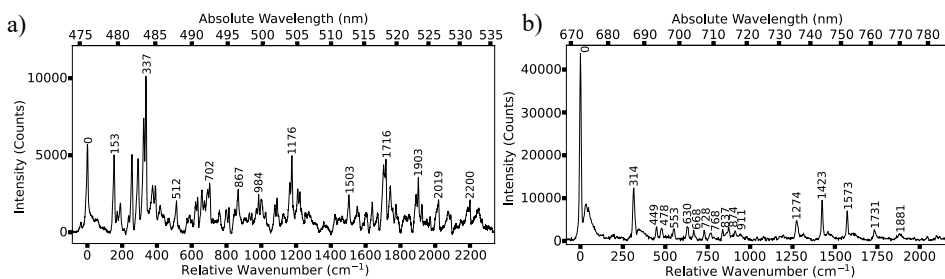


Figure 3.8.: Phosphorescence spectra of unidentified impurities in dibenzothiophene. Panel (a) shows a phosphorescence spectrum of an impurity found in the experiment where we detected perylene-d12 phosphorescence as well. The spectrum is very crowded with lines and might be mixed with another impurity. Panel (b): Apart from perylene-d12, this was the most red-shifted impurity found. The spectrum is different in shape and crowdedness compared to the spectrum of dibenzothiophene in Figure 3.5, the spectrum of fluorene in Figure 3.7 or the spectrum in (a), but resembles more closely a spectrum of a general aromatic compound, without heteroatoms. Unfortunately, the tail of this spectrum stretched all the way into the region of the phosphorescence of perylene-d12, which made this sample useless for the detection of the perylene-d12 triplet energy.

on a strong tail of non-structured delayed luminescence (either phosphorescence or delayed fluorescence from triplet-triplet annihilation). The tail was subtracted by fitting a baseline to it. The origin of the spectrum appears at 784.2 nm or $12,756\text{ cm}^{-1}$, which is calibrated using a Krypton spectral lamp. The full-width-at-half-maximum of the 0-0 ZPL is around $34 \pm 4\text{ cm}^{-1}$, which is larger than the linewidth detected in the ensemble fluorescence spectrum in Figure 2.4 of Chapter 2. However, the much higher concentration is likely the cause of the broadening. Though the spectral lines correspond with the vibrational fingerprint of perylene-d12, the line shifted by 69 cm^{-1} , which can be observed for all other vibrational peaks as well, is not observed in the fluorescence spectrum. It might be a phonon mode or a different spectral site that was not observed with selective excitation when recording the ensemble fluorescence spectrum. Unlike the selective excitation used for molecules in the fluorescence spectrum, the migration of triplets from the host to perylene-d12 would probably not depend strongly on the energetic position of the perylene-d12 molecules. In section 3.3.3, the possibility of the existence of other sites is studied further and compared to fluorescence spectra.

The location of the triplet state at $12,756\text{ cm}^{-1}$ compares well to the position of the triplet found in anthracene as a host,⁸ which was found at $12,844\text{ cm}^{-1}$. The slight blue-shifted triplet state in anthracene was also observed for the singlet state, which was located at $22,263\text{ cm}^{-1}$, compared to $22,017\text{ cm}^{-1}$ in dibenzothiophene. The most red-shifted triplet energy was found in the pure crystal of perylene,⁹ at $12,372\text{ cm}^{-1}$.

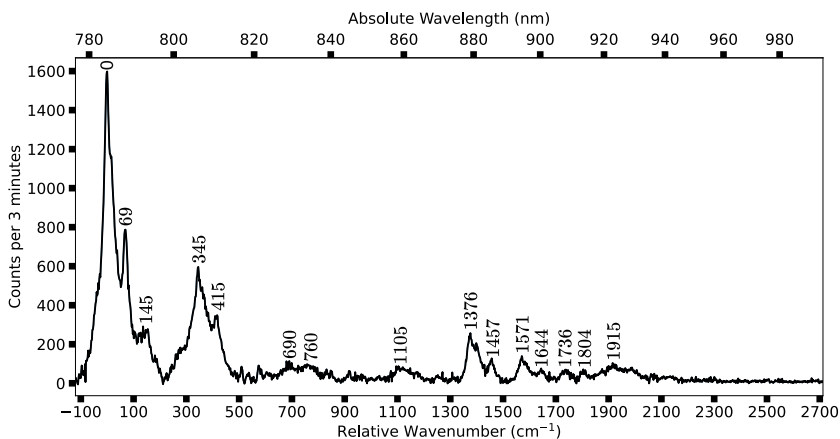


Figure 3.9.: Phosphorescence spectrum of perylene-d12 at a chopper rate of 18 Hz, imposing a delay of 15.6 ms between excitation and detection cycles. The integration time is 45 minutes in total, recorded in two sections, where single spectra are taken at a 3 minute integration time and subsequently merged. The individual spectra are used to remove cosmic rays by substitution. The vibrational fingerprint closely resembles that of the fluorescence spectrum in Figure 3 in Chapter 2, but the lines are much broader due to the high concentration of perylene-d12 and possible mixture of multiple spectroscopic sites (see section 3.3.3).

The integrated intensity of the spectrum gives an average phosphorescence signal of 1000 counts per second. Given that this spectrum is recorded with the same settings as used for estimating the phosphorescence signal of dibenzothiophene we can make a crude estimate of the probability of energy transfer from dibenzothiophene to perylene-d12. However, we need to estimate the quantum yield of phosphorescence as well. Assuming a radiative lifetime $(\gamma_{31}^{rad.})^{-1}$ in the order of 30 s, which was found to be a good approximation for many polyaromatic hydrocarbons,^{10,11} we can estimate a quantum yield ϕ_{ph} through the following way:

$$\phi_{ph} = \frac{\gamma_{31}^{rad.}}{\gamma_{31}}. \quad (3.1)$$

Here the rate γ_{31} is the depopulation rate of the triplet state. From the phosphorescence decay of dibenzothiophene in Figure 3.65 we can estimate that for the T_x and T_y state, the triplet depopulation rates will likely be in the order of 2-4 s^{-1} and for the T_z state in the order of 0.2 s^{-1} . This results in an estimated phosphorescence quantum yield of 0.8-1.6 % for the T_x and T_y state and about 16 % for the T_z state. These estimates do not differ much from the reported phosphorescence quantum yield at room temperature for dibenzothiophene, which was found to be in the order of 2-3 %.¹² Similarly, for perylene we estimate a phosphorescence quantum yield of 0.03 % for the T_{xy} sublevels

and 0.2 % for the T_z sublevel. Given that we have phosphorescence quantum yields for perylene and dibenzothiophene, we can estimate the probability for energy transfer by:

$$k_{dbt \rightarrow pr} = \frac{\phi_{dbt}}{\phi_{pr}} \frac{N_{pr}}{N_{dbt}} \approx 1\%, \quad (3.2)$$

where N_{dbt} and N_{pr} are the detected phosphorescence signals for respectively dibenzothiophene and perylene. The calculated rate is relatively high, considering that most triplets end up in impurities that are contributing to the strong background in the phosphorescence spectrum and to a structured spectrum at shorter wavelengths, shown in Figure 3.8a. A possible explanation is that not merely the T_1 of perylene is involved in the transfer, but possibly also the T_2 state. A theoretical study of the electronic levels of perylene found that the T_2 state is about 0.2 eV above the singlet excited state S_1 .¹³ For perylene in dibenzothiophene this would mean that the T_2 state could be located around $23,600 \text{ cm}^{-1}$, which is just below the T_1 state of dibenzothiophene and therefore could provide an additional channel for Dexter energy transfer between dibenzothiophene and perylene (see diagram in Figure 3.10).

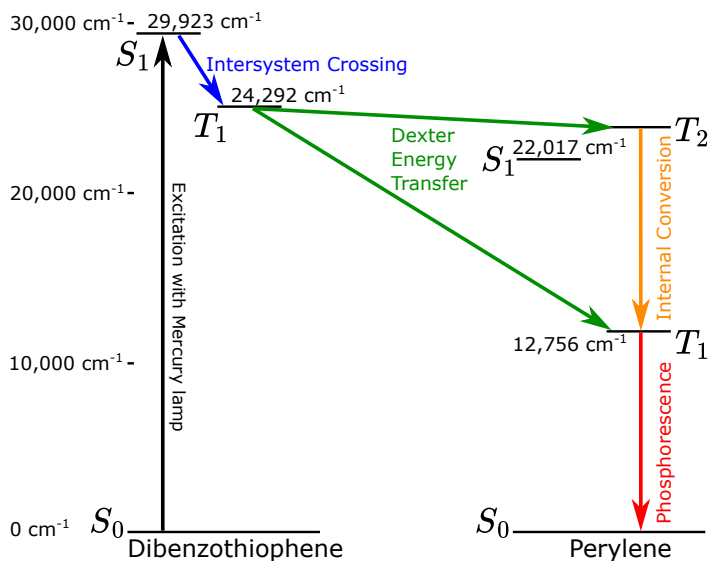


Figure 3.10.: The literature reports¹³ that there might be a second triplet excited state T_2 of perylene, which is only 0.2 eV higher in energy than the singlet excited state S_1 of perylene. The energy of T_2 would therefore be slightly lower than T_1 of dibenzothiophene and therefore T_2 of perylene may participate in the energy transfer between dibenzothiophene and perylene.

We also attempted to measure a phosphorescence decay of the spectral region around 780 nm, but the strong background made it difficult to separate the part that can be attributed to perylene-d12. Therefore, we tried to estimate the phosphorescence decay by varying the chopper rate and measuring the integrated intensity of the

phosphorescence spectrum. Based on the chopper frequency we measure the area under the phosphorescence decay curve, which can be derived by integration:¹⁴

$$N_{pr} = \int_{\frac{1}{4}C}^{\frac{1}{2}C} \sum_{i=1}^n A_i e^{-\frac{t}{\tau_i}} dt = f \sum_{i=1}^n \frac{A_i \tau_i (e^{\frac{1/4}{f\tau_i}} - 1)}{e^{\frac{1/2}{f\tau_i}}}, \quad (3.3)$$

where f is the chopper frequency, C the period and the sum constitutes the individual exponential decays with characteristic times τ_i and amplitude A_i .

3

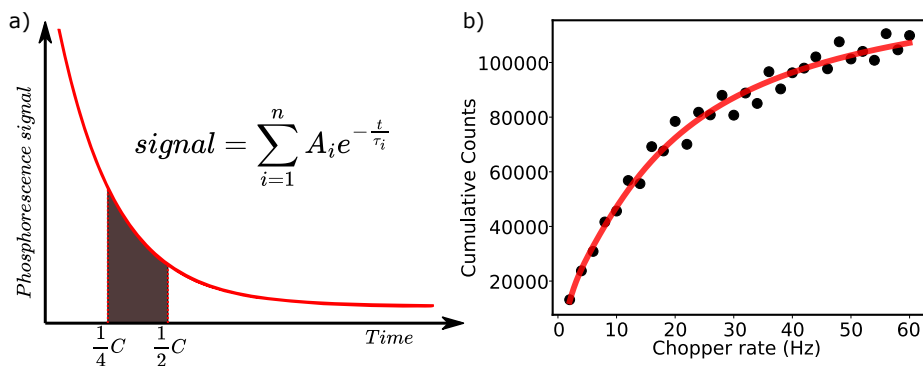


Figure 3.11.: Panel (a) shows a schematic representation of the measured integrated intensity of the exponential decay of phosphorescence in terms of the time per cycle. At an increased chopper rate the integrated area moves to the left. In steady state, the decay curve is represented by the shown formula. Panel (b) shows the integrated intensity of perylene-d12 phosphorescence measured in a single spectrum at various chopper rates. The integration time per point is 120 seconds and the line is a fit of the data to equation 3.3. The best fit is obtained by a sum of two exponential decays.

The two-component fit results in phosphorescence lifetimes of 18 ± 4 ms and 144 ± 58 ms. This is significantly longer than what we find in single-molecule experiments (see Chapter 2): 8.5 ± 0.4 ms and 64 ± 12 ms. However, the uncertainty of the fit in Figure 3.11b is much more significant. In addition, each data point is extracted out of a recorded spectrum, which is superimposed on a strong phosphorescence background with its own time characteristics. By varying some parameters in the isolation of the perylene phosphorescence spectrum from the large background, it was observed that the fit is strongly affected by the value of the points at low chopper rates. These data points are also more uncertain due to the weak signal in the spectra. However, it might be possible that there is some characteristic time delay between the formation of triplet excitons in dibenzothiophene and their migration to perylene-d12. Despite the uncertainty of the phosphorescence lifetimes, the approximate ratio of the two lifetimes does match well with the ratio found in single-molecule experiments.

3.3.3. POSSIBLE EXISTENCE OF MULTIPLE SITES

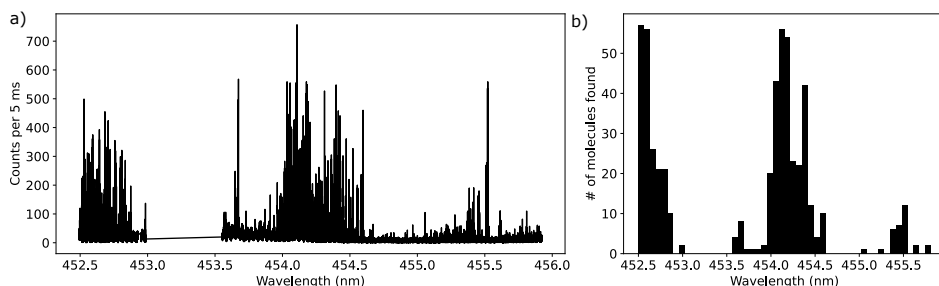


Figure 3.12.: Panel (a) shows a 6 MHz resolution broad range excitation spectrum of a single diffraction-limited focal area in a dibenzothiophene crystal doped with a low concentration of perylene-d12. The scan has a gap around 453 and 453.5 nm, while the rest was recorded. All the peaks are signatures of fluorescence from single molecules and obvious clustering into specific sites is present. Panel (b) shows the average number of molecules detected in a bin of size of 0.07 nm. A total number of 527 molecules are identified.

Although the ensemble fluorescence spectrum in Figure 2.4 of Chapter 2 does not reveal the existence of other spectroscopic sites, the peaks in the phosphorescence spectrum in Figure 3.9, unaccounted for by vibrations (such as the one at 69 cm^{-1}), could be a signature of other spectroscopic sites. Therefore, we studied excitation spectra of perylene-d12 in dibenzothiophene in more detail with another laser that was not present during the studies reported in chapter 2. With this laser (Sacher diode laser with tuning range of about 442-447 nm) we had easier control on scanning large spectral ranges, while avoiding manual adjustments that were necessary with the other laser. A large scan from 452.5 nm up to 456 nm, with a gap between 453 and 453.5 nm, reveals that single perylene-d12 molecules are present in a large spectral range. The main site around 454 nm is present in the scan. However, also additional sites around 452.5 nm and 455.5 nm are revealed. Both sites are approximately $70 \pm 10\text{ cm}^{-1}$ shifted in energy with respect to the main site's origin, which is very close to the peak at 69 cm^{-1} in the phosphorescence spectrum. Assuming that both the singlet and triplet states would shift by a similar amount of energy for the sites, the 69 cm^{-1} peak could indeed represent another spectroscopic site, possibly the one around 455.5 nm. This site would have a triplet state around $12,687\text{ cm}^{-1}$ (vacuum) or 788.4 nm (air). Alternatively, it could be that the second bump in the phosphorescence spectrum, around 145 cm^{-1} shifted from the main peak, thus at $12,611\text{ cm}^{-1}$ (vacuum) or 793.2 nm (air), is actually the phosphorescence from the red-most site at 455.5 nm. In that case, the main peak could correspond to the site around 452.5 nm, which does show a significant population in the histogram of Figure 3.12b. This has to be considered when looking for the triplet resonances on a single-molecule level.

3.4. CONCLUSION AND OUTLOOK

By excitation of dibenzothiophene's singlet excited state we have shown that there is efficient transfer of triplet excitons, acquired through intersystem crossing in the host, to the perylene-d12 molecules. However, the measurements have shown that the outcome of this experiment depends heavily on the quality of the dibenzothiophene. Only in the purest samples we were able to obtain a clear phosphorescence spectrum of perylene-d12, with a vibrational signature that confirms it. In addition, the phosphorescence spectrum reveals peaks that are not accounted for by vibrational peaks in the fluorescence spectrum. This could point to the existence of multiple spectroscopic sites, which are likely present, as observed in a broad-range excitation spectrum, measured by fluorescence.

The experiments could be refined by obtaining dibenzothiophene from a source that contains less impurities that are difficult to remove by zone-refining, for example by synthesis that already involves less impurities, such as the identified fluorene. In that case, the concentration of perylene-d12 could be significantly reduced in order to suppress inhomogeneous broadening in the spectrum and obtain a clearer phosphorescence spectrum. Moreover, the inhomogeneous broadening could be further reduced by improving the quality of the crystals by using co-sublimation techniques.

The spectroscopic studies on perylene's phosphorescence could be further extended by using microwaves to transfer populations of all the triplet sublevels to any of the single triplet sublevels, while measuring the phosphorescence spectrum as a function of microwave frequency and chopper frequency, based on microwave-induced delayed phosphorescence experiments. This way, changes in the quantum yield of phosphorescence can be measured while the population is transferred between triplet sublevels, as well as the ensemble-averaged zero-field splitting between the sublevels.

REFERENCES

- (1) Bree, A.; Zwarich, R. *Spectrochimica Acta Part A: Molecular Spectroscopy* **1971**, *27*, 621–630.
- (2) Zhao, W.; Cheung, T. S.; Jiang, N.; Huang, W.; Lam, J. W. Y.; Zhang, X.; He, Z.; Tang, B. Z. *Nature Communications* **2019**, *10*, 1595.
- (3) Dexter, D. L. *The Journal of Chemical Physics* **1953**, *21*, 836–850.
- (4) Goldacker, W.; Schweitzer, D.; Zimmermann, H. *Chemical Physics* **1979**, *36*, 15–26.
- (5) Ostapenko, N. I.; Sugakov, V. I.; Shpak, M. T., *Spectroscopy of Defects in Organic Crystals*; Springer Science & Business Media: 1993.
- (6) Schmidt, J.; Veeman, W. S.; van der Waals, J. H. *Chemical Physics Letters* **1969**, *4*, 341–346.
- (7) Bree, A.; Zwarich, R. *The Journal of Chemical Physics* **1969**, *51*, 903–912.
- (8) Walla, P. J.; Jelezko, F.; Tamarat, P.; Lounis, B.; Orrit, M. *Chemical Physics* **1998**, *233*, 117–125.
- (9) Clarke, R. H.; Hochstrasser, R. M. *Journal of Molecular Spectroscopy* **1969**, *32*, 309–319.
- (10) Kellogg, R. E.; Bennett, R. G. *The Journal of Chemical Physics* **1964**, *41*, 3042–3045.
- (11) Siebrand, W. *The Journal of Chemical Physics* **1967**, *47*, 2411–2422.
- (12) Fang, X.; Yan, D. *Science China Chemistry* **2018**, *61*, 397–401.
- (13) Giri, G.; Prodhan, S.; Pati, Y. A.; Ramasesha, S. *The Journal of Physical Chemistry A* **2018**, *122*, 8650–8658.
- (14) Zhu, Z.; Shu, X. *Optics Letters* **2018**, *43*, 2575–2578.

4

SINGLE MOLECULES IN A 2-D ELECTRIC FIELD

In this chapter a new host matrix for terrylene molecules, called [1]BenzoThieno[3,2-b]BenzoThiophene or shortly BTBT, is the center of study. We show that the insertion of terrylene inside a single crystal of BTBT leads to a non-centrosymmetric arrangement of host molecules around the terrylene molecule. In experiments, this comes forward by a moderately strong linear response to an electric field, caused by a change in dipole moment between ground and excited state of about 0.28 ± 0.09 Debye. In order to additionally resolve the direction of permanent dipole moments between the ground and excited state we made use of a simple geometry of electrodes that allowed us to direct an electric field at all in-plane angles.

The contents of this chapter are published in: R. Smit, Z. Ristanovic, I. Deperasinksa, B. Kozankiewicz and M. Orrit, Probing the in-plane dipole moment vector between ground and excited state of single molecules by the Stark effect, ChemPhysChem 2024, e202300881

4.1. INTRODUCTION

4.1.1. THE STARK EFFECT

Using molecular probes to sense electric fields at the nanoscale is a well-studied technique that started with cell membranes¹ and hole-burning experiments.² The interaction of a fluorescent molecule with an electric field manifests itself through a linear and/or quadratic shift of the optical resonance with field strength. The total shift of the optical resonance in an electric field perturbation is expressed as follows:

$$h\Delta\nu = -\Delta\vec{\mu}\cdot\vec{E} - \frac{1}{2}\vec{E}\cdot\Delta\overset{\leftrightarrow}{\alpha}\cdot\vec{E}, \quad (4.1)$$

where $\Delta\vec{\mu}$ is the permanent dipole moment vector and $\Delta\overset{\leftrightarrow}{\alpha}$ is the polarizability tensor, both measured as the difference between those quantities in the ground and excited state.

Usually, the quadratic Stark effect is dominant in the case the molecule under study is centrosymmetric, which is the case for the commonly-studied molecules in cryogenic single-molecule spectroscopy. Moreover, the quadratic Stark effect is always (ignoring exotic exceptions) negative and therefore the molecule's resonance can only shift in one direction. This is not a constraint for the linear component of the Stark effect, but it requires non-centrosymmetry. This can be achieved in two ways. One of them is changing the structure of the molecule by chemical substitutions, such that symmetry is broken.³ However, chemical substitutions may lead to unfavourable changes in photophysical properties, such as an increased intersystem crossing rate and/or changes in triplet lifetimes. Another possible consequence of chemical substitutions is an increased electron-phonon coupling, which can negatively influence the strength of the zero-phonon line.³ The alternative to chemical substitutions is the insertion of the centrosymmetric molecule into an environment consisting of a non-centrosymmetric arrangement of host molecules. This so-called host- or matrix-induced asymmetry has proven to yield the best of both worlds and effectively maintains the photophysical properties of the guest. For dibenzoterrylene (DBT), doped into a 2,3-dibromonaphthalene (DBN) matrix, the symmetry-breaking property of the host leads to a high linear Stark coefficient of 1.5 GHz/(kVcm⁻¹) at a narrow lifetime-limited linewidth of about 37 MHz.⁴ Even higher linear Stark shifts have been observed in semi-crystalline polyethylene doped with terrylene.⁵ However, unlike the aforementioned DBT in a DBN crystalline matrix, the linear Stark coefficients in the polymer matrix were broadly distributed due to disorder, while the optical resonances of the molecules were unstable.⁶

The sensitivity of molecules to electric fields, for instance for DBT in DBN, is large enough to detect a single charge at a distance of a few hundred nanometer and could compete with the charge sensitivity of single-electron transistors,⁷⁻⁹ while avoiding complex fabrication techniques. Moreover, with many molecules as electric field sensors inside the crystal, a charge could in principle be triangulated by mapping its electric field.⁷ However, despite narrowly-distributed linear Stark coefficients, the dipole vectors of single molecules can orient in several directions due to symmetry of the insertion site. In the case of DBT in DBN this results for instance in four different in-plane orientations,⁴ which are spectroscopically equivalent and typically hard to distinguish

with polarized excitation. In order to reliably triangulate single electrons or map electric fields by both direction and magnitude, the specific orientation of each molecule's dipole vector would have to be known.

In this work, we examine a method to determine for each molecule the angle and magnitude of the dipole vector. Using a quadrupole arrangement of electrodes we vary the direction of a mesoscopic electric field and measure the frequency shift of the molecule. This particular arrangement of electrodes has for instance been applied to defects in SiC¹⁰ or on NV centers in diamond.¹¹ To test this proof of principle on molecular crystals, we performed these experiments on a novel host matrix for single terrylene molecules, namely unsubstituted [1]BenzoThieno[3,2-b]BenzoThiophene, which will be abbreviated as BTBT from now on. We will show that the insertion of terrylene into a BTBT single crystal leads to a relatively strongly broken symmetry, inducing a dipole moment between ground and excited state of terrylene by about 0.28 ± 0.09 Debye. We complement our study by measurements of the spectroscopic and photophysical properties of terrylene in this new host matrix. Furthermore, we determine the orientation of terrylene molecules with polarized excitation and link these studies to quantum chemistry calculations on possible insertion sites for terrylene.

4.2. EXPERIMENTAL

4.2.1. CRYSTAL PREPARATION AND TRANSFER

BTBT was synthesized and purified by prof. Boleslaw Kozankiewicz from the Institute of Physics in Warsaw. All the procedures of synthesis and purification of BTBT are described in this paper.¹² Single crystals of BTBT doped with terrylene were obtained through co-sublimation in a 0.2 bar argon gas atmosphere at a temperature of about 200 °C, slightly below the melting point of BTBT (217-218 °C). The grown crystals have the form of thin plates of a few tens of μm thick and a surface area of about 10 mm². The fragile BTBT crystals were picked up with a sharp glass tip and deposited on the sample. With a small droplet of vacuum grease (Apiezon) it was made certain that the crystals remained in place during the cooldown with liquid helium.

4.2.2. PREPARATION OF QUADRUPOLE ELECTRODES

The four electrodes (see Figure 4.8) were patterned by e-beam lithography on a SiO₂-coated (300 nm) p-doped Si wafer (University Wafer) covered with a spin-coated bi-layer resist (400 nm PMMA 600 kDa and 250 nm PMMA 950 kDa). Both layers were cured for two minutes on a hot plate at 180 °C. After development of the exposed patterns and submersion in a 1:3 MIBK:IPA solution for 30 seconds, the structures were established by evaporating a 5 nm Cr adhesion layer and an 80 nm Au layer. Excess metal was removed by lift-off in heated acetone (45 °C) under continuous stirring. The metal pads were designed to be 0.75 mm apart from the junction area in order to avoid the optical objective from potentially shorting the Al wires (50 μm diameter) that were bonded between 200 μm^2 gold pads and their corresponding connections to the sample holder. The sample holder itself was connected to two analog

outputs of an Adwin Gold DAQ card. The remaining two electrodes were shorted with the ground plane.

4.2.3. CONFOCAL FLUORESCENCE MICROSCOPY SETUP

The measurements were acquired in a liquid-helium flow cryostat (Janis, SVT-200-5) that can reach a base temperature of 1.2 K. The samples were illuminated through a microscope objective (0.85 NA, Edmund Optics) immersed in the liquid helium, that forms a part of a home-built confocal setup. For the excitation we used a tunable Coherent 699 dye ring laser operated with Rhodamine 6G dye and pumped by a Coherent Verdi V2 laser (5 W at 532 nm). The effective tuning range extended from 560 to 620 nm, while the output wavelength was continuously monitored using a High Finesse WS6-200 wavemeter. Fluorescence was separated from the excitation light by a 615 LP filter (Chroma) and detected by either one or two (for Hanbury-Brown and Twiss experiments) avalanche photodiodes (Excelitas, SPCM-AQRH-16). Fluorescence spectra were recorded with a Horiba iHR320 spectrometer coupled to a liquid-nitrogen-cooled Symphony II CCD detector. Time-correlated single-photon counting was performed using a PicoHarp 300 from PicoQuant. For the start-stop experiments, a delay was imposed on the stop channel by a programmable delay box (Ortec DB463). The linear polarization of the excitation beam was controlled with a half-wave plate (Thor Labs, 588 nm zero-order) after cleaning up with a linear polarizer. The polarization state of the excitation beam was directly measured using a polarization analyzer (Schäfter+Kirchhoff SK010PA).

4

4.3. RESULTS AND DISCUSSION

4.3.1. LINE-NARROWING SPECTROSCOPY

The chemical structure of BTBT in Figure 4.1 shows that BTBT is an elongated aromatic molecule composed of two centro-symmetrically arranged thiophene rings in between two benzene rings. The origin of the optical absorption of BTBT was measured to be around 367.3 nm and the origin of the phosphorescence spectrum was found at 483 nm.¹² Therefore both the singlet and triplet excited states of BTBT are higher in energy than the singlet excited state of terylene (typically around 580 nm), avoiding quenching of the guest singlet by energy transfer to the host's singlet or intermolecular intersystem crossing to the host's triplet.¹³ A fluorescence spectrum of an ensemble of terylene molecules in BTBT reveals the existence of at least two spectroscopic sites (Figure 4.1). Multiple spectroscopic sites are not unusual for terylene in aromatic host matrices and were for example also found for terylene in *para*-dichlorobenzene,¹⁴ anthracene¹³ and *p*-terphenyl.¹⁵ The two sites we find are a blue site with origin around $16,869\text{ cm}^{-1}$ (593.0 nm) and a red site around $16,620\text{ cm}^{-1}$ (601.9 nm).

Based on the spectral intensities and the concentration of emitters in the fluorescent images of BTBT crystals, the red site appears to have a much higher population than the blue site (see Figure 4.2). In addition, the blue site is typically characterized by a strong background, which is likely caused by a coincidence of the vibronic line at

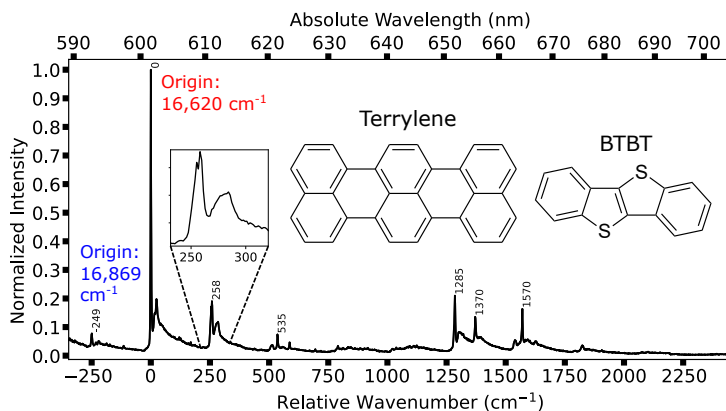


Figure 4.1.: Fluorescence spectrum of an ensemble of terrylene molecules in a BTBT host crystal, excited through a vibronic transition at a wavelength of 582.5 nm. The 0-0 ZPL of a red site peaks at $16,620\text{ cm}^{-1}$ (601.9 nm). Note that a feature on the blue side of this line arises from molecules in a blue site: origin at $16,869\text{ cm}^{-1}$ (593.0 nm). The Debye-Waller factor of the ensemble, as the ratio of the intensity of the 0-0 ZPL to the sum of the intensity of the 0-0 ZPL and the phonon side band, is 0.27 ± 0.03 .

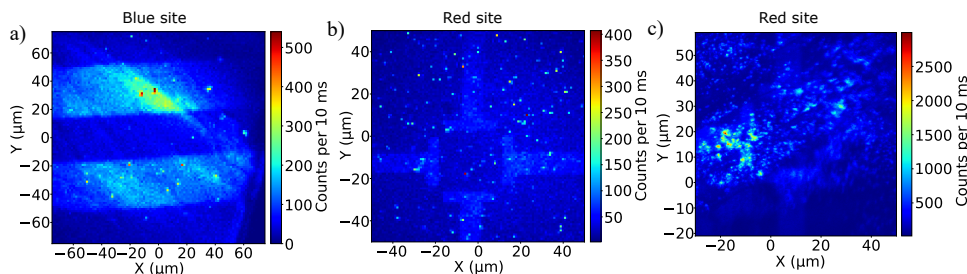


Figure 4.2.: Fluorescence maps of BTBT crystals, measured at different excitation wavelengths. In panel (a) the excitation wavelength was 591.95 nm. Panel (b) is taken at 604.2 nm and panel (c) is taken around 601.3 nm. The image in (a) corresponds to molecules in the blue site, while (b) and (c) are corresponding to the red site. Note that the concentration of fluorescent spots is much higher for (b) and (c), while the background is high in (a).

258 cm^{-1} of the red site with the 0-0 zero-phonon line (ZPL) of the blue site. This coincidence is noticeable from the fluorescence emission spectrum in Figure 4.1. The sharp peak is the 0-0 ZPL of the red site, while a weak signal from the blue site is visible around -249 cm^{-1} . The difference in wavenumbers between the two sites is indeed very close to the red site's strong vibronic line around 258 cm^{-1} . Noteworthy

is that the red site's spectral position is most red-shifted compared to previous studies of terrylene, where the most red-shifted site was obtained in para-dichlorobenzene at 597 nm.¹⁴ Furthermore, the red site's spectrum shows a splitting of the main vibronic line at 255-258 cm⁻¹. Such a splitting could be a signature of non-planar distortion of terrylene's molecular structure due to insertion in the BTBT crystal, which was similarly observed for terrylene in naphthalene,¹⁶ though with a more pronounced splitting of 13 cm⁻¹. As the red site is the most convenient site to study in terms of background, a high population of terrylene molecules and as we will show next, a better spectral stability as well, we will focus in our studies mainly on the red site.

4.3.2. PHOTOPHYSICAL PROPERTIES OF TERYLENE IN BTBT

4

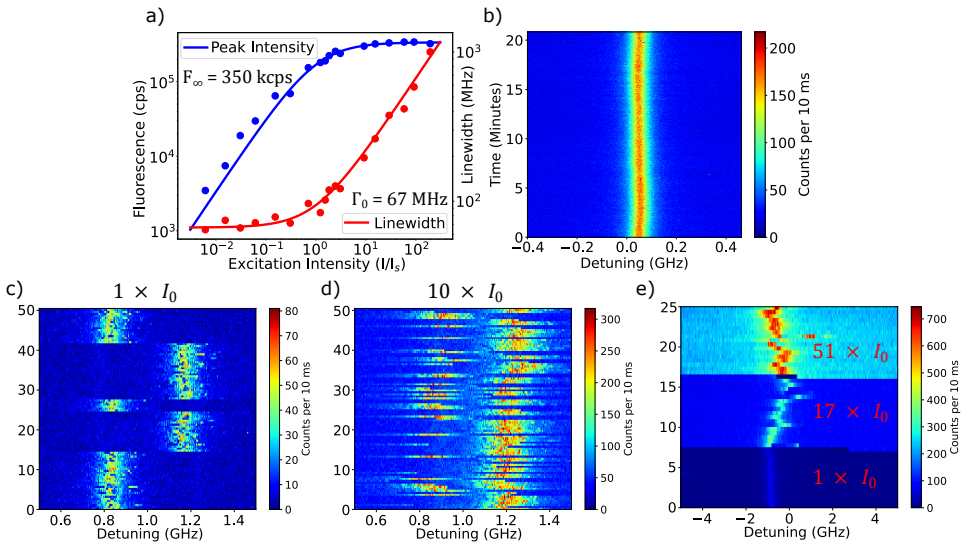


Figure 4.3.: Spectral properties of single terrylene molecules. Panel (a) shows the linewidth and fluorescence rate covered over four orders of magnitude in laser intensity for a molecule in the red site, shown here along with fits of the saturation intensity I_s . The estimated saturation intensity is in the order of 2 W/cm². The red data points are the measured linewidths, which are fitted to the broadening equation $\Gamma(I) = \Gamma_0\sqrt{1 + I/I_s}$. The blue data points are the measured fluorescence rates as a function of laser intensity, fitted to $F(I) = F_\infty(I/I_s)/(1 + I/I_s)$. Panel (b) shows another molecule in the red site that was followed in real time for more than 20 minutes with an integration time of 10 ms per point. Panel (c) and (d) show a molecule in the blue site that couples to a two-level system (TLS), that induces spectral jumps in the series of excitation spectra. Typical for TLSs, the jump rate scales with the excitation intensity. Panel (e) shows a molecule in the blue site that undergoes spectral diffusion upon increasing excitation intensities.

As typically reported for terrylene-doped single-crystal matrices, most terrylene molecules show an excellent spectral stability over longer time.^{14,15,17} One example of a spectrally-stable terrylene molecule is given in Figure 4.3b, which shows no spectral diffusion over the measured time of about 20 minutes. Most molecules in the red site are as stable as the molecule in Figure 4.3b, while unstable molecules tend to be more abundant in the blue site. These instabilities are particularly characterized by spectral jumps due to the presence of (tunnelling) two-level systems (see Figure 4.3c and 4.3d). Furthermore, spectral diffusion at excitation intensities beyond saturation is present in the blue site (Figure 4.3e). This might point to a photo-induced separation of charges in the host crystal.¹⁸

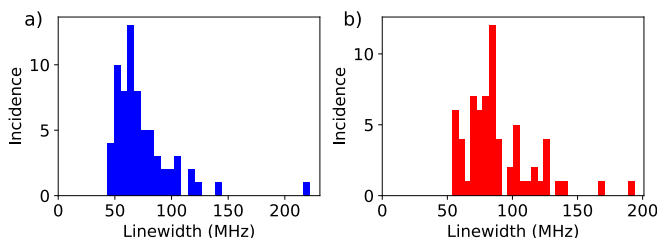


Figure 4.4.: Distributions of homogeneous linewidths of molecules in the blue site for panel (a) and molecules in the red site for panel (b). The excitation intensity was kept below typical saturation intensities to avoid power broadening of the resonances.

The homogeneous linewidth for the molecule in Figure 4.3a is about 67 ± 5 MHz, which is slightly broader than the narrowest linewidths found for terrylene in the red site: about 54 MHz (see distribution of linewidths for the blue and red site in Figure 4.4). However, a linewidth of 54 MHz remains broader than what is expected from typical lifetime-limited terrylene molecules reported in other matrices: ranging from 35 up to 45 MHz.^{17,19} To determine whether the homogeneous linewidth of 54 MHz is close to the lifetime-limited value, we performed antibunching measurements on single molecules in a Hanbury-Brown-Twiss configuration. We recorded the coincidence histogram of the emitted fluorescence photons with the laser at resonance with the 0-0 ZPL using a 256 ps binning time, while delaying the stop-pulse by 36 ns. As expected, Rabi oscillations appear at high laser intensities, shown in Figure 4.5.

Since the detection efficiency of our setup is around 10^{-3} , as determined previously in Chapter 2, we can relate the coincidence histograms, for the given time frame, directly to a correlation function.²¹ The correlation function for photons can be found by solving the optical Bloch equations with the Laplace transform (see derivation in Appendix 1), where we ignored contributions from the triplet state, which only adds photon bunching at longer timescales. The background causes a deviation from zero at the dip and can be taken into account by using the relation: $g_B^{(2)}(\tau) = 1 + \frac{1}{(1 + \frac{1}{\langle I \rangle})^2} (g^{(2)}(\tau) - 1)$, where $g_B^{(2)}(\tau)$ is the autocorrelation function that includes background, captured by the term B

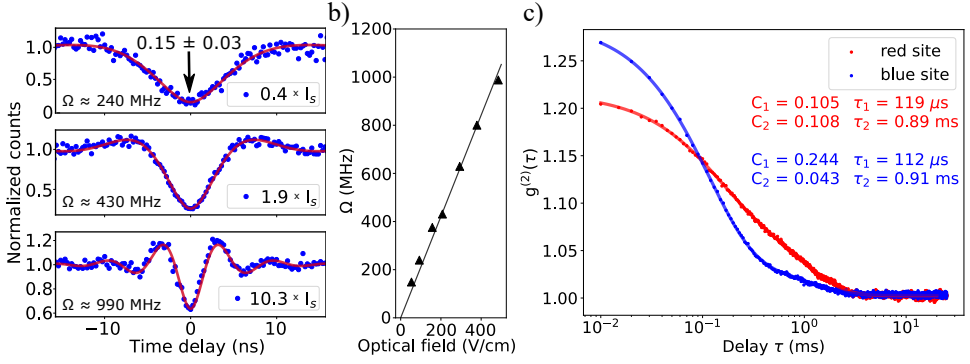


Figure 4.5.: Antibunching measurements on a single terrylene molecule at resonance with the 0 0 zero-phonon line, recorded for around 5 minutes per histogram. The three figures correspond to different excitation intensities, as units of the saturation intensity of about 2 W/cm^2 , where the fitted Rabi frequencies are given by Ω . The red curves are fits of the experimental data to equation 4.2. The data and fit were normalized to approach unity at timescales $\gg T_2$. b) Fitted Rabi frequencies Ω as a function of the estimated optical field intensity at the center of the focused Gaussian beam, using the relation $\Omega = |\mu_{12}| |E_{opt}| / \hbar$. The optical field intensities were estimated by $|E_{opt}| = \sqrt{(4\eta P)/(\pi w^2)}$, with $\eta = \sqrt{\mu_0(\epsilon_0 \epsilon_r)}$ being the wave impedance with $\epsilon_r \approx 3$, P the laser power corrected for losses and w the beam waist of about 500 nm. Neglecting an angle between the transition dipole moment μ_{12} and the optical field E_{opt} , the estimated transition dipole moment is about 1 Debye. Later, we will show that the transition dipole moment is estimated to be around 9.4 Debye using quantum-chemistry calculations. The deviation could be partly explained by the usual overestimation of the saturation intensity with respect to the true optical field at saturation.²⁰ c) Fluorescence-autocorrelation functions reveal bunching at the μs to ms time scale due to intersystem crossing (ISC) to the triplet state. The two curves represent data of single molecules in the red and blue sites, taken at about 3 times the saturation intensity. The data was fitted to a bi-exponential decay of the form $g^{(2)}(\tau) = C_1 \exp(-\tau/\tau_1) + C_2 \exp(-\tau/\tau_2)$, with the obtained parameters for both sites displayed in the image. The fit parameters show a clear difference in contrasts C_1 and C_2 among the two sites, while characteristic time scales for τ_1 and τ_2 are almost equal.

in relation to the average fluorescence signal $\langle I \rangle$. Finally, the normalized coincidence histograms were fitted to the following correlation:^{19,22}

$$g_B^{(2)}(\tau) = 1 - \frac{1}{\left(1 + \frac{B}{\langle I \rangle}\right)^2} \exp\left(-\frac{|\tau|}{2}(\pi\Gamma_0 + \gamma_{21})\right) \times \left[\left(\frac{\pi\Gamma_0 + \gamma_{21}}{2\tilde{\Omega}}\right) \sin(\tilde{\Omega}|\tau|) + \cos(\tilde{\Omega}|\tau|)\right], \quad (4.2)$$

with $\gamma_{21} = 1/T_1$ the decay rate of the excited state, $\pi\Gamma_0 = 1/T_2$ as the inverse of the coherence or dephasing time, and $\tilde{\Omega} = \frac{1}{2}\sqrt{4\Omega^2 - \gamma_{21}^2 - (\pi\Gamma_0)^2 + 2\pi\Gamma_0\gamma_{21}}$, where Ω is the Rabi frequency ($\Omega = |\vec{\mu}_{12}\vec{E}_{opt}|/\hbar$). The slope of the exponential following the dip is given by a sum of parameters that depend on T_1 and T_2 , which makes them difficult to separate from the antibunching measurements alone. Hence, we relate T_2 to the homogeneous linewidth $\Gamma_0 = 54$ MHz, which we obtained from the excitation spectra, through the relation $T_2 = 1/\pi\Gamma_0$. For four molecules, we measured and fitted antibunching curves at a range of excitation intensities, which results in an average excited state lifetime $T_1 = (\gamma_{21})^{-1}$ of 3.0 ± 0.2 ns. When calculating the lifetime-limited linewidth by $\Gamma_0 = 1/(2\pi T_1)$, the result corresponds to a linewidth of 53 ± 4 MHz, which indeed is close to the smallest linewidths found in this system and shows there is very limited additional decoherence. Nevertheless, this lifetime is on the short side for what was reported for terylene in other systems, with 3.15 ns being the shortest lifetime measured for terylene in anthracene.²³ The shortened lifetime for terylene in anthracene was explained by both an enhanced intersystem crossing through the host's triplet and a high refractive index of the anthracene host. Although no report of refractive indices for BTBT can be found, derivatives of BTBT, such as the less-dense polymerized C8-BTBT were reported to have high refractive indices of 1.74 and 1.6 along the out-of-plane and in-plane axes.²⁴ These refractive indices are relatively close to the refractive indices of anthracene.^{25,26} The reduced lifetime of terylene might therefore be related to a high refractive index of BTBT. In addition, a high refractive index, which can cause a stronger van der Waals interaction with the matrix, might (partly) explain the relative red-shift of the spectroscopic sites in BTBT.

At longer time scales of μ s to ms, time-correlated single-photon counting reveals the blinking properties of molecules in the two sites. Fluorescence time traces at resonant excitation were recorded and used for the calculation of the autocorrelation function $g^{(2)}(\tau)$. For molecules in both sites we can distinguish two exponential decays (see Figure 4.5c) in the autocorrelation, which are assigned to the in-plane T_{xy} -triplet substates for the short decay and the out-of-plane T_z -triplet substate for the long decay.^{15,27} For the blue site, the T_z component is relatively weak, which is not the case for the red site. The autocorrelations were recorded at different excitation intensities and processed in a global fit (see procedure also in Chapter 2), together with a saturation and linewidth broadening curve such as in Figure 4.3a and Figure 4.6a and 4.6d. Disregarding inhomogeneity in the ISC rates of single molecules within the sites, the difference among the sites is not that significant (see Table 4.1). For example, in a pentacene-doped *p*-terphenyl matrix the ISC rates were varying by over two orders of magnitude among spectroscopic sites.²⁸ However, the triplet lifetimes we find for the two sites are for both the T_{xy} -triplet substate and the T_z -triplet substate about a factor 3 shorter than typically reported for terylene in other matrices, such as *p*-terphenyl^{15,29} and terylene on hBN in Chapter 5. The shorter lifetimes might be the result of a

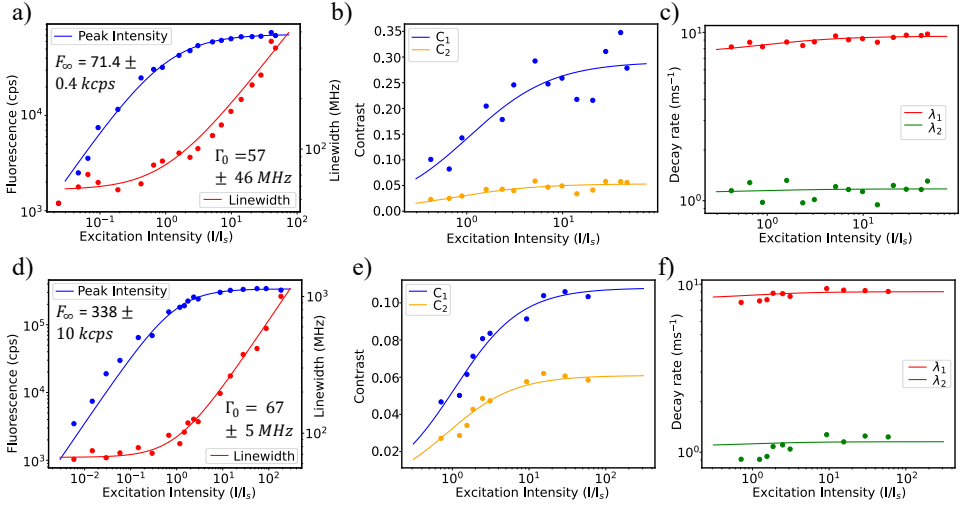


Figure 4.6.: Global fits for the saturation of fluorescence and power broadening of the linewidth are shown in panel (a) and panel (d), combined with fit parameters for the autocorrelation functions, such as contrasts of the exponential decays in panel (b) and panel (e) and decay parameters in panel (c) and panel (f), taken at a range of excitation intensities. The top panels correspond to a molecule in the blue site, while the bottom panels correspond to a molecule in the red site. The resulting parameters obtained from the global fits are displayed in Table 4.1.

heavy-atom effect and/or distortion of the terrylene molecule in its site.

Site	Position (cm^{-1})	Linewidth : Γ_0 (MHz)	ISC rate : γ_{23}^{xy} (s^{-1})	Lifetime : $(\gamma_{31}^{xy})^{-1}$ (μs)	ISC rate : γ_{23}^z (s^{-1})	Lifetime : $(\gamma_{31}^z)^{-1}$ (ms)
Blue	16,869	43	4000 ± 300	134 ± 3	170 ± 50	0.9 ± 0.1
Red	16,620	54	1900 ± 400	125 ± 15	300 ± 80	1 ± 0.2

Table 4.1.: Spectroscopic and photophysical properties of the blue and red site. The intersystem crossing (ISC) rates and lifetimes of the two distinguishable triplet states, are derived from correlation functions $g^{(2)}(\tau)$, recorded at different excitation intensities. Since these parameters for ISC and triplet lifetimes concern single-molecule measurements they may be affected by the inhomogeneity of the molecules' environment.

4.3.3. DETERMINATION OF DIPOLE VECTORS WITH A 2-D ELECTRIC FIELD

As explained in section 4.1.1., the linear Stark effect requires a change in the electric dipole moment between ground and excited state, which is a vector: $\Delta\vec{\mu}$. In the regime of voltages that we applied, we observed a moderately strong linear Stark shift with a negligible quadratic component. The dominance of the linear Stark shift is not trivial, as both the BTBT host and terrylene are centrosymmetric. Therefore the change in dipole moment between ground and excited state must be induced by a symmetry-breaking insertion into the host's crystal lattice.⁴

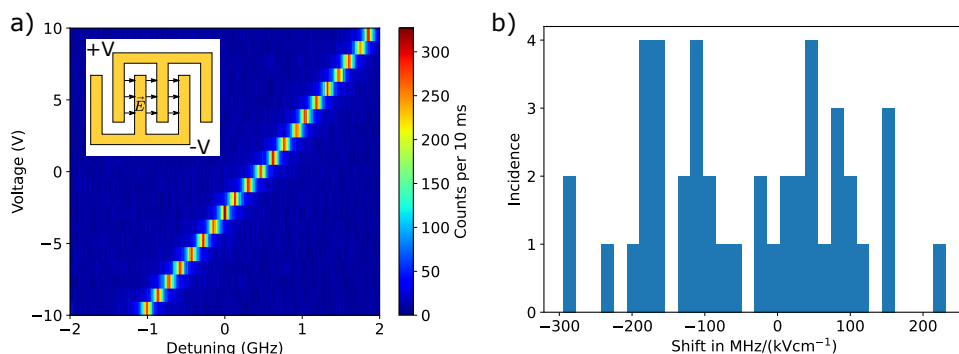


Figure 4.7.: Panel (a) shows the response of a single molecule in the blue site to an incremental electric field between interdigitated electrodes, which are schematically drawn in the figure inset. Panel (b) shows the distribution of Stark coefficients for 44 single molecules that are measured in the same range as the molecule in panel (a).

We started with typical Stark effect measurements, where a set of parallel electrodes are used to impose an electric field in one dimension (see schematic in inset of Figure 4.7a). However, the strength of the measured Stark effect depends on the direction of the dipole vector $\Delta\vec{\mu}$, which due to symmetry of the insertion site can have different projections on the imposed electric field. These projections of $\Delta\vec{\mu}$, together with inhomogeneities of $\Delta\vec{\mu}$ from molecule to molecule due to different charge environments, resulted in a complex distribution of Stark coefficients, as shown in Figure 4.7b.

To reduce the complexity of the measured Stark coefficients, by measuring the Stark effect independently of the alignment of the crystal to the electrodes, we designed a quadrupole structure with four independently-connected electrodes (Figure 4.8a). The crystal is mounted on top of these four electrodes (Figure 4.8b). We apply a bias on the horizontal and vertical electrode pair (Figure 4.8d). With COMSOL simulations in Figure 4.8d we show that the electric field is mostly homogeneous at the center and moreover we find that the superposition principle of the horizontal and vertical electric field applies, which makes it possible to orient the field in all in-plane directions. These

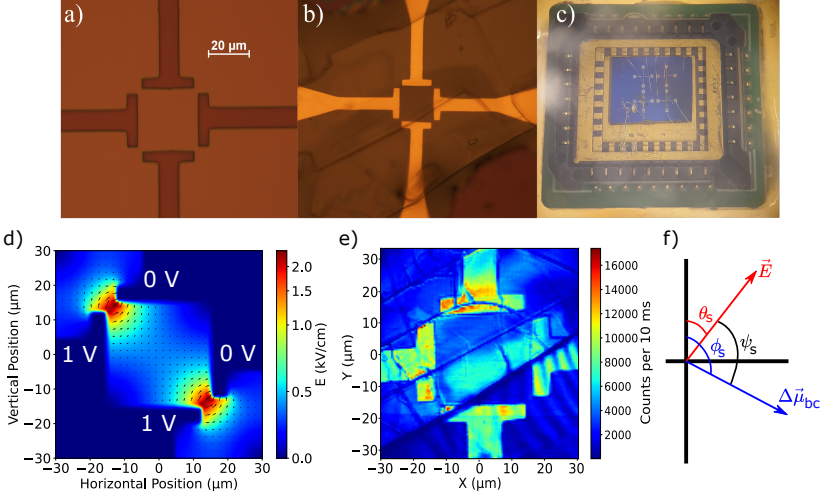


Figure 4.8.: Panel (a) shows the patterned electrodes in the e-beam resist layer. In panel (b) the structures have been filled with gold and a BTBT crystal is mounted on top. The sample is attached to a holder and wire bonded in panel (c) in order to apply voltages to the electrodes. The simulated electric field is shown in panel (d) for a case of symmetric voltages on the horizontal and vertical electrode pairs. Panel (e) shows the confocal reflection image of the mounted crystal that was used in low-temperature experiments. The definitions of the angles used in equation 4.3 are shown schematically in panel (f).

simulations are performed in two dimensions and do not take the substrate or any other anisotropies in the environment into account. Furthermore, the simulations show that the field at the center is a factor 1.2 weaker compared to the naive case where the field is equal to the potential difference divided by the distance between the electrodes (30 μm). This is likely due to concentration of the field between the side tips of the electrodes. The factor of 1.2 was taken into account when fitting experimental data to theory.

As the crystal itself is three-dimensional, the applied electric field is only sensing the projection of $\Delta\vec{\mu}$ in the crystallographic bc -plane, due to the crystalline structure of BTBT.³⁰ The linear shift of the resonance frequency of the single molecules is given by the scalar product of the two vectors $-\Delta\vec{\mu}\cdot\vec{E}$. Taking into account only the components that are in the plane of the electric field and neglecting crystal anisotropy, the magnitude of the shift reduces to:

$$h\Delta\nu = -|\Delta\vec{\mu}_{bc}||\vec{E}|\cos\psi_s, \quad (4.3)$$

where ψ_s indicates the angle between the dipole moment $\Delta\vec{\mu}_{bc}$ and the electric field \vec{E} . When we center our frame of reference around the electric field, given by angle θ_s , and defining an angle for the dipole vector, as ϕ_s , the angle ψ_s can be written as $\psi_s = \phi_s - \theta_s$ (see Figure 4.8f).

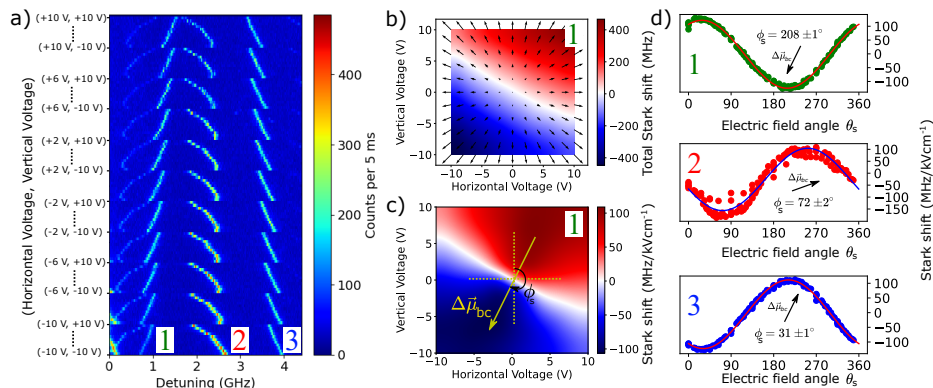


Figure 4.9.: a) Series of 121 single excitation spectra that records the response of molecules in the same focal volume to changing electric field. The scans start with -10 V on both the bottom and left electrode and progresses with a sweep of the voltage on the left electrode from -10 V to 10 V in 11 steps. Subsequently, the voltage on the bottom electrode is increased followed by another sweep of the voltage on the left electrode. Two different patterns can be observed, with molecules moving in both directions. Panel (b) depicts the shift of molecule 1 in (a) for all voltage combinations. The relative magnitude and direction of the applied electric field, in the center between the four electrodes, are plotted as arrows. Panel (c) shows the shifts in (b), normalized for the magnitude of the electric field vector. The direction of the dipole vector and its angle are plotted in the center. (d) The relative magnitude of the Stark effect for the three molecules in (a) is plotted as a function of electric field angle θ_s and fitted to equation 4.3 as $\Delta\mu|\vec{E}| = -|\Delta\vec{\mu}_{bc}|\cos(\theta_s - \phi_s) + offset$, where ϕ_s is the angle of the dipole vector $\Delta\vec{\mu}_{bc}$. The experimental data in (b) and (c) have been smoothed by bicubic interpolation.

With a predefined step size in voltage, all combinations of horizontal and vertical biases are applied within the range of -10 V to +10 V. For each of the combinations, we recorded an excitation spectrum around the molecule's 0-0 zero phonon line (Figure 4.9a) and fitted this to a Lorentzian distribution to determine its resonance frequency. For all bias combinations, the observed shift of molecule 1 in Figure 4.9a is plotted in Figure 4.9b, where the arrows indicate the electric field direction and magnitude for the corresponding combination of voltages. On the diagonal there is a clear region of white color where little to no shift is observed, even though an electric field is applied. This corresponds to the case where the angle ψ_s is close to 90° . The other diagonal, orthogonal to the white region, represents the direction where the electric field and dipole vector are parallel. On this diagonal, the dipole vector orients in the direction where the Stark shift is negative (equation 4.3). The orientation found for the dipole of

molecule 1 is drawn in Figure 4.9c. For the three molecules in Figure 4.9a, the dipole orients in different directions shown by their relationship with field orientation in Figure 4.9d. Overall, molecule 1 and 3 show good agreement with equation 4.3, while molecule 2 shows more variation. Moreover, the curve of molecule 2 displays a relatively strong asymmetry between positive (up to $+100 \text{ MHz}/(\text{kVcm}^{-1})$) and negative values (down to $-150 \text{ MHz}/(\text{kVcm}^{-1})$). In addition, the curve shows nonlinear behaviour for sweeps at different voltage combinations, where the electric field vector points roughly in the same direction, but with a different magnitude (different rows in Figure 4.9b). This may point to an accumulation of charge, which is not observed for molecule 1 and 3. Despite the variations for molecule 2, the angle of the dipole vector can be measured with good accuracy.

4

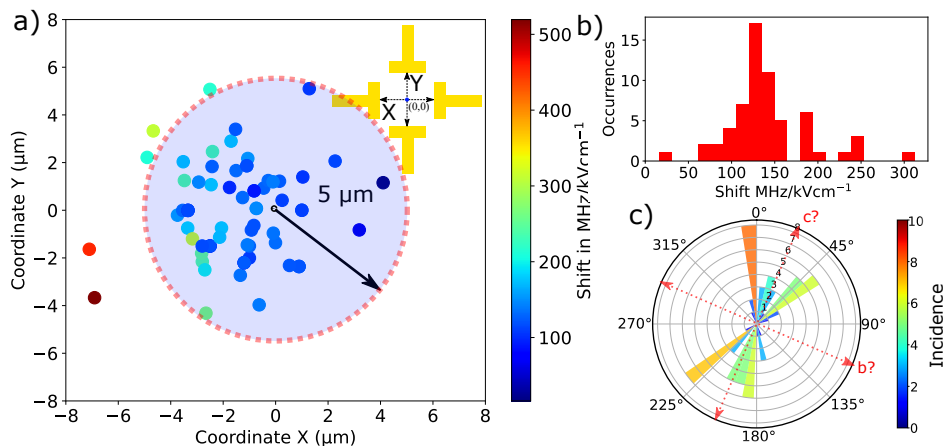


Figure 4.10.: a) Scatter plot of the measured Stark coefficients (maximum shift per unit electric field when the electric field and dipole vector align) of 69 molecules, positioned at their locations with respect to the four electrodes. A circle with radius of $5 \mu\text{m}$, drawn from the center between the four electrodes at $(0,0)$, selects the 64 molecules that are closest to the middle and have been plotted in a histogram in panel (b). The distribution of the angles of the dipole vector are plotted in panel (c). Here, the width of the bars indicate the bin size of 9° per bin and both the length and color indicate the number of molecules that are present within each bin. The red dashed arrows indicate possible symmetry axes for the dipole vectors, which based on the insertion sites in section 4.3.5 could relate to the noted crystallographic axes (bbc insertion site in Table 4.2).

To gather statistics on the orientation of the dipole vectors in the red site, we performed measurements such as in Figure 4.9 for a total of 69 molecules. The in-plane position of each molecule was measured, such that the molecules close to the center of the four electrodes could be selected. The Stark coefficient of each molecule is

scatter-plotted by its spatial position in Figure 4.10a. From the plot it becomes clear that outliers, in terms of Stark shift, are indeed further away from the center, where there is either a weak or an enhanced field in the gap between the electrodes (Figure 4.8d). Closer to the center position, the spread in values is lower and a histogram of the maximum magnitude of the Stark shift, for molecules inside a circle with a radius of 5 μm , reveals a relatively narrow distribution (Figure 4.10b). The average slope of the Stark shift was measured to be $140 \pm 47 \text{ MHz}/(\text{kVcm}^{-1})$ and this corresponds to an in-plane dipole moment $|\Delta\vec{\mu}_{bc}|$ of 0.28 ± 0.09 Debye, which is not corrected for local-field effects around the molecule.³¹ The uncertainty of $|\Delta\vec{\mu}_{bc}|$ can be explained by variations in the electric field further off-center, while also different axial positions of the molecule and charge inhomogeneities around the molecules may contribute to variations of the dipole vector magnitude.

The angle of the dipole moment vector shows a relatively broad distribution (Figure 4.10c). Although these observations are only for the red site, a broad distribution of angles, possibly due to crystal symmetry, may likewise explain the large variations we observed for the magnitude of the Stark effect with a 1-D electric field for the blue site (Figure 4.7b). The distribution for the red site shows that there are at least two populations of molecules, spanning also the opposite quadrant. The drawn dashed lines might be the symmetry axes of the polar distribution. However, the many systems of cracks, possibly also step edges, in Figure 4.8e made it difficult to relate these lines to crystallographic axes. Nonetheless, the observation of a relatively narrow distribution of linear Stark coefficients, and thus non-random orientations for dipole vectors, points to a symmetry that is broken by the host matrix BTBT. This will set a limit to the possible insertion sites. However, an additional method to determine possible insertion sites is by measuring another vector, namely the direction of the transition dipole moment $\vec{\mu}_{12}$. For terrylene, the transition dipole moment follows the long axis, and thus reveals the alignment of the terrylene molecules inside the crystal.

4.3.4. THE TRANSITION DIPOLE MOMENT OF TERRYLENE

The transition dipole moment of terrylene, $\vec{\mu}_{12}$, which follows the long axis of the molecule, couples to the optical field \vec{E}_{opt} , inducing (Rabi) oscillations between ground and excited state. The coupling between $\vec{\mu}_{12}$ and \vec{E}_{opt} is optimal when the two vectors are parallel. This is achieved by converting the laser light to a linearly-polarized state with a polarizer, while a half-wave plate can tune the angle. As a function of the angle between $\vec{\mu}_{12}$ and \vec{E}_{opt} , called ψ_p , the fluorescence intensity varies by a $\cos^2(\psi_p)$ relationship.

Before we determined the angle of the transition dipole moment for the crystal in Figure 4.11a, we made sure which crystal cracks represented crystallographic axes, to serve as reference axes for $\vec{\mu}_{12}$. To determine the crystallographic axes we illuminated a BTBT single crystal with white light between crossed-polarizers. As we rotated the crystal, the crystal turned dark at the four angles where the linearly-polarized light aligned with a crystallographic axis. At in-between angles, the crystal was bright and colourful due to birefringence. The extinction angles coincided with the edge of

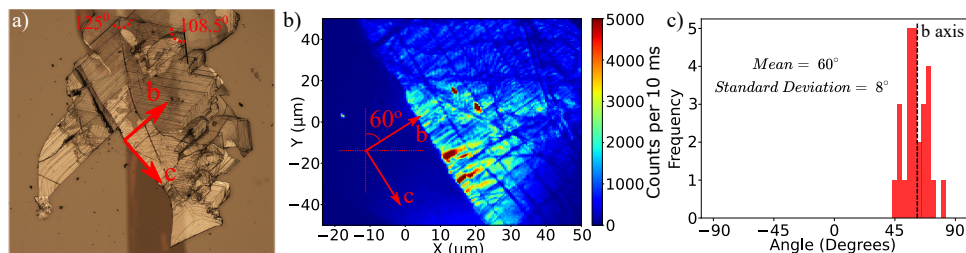


Figure 4.11.: Panel (a) shows a microscope image of the crystal with the annotated crystallographic axes deduced from the structure of the crystal (see angles) and birefringence measurements. Panel (b) shows a confocal microscope image of a part of a BTBT single crystal, taken around the arrows in (a). c) Histogram of the transition dipole moment angle with respect to the axes shown in (b) for 26 different molecules. The average angle is around 60° with a standard deviation of 8° . The angle corresponds to the b-axis, which is perpendicular to the crystal edge.

4

the crystal and a set of lines perpendicular to the edge, as shown in Figure 4.11b. However, many lines, of which some were possibly step edges, did not coincide with a crystallographic axis and confirm that it is difficult to assign crystallographic axes from series of cracks in the crystals alone.

Single molecules in the red site were excited resonantly by the 0-0 ZPL and their intensity was monitored in the series of excitation spectra, where each line was measured with a different polarization angle (Figure 4.12a and 4.12b). We changed the polarization of the laser light in a range of 180° , which was sufficient to determine the axis of $\vec{\mu}_{12}$. The intensity of the molecule at various polarization angles is fitted to $I(\theta) = B + A \cos^2(\phi_p - \theta_p)$, where ϕ_p represents the axis of $\vec{\mu}_{12}$, B the background and A the amplitude. This procedure was repeated for 26 molecules and plotted in a histogram in Figure 4.11c, which shows there is a relatively narrow distribution of transition dipole moments around the b axis, resolved from the outer structure (Figure 4.11a). The same angle of $\vec{\mu}_{12}$ was found at room temperature, where both sites and inhomogeneities have been ensemble averaged (Figure 4.12d). The similarity of BTBT to anthracene, which crystallizes in the same form, supports an insertion of terrylene along the b-axis.³² An insertion along the b-axis was found for DBT in anthracene, which apart from the two outer benzene rings closely resembles the shape of terrylene.

Taking into account the measured orientation of terrylene along the b-axis of BTBT and the broken symmetry of terrylene by the host, we can start to relate our measurements to a possible insertion site. These calculations were performed by Irena Deperasińska from the Institute of Physics in Warsaw (Poland).

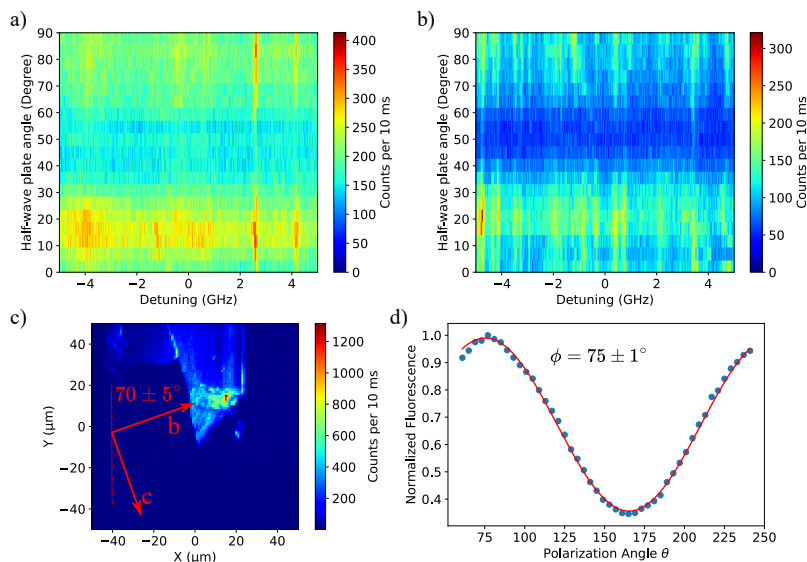


Figure 4.12.: Panels (a) and (b) represent low-temperature excitation spectra of respectively the blue and the red site as a function of half-wave plate angle. Molecules of the two sites follow the same pattern. Panel (c) shows the orientation of the crystallographic axes in a room-temperature measurement. In panel (d) we find a cosine-squared relation of the fluorescence with the polarization angle again. As this measurement was taken at room temperature, different sites cannot be distinguished and this shows that most molecules align with the b-axis. The background does not fully extinguish and may be caused by ill-inserted molecules in the crystal.

4.3.5. PROPOSED INSERTION SITES

The equilibrium structure of terylene inside the BTBT crystal cavities was optimized in the ground (S_0) and excited (S_1) electronic state with Gaussian16³³ using the procedure ONIOM(B3LYP/6-31G(d,p): PM3), i.e. with the semiempirical PM3 method describing the rigid crystal structure of BTBT and B3LYP and TD B3LYP/6-31G(d,p) methods for terylene. The cavities inside the BTBT crystal were formed by taking out 2 and 3 BTBT molecules from a crystal element of 48 molecules in a pattern as previously described for DBT in 2,3-dibromonaphthalene⁴ and in anthracene crystals.³² The Franck-Condon factors for the $S_0 \rightarrow S_1$ transition were calculated with a procedure included in Gaussian16. The spin-orbit coupling matrix elements between the singlet and triplet states were calculated with ORCA 4.2.1³⁴ as square root of the sum of squares of spin-orbit coupling matrix elements of all triplet state sublevels of the uncoupled states.

The calculations on the properties of terylene in the BTBT host crystal rely on the optimization of the structure of the guest molecule embedded in a cavity obtained by removing the appropriate number of host molecules. In the context of the present work

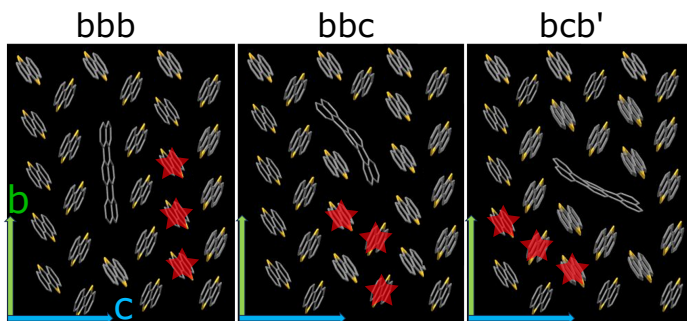


Figure 4.13.: Optimized geometry of terrylene in the three considered cavities, created by the removal of three molecules of BTBT. The red asterisks indicate which molecules have been removed in order to form the cavity for terrylene. The green arrow indicates the b axis and blue the c axis of the BTBT crystal.

4

our interest is concentrated around the cavities in which terrylene orients with its long axis mostly parallel to the crystallographic b axis. The three possible sites, called bbb, bbc and bcb', are presented in Figure 4.13.

In Table 2, the calculations of terrylene in the three sites are shown. Here, we present the calculated (0,0) transition energies, permanent dipole moments in the S_0 and S_1 states and the transition dipole moments. Additional calculational results are presented in Tables 3, 4 and 5.

The calculations show that the terrylene molecule loses its planar symmetry. For example, the long axis of the terrylene molecule is slightly longer than twice the distance between BTBT molecules along the b axis, thus a molecule in the cavity bbb is forced to „compensate” this incompatibility by a small deviation from planarity. On the other side, the cavity bbc (Figure 4.13 forces terrylene to be bent in a bow (Figure 4.13), which results in a considerably higher dipole moment than in the two other cases.

In view of the results of the calculations, a lack of planar symmetry of the terrylene molecule is indicated by the appearance of new vibronic lines, absent in the spectrum of isolated (thus planar) terrylene (see Figure 4.14), as well as the appearance of a permanent dipole moment (Table 4.2 and Table 4.4). Other signatures of the symmetry loss are the positive (non-zero) elements of the spin-orbit coupling (Table 4.3).

Out of the three possible cavities occupied by a terrylene molecule, the site bbc seems to be the closest to the experimental red site. Arguments for this assignment are the following:

- i) the calculated 0-0 ZPL is most red-shifted (Table 4.2)
- ii) the dipole moment $|\Delta\mu| = \mu(S_1) - \mu(S_0)$ has the highest value, although lower than

Site		<i>a</i> - axis	<i>b</i> - axis	<i>c</i> - axis	$ \mu $
bbb $\lambda(0,0) =$ 603.7 nm	$\mu(S_0 \rightarrow S_1)$	0.274	-9.43	-0.216	9.436
	$\mu(S_0)$	-0.330	-0.108	-0.095	0.360
	$\mu(S_1)$	-0.354	-0.106	-0.102	0.383
	$\mu(S_1) - \mu(S_0)$	-0.024 (-0.004)	0.003 (-0.050)	-0.007 (0.001)	0.023 (0.050)
bbc $\lambda(0,0) =$ 607.1 nm	$\mu(S_0 \rightarrow S_1)$	0.384	8.020	-4.649	9.278
	$\mu(S_0)$	0.456	0.013	-1.756	1.815
	$\mu(S_1)$	0.429	-0.062	-1.648	1.704
	$\mu(S_1) - \mu(S_0)$	-0.027 (-0.064)	-0.074 (-0.102)	0.108 (0.182)	0.111 (0.218)
bcb' $\lambda(0,0) =$ 604.1 nm	$\mu(S_0 \rightarrow S_1)$	-1.642	6.783	6.329	9.422
	$\mu(S_0)$	-0.478	0.303	-0.414	0.701
	$\mu(S_1)$	-0.530	0.301	-0.437	0.750
	$\mu(S_1) - \mu(S_0)$	-0.052 (0.016)	-0.002 (0.001)	-0.023 (0.006)	0.049 (0.016)

Table 4.2.: Results of the ONIOM(B3LYP/6-31G(d,p):PM3) calculations for terrylene embedded in the considered cavities in the BTBT crystal. The quantity $\lambda(0,0)$ is the energy of the (0,0) transition with the zero-point energy correction (more details in table 3), $\mu(S_0 \rightarrow S_1)$, $\mu(S_0)$ and $\mu(S_1)$ are the dipole moments (in Debye) for the $S_0 \rightarrow S_1$ transition, and in the S_0 and S_1 states. Their components are presented along the crystal axes. For isolated terrylene $\lambda(0,0) = 604.3$ nm and $\mu(S_0 \rightarrow S_1) = 9.443$ D. In the rows for $\mu(S_1) - \mu(S_0)$ we show, between parentheses, the results of calculations with use of the simple but uniform B3LYP/3-21G method for the whole system (taken in the geometries optimized by ONIOM).

	isolated	bbb	bbc	bcb'
<i>Transition energies from S_0 state (nm)</i>				
S_1	554.7	554.8	561.7	558.1
T_1	1221.8	1221.8	1259	1240.3
T_2	549.6	549.7	552.5	551.9
<i>SOC matrix elements (cm^{-1}) between T_i and S_k</i>				
T_1/S_0	0.0	0.16 (0.27)	0.58 (0.19)	0.12 (0.17)
T_1/S_1	0.0	0.00	0.00	0.02 (0.00)
T_2/S_0	0.0	0.16 (0.27)	0.40 (0.34)	0.33 (0.09)
T_2/S_1	0.0	0.04 (0.25)	0.26 (0.24)	0.07 (0.30)

Table 4.3.: H_{SO} - Spin-orbit coupling matrix elements between the singlet and triplet states. In parenthesis we show the fraction of the z-component relative to the x and y components: $H_{SO,z}/H_{SO,xy}$.

the experimentally determined 0.28 ± 0.09 D (0.111 D obtained by the ONIOM method, and 0.218 D by using simple B3LYP/3-21G). In addition, the dipole vector has the highest value along the crystallographic axes b and c (Table 4.2), as suggested from the experiment. The calculated in-plane dipole vector orients about 30° with the c-axis, which indicates that the orientations found for the dipole vectors center around the crystallographic axes drawn in Figure 4.10c, with possibly four distributions resulting from the four possible, and spectroscopically

Site	Dipole Moment	$ \mu $ (Debye)	X	Y	Z
<i>Isolated</i>	$\mu(S_0 \rightarrow S_1)$	9.4430	0.0000	9.4430	0.0000
<i>bbb</i>	$\mu(S_0 \rightarrow S_1)$	9.4346	0.0008	-9.4346	0.0086
	$\mu(S_0)$	0.0299	-0.0016	-0.0018	-0.0298
	$\mu(S_1)$	0.0401	-0.0255	0.0025	-0.0308
<i>bbc</i>	$\mu(S_0 \rightarrow S_1)$	9.2768	0.0043	9.2768	0.0053
	$\mu(S_0)$	0.3745	-0.0060	-0.0244	0.3736
	$\mu(S_1)$	0.3275	-0.0118	-0.0145	0.3269
<i>bc b'</i>	$\mu(S_0 \rightarrow S_1)$	9.4219	0.0023	9.4219	0.0279
	$\mu(S_0)$	0.0428	0.0033	0.0418	0.0086
	$\mu(S_1)$	0.0596	0.0216	0.0544	0.0046

Table 4.4.: Components of the dipole moments for terrylene taken from the sites and shown in the standard XYZ orientation (XY is the plane of Tr, Y is the direction of the long axis)

4

equivalent, in-plane orientations of the *bbc* site.

- iii) Although the transition dipole moment vector is mostly aligned with the crystallographic b-axis, the bent structure of terrylene creates an angle of about 30° with this axis b. However, the only possible insertion that follows exactly the b-axis is site *bbb*, but the centrosymmetric arrangement of host molecules around terrylene in this site would lead to an effective zero dipole moment. The width of the distribution in Figure 4.11c does not exclude the possibility of a small angle of the transition moment with the b axis.
- iv) The highest spin-orbit coupling was calculated for the site *bbc*.

4.4. CONCLUSION

Terrylene molecules embedded in a single crystal of BTBT possess favourable spectroscopic properties in terms of homogeneous linewidths and spectral stability. Furthermore, the studies we performed on the red-most spectroscopic site show that the host matrix induces a broken symmetry of the otherwise centrosymmetric terrylene, giving rise to a net in-plane dipole moment of 0.28 ± 0.09 Debye oriented in four in-plane directions. Although the induced net dipole moment could be classified as moderate, when for example compared to dibenzoterrylene (DBT) in 2,3-dibromonaphthalene, the magnitude of the dipole vector is still remarkable and might point to a strong influence of the sulphur atoms on the charge distributions in the ground and excited state. For DBT in DBN it was found that mostly the side wings of DBT, which terrylene lacks, were responsible for the induced dipole through the host's bromine atoms.⁴ In the case of the BTBT host, the effect of the sulphur atoms on the guest molecule could perhaps be strengthened by replacing terrylene with DBT.

Our reported method on the control of the electric fields' direction, applicable to any crystal, makes it possible to determine the dipole vector for each molecule individually,

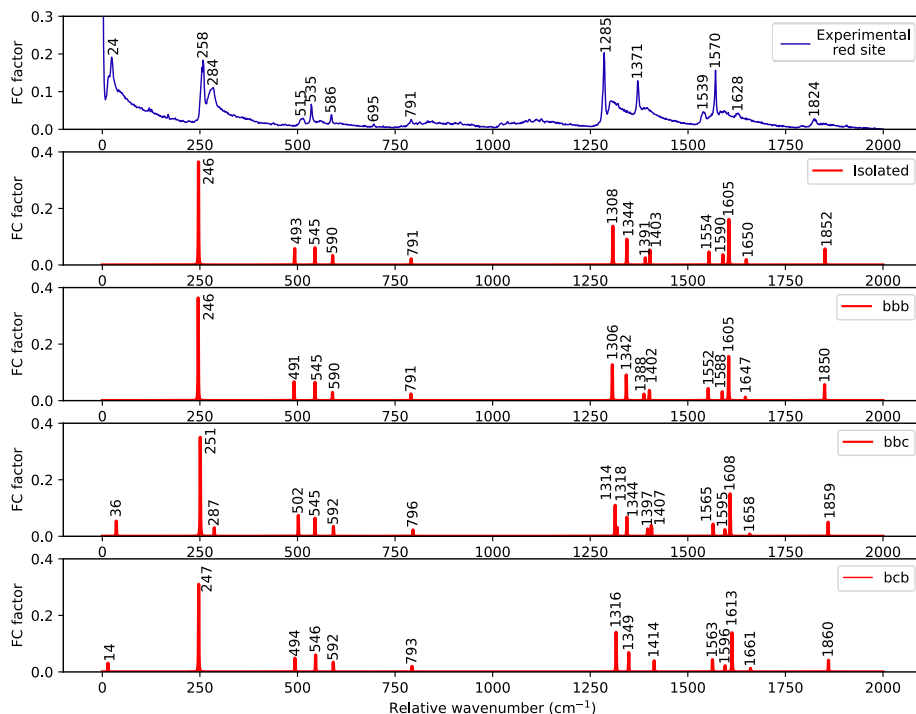


Figure 4.14.: Spectroscopic data for terrylene optimised in the BTBT crystal as a result of calculations by the ONIOM(B3LYP/6-31G(d,p):PM3) method (data in red). The calculations are compared to the experimental data of Figure 4.1 (data in blue)

which would make the use of these molecules for mapping electric fields, by direction and magnitude, or tracing charges, more reliable. In the future, the electric field control could be extended to three dimensions, by using the substrate's p-doped silicon layer as an additional electrode and an ITO cover glass as a top electrode for out-of-plane measurements of the dipole. Moreover, the good hole-conduction properties of BTBT and linear response of molecules to electric field, makes this an interesting system for the study of the injection of charges, for example by a field-effect transistor configuration.³⁵

REFERENCES

- (1) Davila, H. V.; Salzberg, B. M.; Cohen, L. B.; Waggoner, A. S. *Nature New Biology* **1973**, *241*, 159–160.
- (2) Marchetti, A. P.; Scozzafava, M.; Young, R.-H. *Chemical Physics Letters* **1977**, *51*, 3.
- (3) Faez, S.; Verhart, N. R.; Markoulides, M.; Buda, F.; Gourdon, A.; Orrit, M. *Faraday Discussions* **2015**, *184*, 251–262.
- (4) Moradi, A.; Ristanović, Z.; Orrit, M.; Deperasińska, I.; Kozankiewicz, B. *ChemPhysChem* **2019**, *20*, 55–61.
- (5) Orrit, M.; Bernard, J.; Zumbusch, A. *Chemical Physics Letters* **1992**, *196*, 6.
- (6) Fleury, L.; Zumbusch, A.; Orrit, M.; Brown, R.; Bernard, J. *Journal of Luminescence* **1993**, *56*, 15–28.
- (7) Plakhotnik, T. *ChemPhysChem* **2006**, *7*, 1699–1704.
- (8) Plakhotnik, T. *Journal of Luminescence* **2007**, *127*, 235–238.
- (9) Faez, S.; van der Molen, S. J.; Orrit, M. *Physical Review B* **2014**, *90*, 205405.
- (10) Rühl, M.; Lehmeier, J.; Nagy, R.; Weisser, M.; Bockstedte, M.; Krieger, M.; Weber, H. B. *New Journal of Physics* **2021**, *23*, 073002.
- (11) Bassett, L. C.; Heremans, F. J.; Yale, C. G.; Buckley, B. B.; Awschalom, D. D. *Physical Review Letters* **2011**, *107*, 266403.
- (12) Deperasińska, I.; Banasiewicz, M.; Gawryś, P.; Morawski, O.; Olas, J.; Kozankiewicz, B. *The Journal of Chemical Physics* **2021**, *155*, 034504.
- (13) Nicolet, A.; Kol'chenko, M. A.; Kozankiewicz, B.; Orrit, M. *The Journal of Chemical Physics* **2006**, *124*, 164711.
- (14) Navarro, P.; Tian, Y.; van Stee, M.; Orrit, M. *ChemPhysChem* **2014**, *15*, 3032–3039.
- (15) Kummer, S.; Basché, T.; Bräuchle, C. *Chemical Physics Letters* **1994**, *229*, 309–316.
- (16) Deperasińska, I.; Kozankiewicz, B. *Chemical Physics Letters* **2017**, *684*, 208–211.
- (17) Gorshelev, A. A.; Naumov, A. V.; Eremchev, I. Y.; Vainer, Y. G.; Kador, L.; Köhler, J. *ChemPhysChem* **2010**, *11*, 182–187.
- (18) Colautti, M.; Piccioli, F. S.; Ristanović, Z.; Lombardi, P.; Moradi, A.; Adhikari, S.; Deperasińska, I.; Kozankiewicz, B.; Orrit, M.; Toninelli, C. *ACS Nano* **2020**, *14*, 13584–13592.

- (19) Kummer, S.; Basche, T. *The Journal of Physical Chemistry* **1995**, *99*, 17078–17081.
- (20) Plakhotnik, T.; Moerner, W. E.; Palm, V.; Wild, U. P. *Optics Communications* **1995**, *114*, 83–88.
- (21) Verberk, R.; Orrit, M. *The Journal of Chemical Physics* **2003**, *119*, 2214–2222.
- (22) Basché, T.; Moerner, W. E. *Nature* **1992**, *355*, 335–337.
- (23) Kol'chenko, M. A. *Optics and Spectroscopy* **2005**, *98*, 681.
- (24) Keum, C.-M.; Liu, S.; Al-Shadeedi, A.; Kaphle, V.; Callens, M. K.; Han, L.; Neyts, K.; Zhao, H.; Gather, M. C.; Bunge, S. D.; Twieg, R. J.; Jakli, A.; Lüssem, B. *Scientific Reports* **2018**, *8*, 699.
- (25) Wolf, H. C. *Zeitschrift für Naturforschung A* **1958**, *13*, 414–419.
- (26) Nakada, I. *Journal of the Physical Society of Japan* **1962**, *17*, 113–118.
- (27) Lawetz, V.; Orlandi, G.; Siebrand, W. *The Journal of Chemical Physics* **1972**, *56*, 4058–4072.
- (28) Patterson, F. G.; Lee, H. W. H.; Wilson, W. L.; Fayer, M. D. *Chemical Physics* **1984**, *84*, 51–60.
- (29) Brouwer, A. C. J.; Groenen, E. J. J.; Schmidt, J. *Physical Review Letters* **1998**, *80*, 3944–3947.
- (30) Liu, X.; Su, X.; Livache, C.; Chamoiseau, L.-M.; Sanaur, S.; Sosa-Vargas, L.; Ribierre, J.-C.; Kreher, D.; Lhuillier, E.; Lacaze, E.; Mathevet, F. *Organic Electronics* **2020**, *78*, 105605.
- (31) Aubret, A.; Orrit, M.; Kulzer, F. *ChemPhysChem* **2019**, *20*, 345–355.
- (32) Nicolet, A. A. L.; Hofmann, C.; Kol'chenko, M. A.; Kozankiewicz, B.; Orrit, M. *ChemPhysChem* **2007**, *8*, 1215–1220.
- (33) Frisch, M. J.; Trucks, G. W.; Schlegel, H. B.; Scuseria, G. E.; Robb, M. A.; Cheeseman, J. R.; Scalmani, G.; Barone, V.; Petersson, G. A.; Nakatsuji, H.; Li, X.; Caricato, M.; Marenich, A. V.; Bloino, J.; Janesko, B. G.; Gomperts, R.; Mennucci, B.; Hratchian, H. P.; Ortiz, J. V.; Izmaylov, A. F.; Sonnenberg, J. L.; Williams, Ding, F.; Lipparini, F.; Egidi, F.; Goings, J.; Peng, B.; Petrone, A.; Henderson, T.; Ranasinghe, D.; Zakrzewski, V. G.; Gao, J.; Rega, N.; Zheng, G.; Liang, W.; Hada, M.; Ehara, M.; Toyota, K.; Fukuda, R.; Hasegawa, J.; Ishida, M.; Nakajima, T.; Honda, Y.; Kitao, O.; Nakai, H.; Vreven, T.; Throssell, K.; Montgomery Jr., J. A.; Peralta, J. E.; Ogliaro, F.; Bearpark, M. J.; Heyd, J. J.; Brothers, E. N.; Kudin, K. N.; Staroverov, V. N.; Keith, T. A.; Kobayashi, R.; Normand, J.; Raghavachari, K.; Rendell, A. P.; Burant, J. C.; Iyengar, S. S.; Tomasi, J.; Cossi, M.; Millam, J. M.; Klene, M.; Adamo, C.; Cammi, R.; Ochterski, J. W.; Martin, R. L.; Morokuma, K.; Farkas, O.; Foresman, J. B.; Fox, D. J. *Gaussian 16 Rev. C.01*, Wallingford, CT, 2016.
- (34) Neese, F. *WIREs Computational Molecular Science* **2018**, *8*, e1327.
- (35) Nicolet, A. A. L.; Kol'chenko, M. A.; Hofmann, C.; Kozankiewicz, B.; Orrit, M. *Physical Chemistry Chemical Physics* **2013**, *15*, 4415–4421.

5

HEXAGONAL BORON NITRIDE: A UNIVERSAL HOST MATRIX?

In this chapter, I will present the studies that we performed on an unconventional host for single molecules, namely two-dimensional hexagonal boron nitride (hBN). We will show that single molecules on the surface of hBN reveal narrow spectral lines at low temperature. Contrary to molecules on surfaces of three-dimensional (organic) crystals, we were able to record excitation spectra of the molecule's zero-phonon lines on the surface of hBN and reveal linewidths that are sometimes less than a factor 10 broader than the lifetime-limited linewidth, as dictated by the fluorescence lifetime. This new host could potentially overcome the limitations of three-dimensional organic matrices, which require a 'good' insertion of the guest molecules. However, molecules on hBN are subject to a spectral diffusion and this currently limits the usability of this system for applications such as sensing at the nanoscale or uses in quantum optics. We will show that thermal annealing of the hBN, before deposition of the molecules, dramatically improves the stability of the molecules and this indicates it might be possible to eliminate spectral diffusion altogether. In this study, we will focus on terrylene molecules adsorbed onto hBN. In addition, we will show some results of new types of molecules, called graphene quantum dots, which have not been studied before in line-narrowing spectroscopy. Due to their bulkiness, these type of molecules are difficult to incorporate in standard host matrices and therefore these studies underline the potential to extend the use of hBN to a large variety of guest molecules.

Part of the contents of this chapter is published as: R. Smit, A. Tebyani, J. Hameury, S.J. van der Molen and M. Orrit, "Sharp zero-phonon lines of single organic molecules on a hexagonal boron-nitride surface", Nature Communications 14, 7960 (2023)

5.1. INTRODUCTION

5.1.1. HEXAGONAL BORON NITRIDE

Similar to graphene, hexagonal boron-nitride (hBN) is a two-dimensional material that possesses a hexagonal lattice (Figure 5.1). However, unlike graphene, the alternating arrangement of boron and nitrogen opens up a large electronic band gap of about 6 eV,¹ which makes it optically transparent. hBN is therefore usually termed ‘white graphene’. Importantly, the large band gap of hBN avoids what would happen with fluorescent molecules in contact with graphene or other small bandgap materials, namely fluorescence quenching by non-radiative energy transfer.² The similar structure, bond lengths and the van der Waals interactions that exist in multilayer hBN, make hBN an interesting host material for polycyclic aromatic hydrocarbons, which are interacting through van der Waals forces among each other as well. Fluorescent terrylene molecules, deposited on hBN, were already measured at room temperature by Han *et al.*³ Interestingly, this work suggests that the terrylene molecules are protected by the hBN, as bleaching rates of single molecules were more than a hundred-fold reduced on hBN, as compared to single molecules on bare silica.

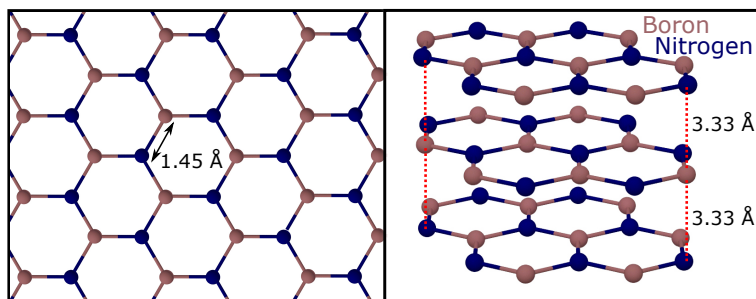


Figure 5.1.: Structure of hexagonal boron-nitride. Boron and nitrogen are alternatingly arranged, with an interatomic distance of 1.45 Å. In multilayer hBN, the layers stack such that a nitrogen atom faces a boron atom and vice versa. The interlayer distance is 3.33 Å, which is the same as for graphene.⁴

As a model molecule for our studies of hBN, we also employed terrylene. No further introduction of this molecule is required, as it is already part of an extensive study in Chapter 4. hBN can be synthesized in several forms, such as free-standing crystals or grown onto a substrate. On a substrate, such as Cu(111), wafer-scale monolayers of hBN can be grown by chemical vapor deposition.⁵ Free-standing crystals of hBN are traditionally grown by chemical reactions at high temperature and high pressure.⁶ This is also the method used by T. Taniguchi and K. Watanabe from NIMS,⁷ whose hBN crystals are regarded to be of the best quality. Since the first discovery of single-photon emitters in hBN,⁸ a new and nowadays rich field of research has emerged. Since then, many types of distinct emitters in hBN, typically attributed to light-emitting defects, have been reported. The fluorescence from these emitters peaks over a surprisingly broad spectral range, from the deep ultraviolet⁹ up to the near-infrared,¹⁰ with many more at

in-between wavelengths. The atomic and electronic structure of the claimed defects still remains a puzzle and only educated guesses as to their origin have been made from quantum-chemistry models.^{11–14} Since the start of our work, new perspectives on some of these emitters have arisen, such as that some of their origins could be traced back to organic compounds formed during preparation steps that involves high-temperature thermal annealing.¹⁵

5.1.2. LOW-TEMPERATURE SPECTROSCOPY ON SURFACES

At room temperature, the surface of a substrate is commonly used to study single molecules. At low temperature, on the contrary, surfaces are not a stable environment compared to the bulk of a solid. Early studies of single molecules in a hexadecane crystal revealed that molecules closer to the interface with silica had strongly broadened zero-phonon lines, while no zero-phonon line was detected for single molecules at the silica surface itself.¹⁶ Later experiments on dibenzanthanthrene (DBATT) inside nanochannels filled with matrices of naphthalene and n-tetradecane confirmed that molecular spectral lines were broader when the channel decreased in height and molecules would be located closer to the interfaces.¹⁷ Lastly, the study of fluorescent molecules evaporated onto a polymer layer, controllably heated to allow the molecules to diffuse into the polymer and settle at controllable mean depths, showed likewise that molecules closer to the surface exhibited strongly broadened zero-phonon lines. Interestingly, the amount of spectral diffusion was also significantly higher for molecules closer to the surface and no zero-phonon line could be detected closer than 0.5 nm to the surface.¹⁸ Beyond single-molecule studies, narrow ZPLs down to 500 MHz in width have been observed through hole-burning spectroscopy, e.g. for chemisorbed, and thus strongly bound, quinizarin on alumina surfaces,¹⁹ but this particular method relies on weak photostability and thus renders it impossible to detect single molecules.

The causes for the anomalous behavior of ZPLs of single molecules close to a surface or interface as compared to molecules in the bulk is still under debate. Possibly, high densities of two-level systems (TLSs) at or close to the surface have lower activation energies due to the ill-condensed boundaries of a crystal. Impurities could also pile up at the crystal boundaries due to expulsion from the bulk or by adsorption from the environment and give rise to a local increase of conformational states. Despite these surface-induced effects on ZPLs, it has been possible to reduce the dimensions of host-guest crystals and yet obtain near-lifetime-limited emission in the bulk of aromatic nanocrystals less than 100 nm thick, grown by reprecipitation from solution.^{20,21} Thinner matrices for single molecules are highly desirable for applications such as single-charge sensing, which requires a close proximity of the sensing molecules to the charge,²² or potential applications in nanophotonics. For the latter case, such systems-on-a-chip make use of dielectric waveguides, and a closer proximity of single molecules to waveguides is expected to lead to a better coupling to the evanescent field. The coupling of single molecules to waveguides on a chip was demonstrated in 2017.²³ Later experiments with waveguide-coupled single dibenzoterrylene (DBT) molecules revealed spectral diffusion of the 0-0 ZPL under an applied electric field, attributed to charge fluctuations induced within the nanoguide itself.²⁴ With high-quality anthracene crystals of about 150 nm

in thickness, suspended over the waveguide channels, it was demonstrated that DBT molecules coupling to the waveguide remain stable and near-lifetime-limited for hours.²⁵

5.2. EXPERIMENTAL

5.2.1. SAMPLE PREPARATION

In most experiments, we made use of free-standing crystals, purchased from the company HQ Graphene. In the remaining experiments (to be mentioned in the text) we employed high-quality crystals from NIMS, with permission shared with us by dr. Semonti Bhattacharyya from Leiden University. The crystals of both sources are typically up to a few mm large and multilayered. To obtain flakes of hBN on a substrate we use the commonly-employed method of exfoliation using scotch tape, which was established by A. Geim and K. Novoselov to obtain graphene monolayers.²⁶ The repeated use of the scotch tape cleaves the thick crystals into thinner (and smaller) crystals, which can be transferred to a substrate. The tape is stuck to the substrate and heated to 120 °C for 2 minutes on a hot plate to improve the adhesion of the flakes to the substrate. Then the tape is removed, while some flakes stay behind (Figure 5.2). As a typical substrate we used a Si wafer with a thermally-grown oxide layer of 300 nm, bought from University Wafer. Before deposition of hBN, the substrate was typically cleaned with acetone.

Molecules were either diluted in toluene (Acros Organics, 99.85 %) and spin-coated on the substrates or directly sublimated from crystals. For the preparation by spin coating, the concentration of molecules in toluene was diluted to 0.1-1 nM and about 30-50 μL of the solution was pipetted on the substrate and spin coated for 20 s at 2000 rpm, followed by a drying step at 4000 rpm for another 20 s. For sublimation, pure crystals of terylene were placed at the bottom of a vacuum sublimation apparatus, where the substrate was suspended on a cold finger, cooled by water ice (Figure 5.3). The atmosphere was pumped to vacuum and the bottom was heated to 120-140 °C, in order to obtain a similar concentration as obtained through spin coating.

For the fluorescence measurements we used the setup as described in Chapter 2 in Figure 2.3. In the early experiments, the flakes were used immediately, but later we performed post-processing on the flakes, such as thermal annealing. Thermal annealing was performed in a Thermcraft tube oven in a moderate vacuum of about 10^{-2} mbar of residual air. The annealing temperatures were varied between 500–900 °C with a dwell time of up to 12 hours. Height profiles of the hBN flakes were measured by AFM.

5.3. RESULTS AND DISCUSSION

5.3.1. PROPERTIES OF THE HBN FLAKES

Atomic force microscopy (AFM) measurements show that most of the hBN flakes have a thickness of less than 100 nm (about 300 layers), with some exceptions of thick flakes of a few 100 nm. The AFM scans in Figure 5.4 show flakes that were either annealed or not annealed. On the flakes themselves, there is no noticeable difference in the AFM scans between Figure 5.4e and Figure 5.4f, which is measured before and after annealing. In the regions outside of the flakes, the residue from the scotch tape (mostly

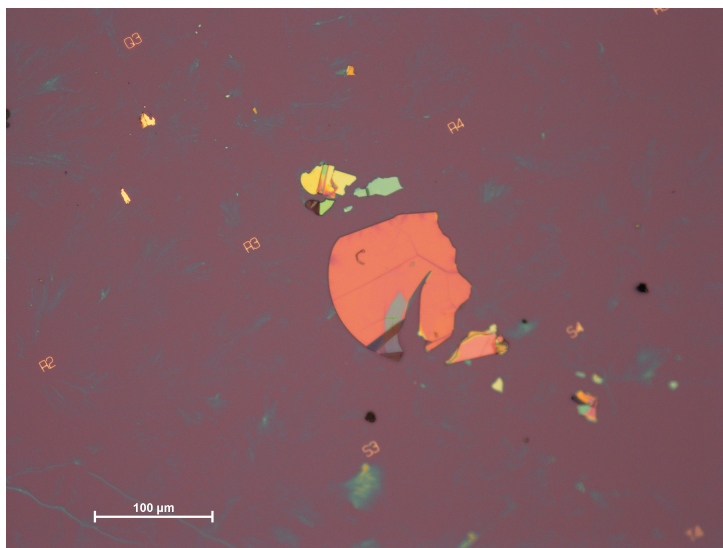


Figure 5.2.: . Microscope image of a collection of hBN flakes that are obtained by exfoliation. The sizes of the flakes vary from sub- μm to large flakes of up to a few $100\ \mu\text{m}$. The color of the flakes gives a rough indication of the thickness, as it arises from interference of light reflected from the interfaces.²⁷ Typically, the bluish flakes are the thinnest, while reddish flakes are the thickest. The blue-green-yellowish clouds in the background are polymer residues from the scotch tape.

polymers) is removed efficiently by thermal annealing. However, the surface roughness on the flakes themselves is preserved, as the contamination could be located under the flake and is therefore protected.

As part of surface roughness, there are sometimes bubbles present in the AFM scans (see for example one in the left corner of Figure 5.4e). These bubbles or pockets are likely due to pile-up of organic contamination between the hBN sheets or at the interface, and were similarly observed in heterostructures of 2D materials by cross-sectional imaging.²⁸ Step edges, due to a decrease or increase in layer count, also occur in the scans, but are sometimes difficult to see, because of their low contrast. Such step edges are better visualized on extended terraces, present as sharp lines in Figure 5.5. Other anomalies are the sharp increases in height, such as found in Figure 5.4d. These are likely caused by wrinkles in the sheet, where the layers fold up. The formation of wrinkles was found to be enhanced by annealing at similar temperatures as we used.²⁹ On the extended terraces, the surface can be almost atomically flat as shown in Figure 5.5, where the surface height deviations reach $0.41\ \text{nm}$, close to the interlayer distance of $0.33\ \text{nm}$. Although this could indicate a small variation in layer count, the measured values are likely limited by the AFM resolution and the surface roughness of the wafer substrate.

The lattice of hBN has only one weakly active Raman mode around $1,365\ \text{cm}^{-1}$,

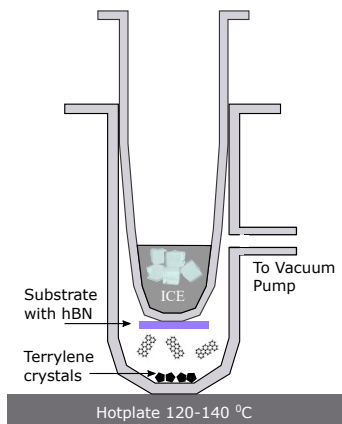


Figure 5.3.: Schematic representation of the sublimation apparatus, which consists of two round-bottom flasks, where the top one is inserted into the bottom one, sealed by vacuum grease (Apiezon) and pumped by a vacuum pump from the side. The bottom of the flask is heated on a hot plate to approximately 120-140 °C. The crystals are placed inside, in contact with the heated bottom. The sample is fixed with carbon tape on the cold finger and cooled by water ice.

5

attributed to the stretching of the bond between boron and nitrogen. We observed this Raman peak with a relatively strong 532 nm laser spot, shown in Figure 5.6. The width of the Raman peak of about 10 cm^{-1} depends not only on crystal quality, but also on the isotopic distribution. In high-quality crystals grown with natural abundances of isotopes, ^{14}N and ^{15}N for nitrogen and ^{10}B and ^{11}B for boron, the Raman peak has a minimum width of about $7.3\text{-}7.5 \text{ cm}^{-1}$.³⁰ Hence, the $10 \pm 1 \text{ cm}^{-1}$ measured in our samples may be the result of a poorer crystallinity, although the measured linewidth conforms to the report of HQ Graphene. For the hBN from NIMS, regarded to be of higher quality, the Raman peak measured the same width within the uncertainty.

5.3.2. ROOM-TEMPERATURE FLUORESCENCE MEASUREMENTS

After deposition of molecules on the hBN substrate, we measured the spatial distribution of the emitters and their spectra at room temperature. In the case of sublimated molecules on non-annealed hBN flakes, we find molecules to be located everywhere on the hBN flake (see Figure 5.7a). However, some regions tend to be more packed with molecules than others are. For example, the sharp edge in Figure 5.7a, possibly a step edge or wrinkle, contains a lot more fluorophores than the stretched and presumably flat regions. Interestingly, this packing of emitters was similarly observed for defect emitters, which are in exfoliated hBN also preferentially located around sharp edges.^{31,32} However, both reports concern emitters that were activated by

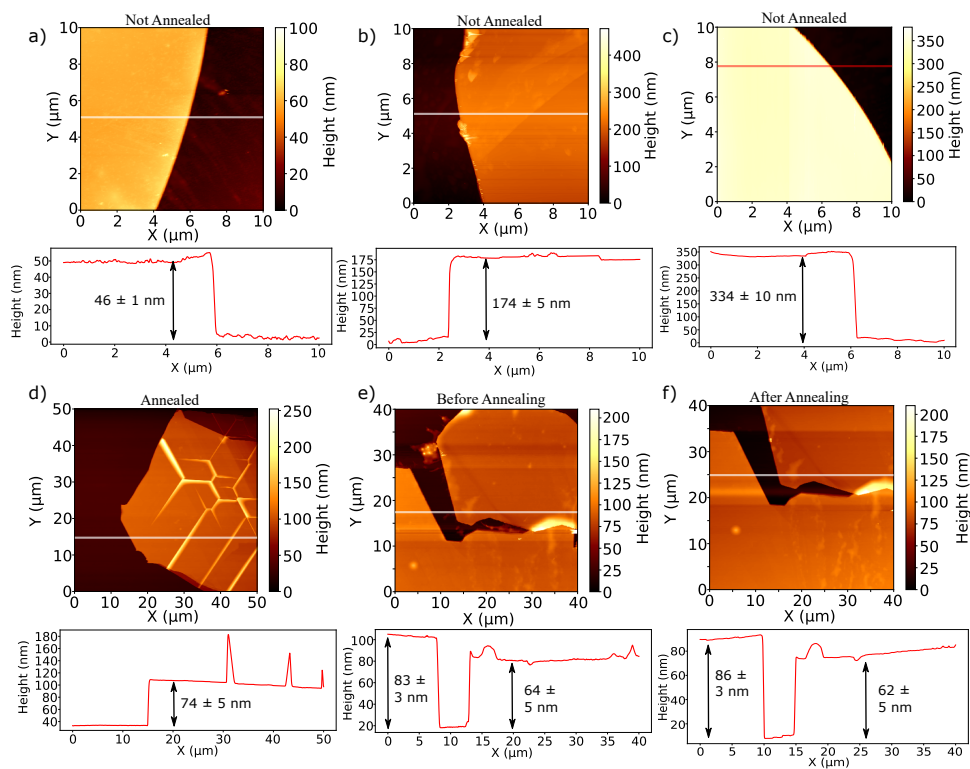


Figure 5.4.: a,b,c) AFM scans of a small part ($10 \times 10 \mu\text{m}^2$) of non-annealed exfoliated hBN flakes on a Si/SiO₂ substrate with below each 2D map the corresponding height profile, recorded along the white line (red for (c)). The flake in (d) is annealed at 500 °C for 12 hours. The AFM images in (e) and (f) show the same flake, respectively before and after annealing at 500 °C for 12 hours.

thermal annealing, which as mentioned before could create organic molecule emitters.¹⁵ Furthermore, our molecules have found some place to immobilize, as was already observed by Han *et al.*, and can be measured up to a few minutes of time until bleaching occurs. In samples with a very high concentration of terrylene, the bleaching is clearly observed as a single exponential decay in the measured fluorescence signal, where the time constant is typically in the order of minutes (Figure 5.7b). This bleaching rate is relatively fast and may indicate that most (sublimated) molecules are not so well protected by the hBN, as suggested for the spin-coated molecules by Han *et al.* For spin-coated molecules it might be possible that some molecules diffuse from the solvent between the interface of silica and hBN.³³

The room-temperature spectra of the fluorescence emission from the isolated spots

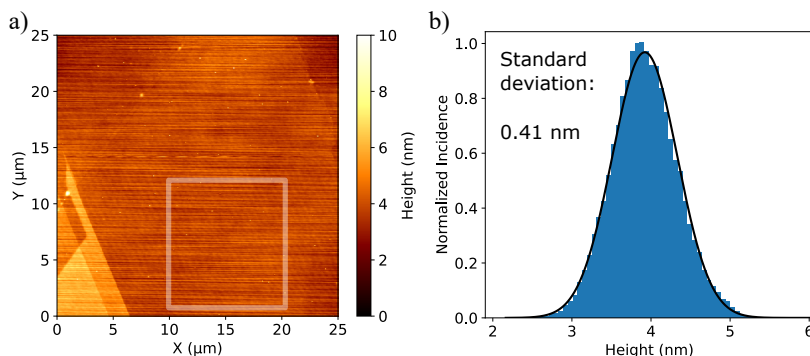


Figure 5.5.: AFM scan of a flat area of an annealed hBN flake (500 °C for 12 hours). The white rectangle encloses the region that builds up the histogram in b). The Gaussian distribution of surface heights shows a standard deviation of 0.41 nm. Tilts and drifts in the scan have been subtracted by a line-by-line linear fit.

5

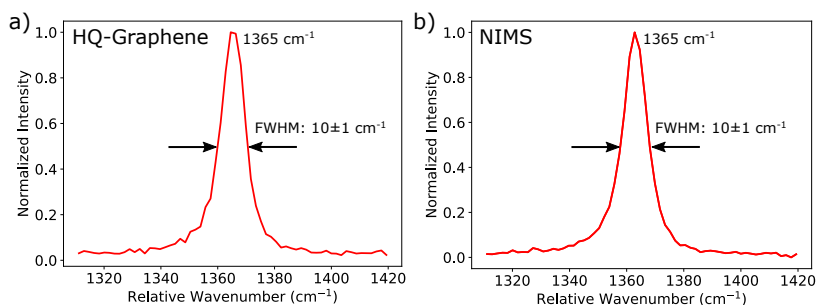


Figure 5.6.: Spectra of the inelastically-scattered light from a multilayer hBN flake (from supplier HQ Graphene in panel (a) and NIMS in panel (b)), taken with a 532 nm laser. The single Raman peak observed for both cases at 1365 cm^{-1} , with a FWHM of $10 \pm 1 \text{ cm}^{-1}$, was taken at a resolution of around 1-2 cm^{-1} . The spectrum is recorded at room temperature with a 1200 lines/mm grating and a 0.1 mm slit size.

displays a shape that conforms to the emission spectrum of terylene, but also of many other polycyclic aromatic hydrocarbons (PAHs). The spectra are heavily broadened at room temperature and few features can be resolved, apart from the large spectral bands around the 0-0 zero-phonon line, the C-C stretch region and overtones (Figure 5.8a). All of them are also present for other PAHs. However, for some isolated emitters, the spectra did reveal more features, such as in Figure 5.8b. The positions of these bands coincide with the well-resolved spectral lines that we recorded at low temperature, which will be shown in the next section.

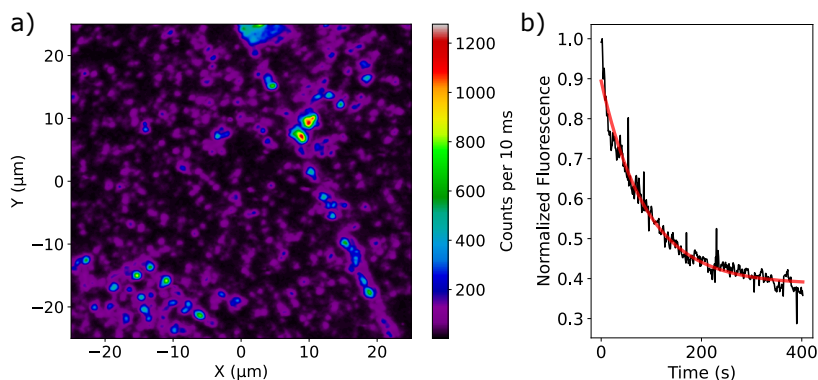


Figure 5.7.: Panel (a) shows a fluorescence map of a part of an hBN flake. The terrylene molecules are sublimated, using the setup in Figure 3, at 120 °C for 5 minutes and excited by a vibronic transition with 532 nm light. The faintest and most isolated spots of purplish color are possibly single molecules (antibunching measurements were only made at low temperature, in absence of photobleaching), while brighter spots are likely multiple molecules in the same focal area. The image was recorded at an excitation intensity of about 10 kW/cm². At similar power levels, and high concentration of terrylene, bleaching occurs at room temperature, at timescales in the order of minutes, as shown in panel (b). The characteristic time of the single exponential decay is here around 90 s. The data is measured from the integrated intensity of emission spectra. Deviations due to cosmic rays in the spectra, which are not filtered, are probably the cause of the peaks. Note that the bleaching does not extend to zero and may be caused by some population of molecules that bleach on a much longer timescale and/or contributions from molecules further away from the peak of the diffraction-limited laser spot.

Surprisingly, a major discrepancy exists between the spectra in Figure 5.8 and the results of Han *et al.* The emission intensity peaks around 580 nm, while Han *et al.* reported an emission peak around 600 nm. This is a significant red-shift of the emission peak, which is not regularly observed for terrylene in organic matrices. Only for terrylene in *p*-dichlorobenzene,³⁴ with a site around 597 nm, and terrylene in BTBT at 602 nm (see Figure 4.1 in Chapter 4), the emission is shifted that far to the red. Although the majority of terrylene molecules do display an emission around 580 nm in our work, we will show that after annealing of the hBN flakes, a population of molecules around 600 nm does appear in the inhomogeneous broadening.

5.3.3. LOW-TEMPERATURE SPECTRA OF TERYLENE ON HBN

By cooling down our hBN samples covered with terrylene, we observe a strong line narrowing of the emission spectra. This allows us to identify each emitter located on

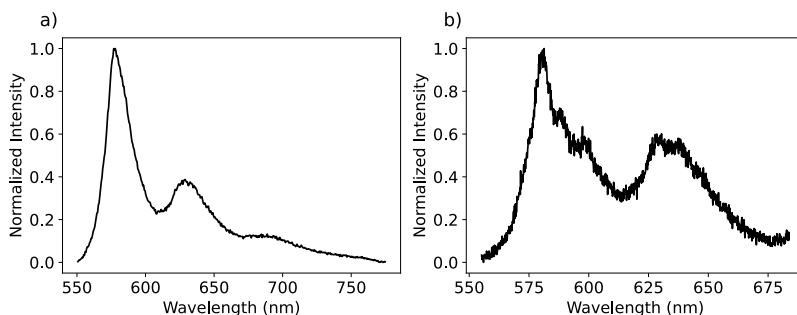


Figure 5.8.: Fluorescence emission spectra of terrylene at room temperature. The spectrum in (a) is likely from an ensemble of terrylene molecules, while the spectrum in (b) might be from a single molecule, as the emission was relatively isolated.

5

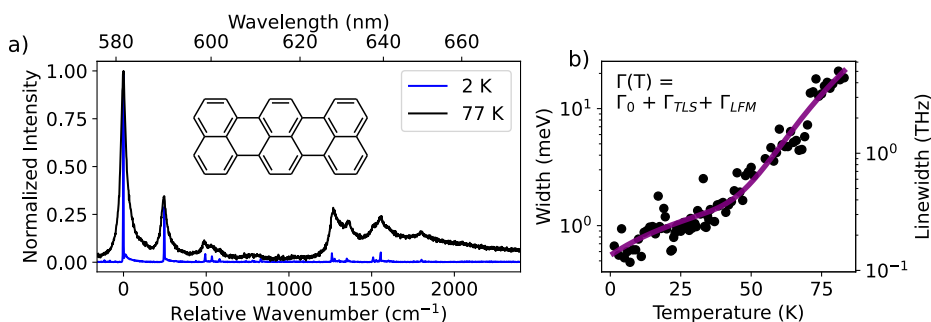


Figure 5.9.: Emission spectra of a single terrylene molecule around 582 nm, taken at two temperatures, 2 K (blue) and 77 K (black). Both spectra have been normalized to unity relative to the intensity of the 0-0 ZPL. b) Linewidth of the 0-0 ZPL of a single terrylene molecule (not the one shown in (a)). The linewidth was fitted to the equation in inset, where Γ_{TLS} scales linearly with temperature and Γ_{LFM} is given by the Arrhenius law, described in equation 5.1. The linewidth at the lowest temperature was limited by the spectrometer resolution ($1.7 \pm 0.1 \text{ cm}^{-1}$). A zoomed-in version of the spectrum in (a) can be found in Figure 5.11b.

the hBN flake by its vibrational fingerprint. The blue curve in Figure 5.9a shows sharp spectral lines, limited in width by the spectrometer resolution of about $1.7 \pm 0.1 \text{ cm}^{-1}$. Even at liquid-nitrogen temperatures of 77 K, the coarse spectral fingerprint of the emitter could be resolved with relative ease, which makes the use of liquid helium not necessary for identification of the emitters. The sharpest line in the spectrum is the 0-0 ZPL and corresponds to the purely electronic transition. The remaining peaks correspond

to a transition that involves an additional excitation of a (or multiple) vibration(s). These vibrational energies have been analyzed for terylene in great detail in various matrices³⁵⁻³⁷ and can also be found in the spectrum of terylene in BTBT, Figure 4.1 in chapter 4. The line narrowing of the 0-0 ZPL follows the relationship with temperature shown in Figure 5.9b. Here, we measured the linewidth or full-width-at-half-maximum for 88 intermediate temperatures over the range of 1.4 K up to 83 K. The 0-0 ZPL linewidth follows the broadening relation that is consistent with defects in hBN^{38,39} or disordered matrices, such as polymers:⁴⁰

$$\Gamma(T) = \Gamma_0 + \Gamma_{TLS} + \Gamma_{LFM} = \Gamma_0 + bT^\alpha + w \times \exp(-E_a/k_B T). \quad (5.1)$$

The first term Γ_0 is the homogeneous linewidth, while the broadening terms Γ_{TLS} and Γ_{LFM} account for respectively the activation of switching two-level systems (TLSs) and the population of quasi-localized low-frequency modes (LFMs). In general, two-level systems are activated in a linear fashion with temperature, with $\alpha \approx 1$. The LFMs are activated by an Arrhenius law and provide an activation energy or Debye temperature of the molecule in its insertion site. Comparing the broadening of terylene on hBN to traditional three-dimensional matrices we find in the limited amount of works available that the linewidth at 50 K of about 25 cm^{-1} is very similar to the linewidth of terylene found in the Shpol'skii matrices n-hexadecane and n-dodecane,⁴¹ with respectively $33 \pm 3 \text{ cm}^{-1}$ and $21 \pm 3 \text{ cm}^{-1}$. However, the contribution from TLSs, which we estimate as $5 \pm 3.5 \text{ GHz/K}$ ($21 \pm 14 \text{ } \mu\text{eV/K}$) seems to be considerably larger than the typically less than 100 MHz/K found in Shpol'skii matrices.⁴⁰ The similar linewidth of terylene on hBN compared to a Shpol'skii matrix and the higher TLS broadening on hBN could mean that molecules in Shpol'skii systems broaden quicker at lower temperatures. As we will show later, the TLSs are likely attributed to organic contamination on the surface of hBN and thus the closer proximity of these TLSs might be responsible for the stronger broadening. Beyond this linear regime of TLSs, there is a clear exponential take-off from about 50 K, which corresponds to a rather high activation energy or Debye temperature of $405 \pm 41 \text{ K}$. This is considerably higher than the regular 10-40 K observed for example in the case of dibenzoterylene (DBT) in anthracene⁴²⁻⁴⁴ and found in all organic matrices. However, DBT molecules in anthracene broaden with a pure Arrhenius curve and do not suffer from additional broadening of the homogeneous linewidth due to TLSs.

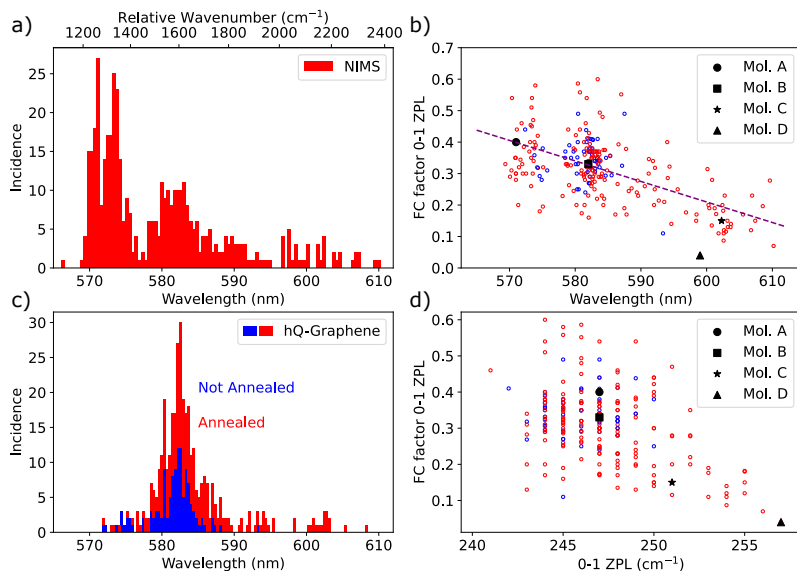


Figure 5.10.: Panel (a) displays the histogram of wavelengths where we found the purely-electronic transition of single terrylene molecules on hBN flakes from NIMS. All data was recorded with a fixed 532 nm excitation laser and for reference the relative difference in energy between this laser and the 0-0 ZPL of the molecules is shown on the top axis in wavenumbers. Note that some structure is present in the histogram, which might arise from absorption peaks that reflect the vibrational spectra in Figure 5.11 of terrylene. Hence, some molecules may not appear in the histogram, because there are no absorption lines present at 532 nm. This suggests that there might be a continuous distribution, spanning a large range of more than 40 nm. All data of 452 individual molecules is obtained from annealed hBN. Panel (b) shows for 237 molecules (58 molecules for non-annealed hBN in blue color), both from hBN from NIMS and HQ Graphene, the relation between the relative intensity of the main vibration (0-1 ZPL) versus the position of the 0-0 ZPL. On average, the more red-shifted molecules have a weaker vibronic coupling (Pearson's correlation coefficient $r = -0.56$). In panel (c) a similar distribution is shown as for (a), but for hBN from the supplier HQ Graphene and taken from both annealed (red data) and non-annealed (blue) hBN. The total number of molecules in the histogram amounts to 373 (123 for non-annealed and 250 for annealed hBN). Panel (d) shows the relation between the energy of the 0-1 ZPL and the relative intensity of the 0-1 ZPL compared to the 0-0 ZPL. Overall, a decrease in the Franck-Condon (FC) factor of the 0-1 ZPL is measured when the energy of the 0-1 ZPL is higher. The symbols displayed in panel (b) and panel (d) refer to the molecules that are plotted in Figure 5.11.

We find the 0-0 ZPLs of terrylene molecules to be scattered over a broad range, though with clustering around specific wavelengths (see Figure 5.10a and 5.10c). We started initial experiments with hBN obtained from HQ Graphene and the inhomogeneous broadening of terrylene on flakes of that particular manufacturer centers mostly around 582 nm. This distribution, found in Figure 5.10c, is relatively broad with a width of about 4 nm (120 cm^{-1}), which is compared to other hosts only typical for disordered systems such as polyethylene.⁴⁵ For the case of hBN obtained from NIMS, we measure a very different distribution of 0-0 ZPLs, which rather looks like a signature of a larger continuous distribution, spanning over 40 nm. This continuous distribution displays gaps and a structure that reminds of the vibrational spectrum of terrylene, where the structure is given by the energy difference between the 532 nm laser and the 0-0 ZPL position; a narrow absorption spectrum. This could indicate that we are not seeing all molecules with our fixed-frequency laser, as those molecules could simply lack absorption lines in resonance with the laser. Surprisingly, the inhomogeneous broadening of terrylene on NIMS hBN peaks around 572 nm instead of 582 nm. This marked difference still remains to be explained.

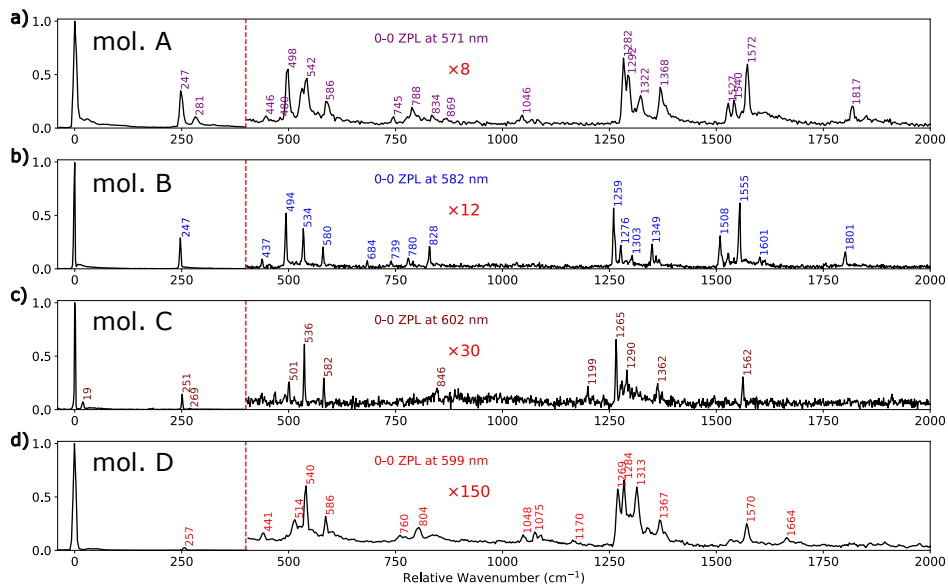


Figure 5.11.: Comparison of fluorescence emission spectra of single terrylene molecules at various positions in the inhomogeneous broadening. The spectrum in panel (a) is from a molecule with a 0-0 ZPL at 571 nm, taken on annealed hBN from NIMS. Panel (b) shows the detailed spectrum of the molecule in Figure 5.9a (blue curve), with a 0-0 ZPL at 582 nm and taken on HQ Graphene hBN (not annealed). Panel (c) shows a red-shifted molecule (602 nm) taken on HQ Graphene hBN that was annealed. Another red-shifted molecule at 599 nm is shown in panel (d), taken on annealed NIMS hBN. Note that the red-shifted molecules have weaker Franck-Condon factors, where in the extreme case of molecule D, the part of the spectrum after 400 cm^{-1} is magnified by 150x for comparison. Moreover, the phonon sidebands are weaker for the red-shifted molecules. In the case of (d), the Debye-Waller factor ($=I_{ZPL}/(I_{ZPL} + I_{PSB})$) is more than 0.9. The spectra in (a) and (d) were taken with a slightly lower resolution of 600 lines/mm at a 0.1 mm slit size of the spectrometer in order to capture the whole spectrum at once. The spectra in (b) and (c) were taken with the higher resolution grating of 1200 lines/mm and 0.1 mm slit size and are therefore stitched by two individual recordings.

On hBN flakes that were annealed prior to molecule deposition, as compared to non-annealed flakes, we find molecules with considerably red-shifted 0-0 ZPLs. Surprisingly, the red-shifted molecules show a reduced vibronic coupling (Franck-Condon factors) between the excited state and vibronic levels of the ground state. Overall, we observe a decrease of the Franck-Condon (FC) factors when the 0-0 ZPL shifts to the red, as observed in Figure 5.10b, where examples of emission spectra in various positions

along the inhomogeneous broadening are additionally shown in Figure 5.11. Moreover, there appears to be a weak relation between the 0-0 ZPL position and the energy of the main vibration (frequency difference between the 0-1 ZPL and the 0-0 ZPL), shown in Figure 5.10c. In extreme cases, the FC factors show a suppression to such an extent that the bulk of emission is directed into the 0-0 ZPL. This can be expressed in a quantity that is called the branching ratio ($= I_{ZPL}/I_{spectrum}$) and amounts to the molecule in Figure 5.11d to at least 78%. This feature is particularly interesting for the generation of indistinguishable photons in quantum optics. In view of this application, the highest branching ratios have been achieved for dibenzoterrylene, where record values of up to 55% are reported for dibenzoterrylene in *p*-terphenyl nanocrystals.²¹ The cases of anomalously high branching ratios for terrylene were only detected on annealed hBN. In fact, in our experiments not a single molecule with a 0-0 ZPL beyond 600 nm was detected without prior annealing of the hBN flakes. Annealing, at the temperatures we applied (500 °C up to 900 °C) is expected to remove most organic contamination⁴⁶ and to at most redistribute defects such as vacancies,⁴⁷ as the removal of structural defects would require much higher temperatures, up to 1700 °C.⁴⁸

Remarkably, we also find considerably fewer molecules on the annealed samples, although we kept the sublimation rate of terrylene fixed or even slightly increased it. This is for example visible in the fluorescence image of an annealed flake in Figure 5.12. Compared to Figure 5.7a, there are significantly less emitters present on the flake. Moreover, the emitters that are there are mostly concentrated in the regions where the AFM scan shows an increased surface roughness. We propose as a possible explanation that terrylene anchors to (organic) contamination at the hBN surface. As annealing dramatically reduces the concentration of those anchors, terrylene molecules will either leave the flake area or may aggregate to the few nucleation sites and stop fluorescing because of self-quenching. Another possibility is that the annealing process creates dangling bonds at defect sites, which may react with terrylene upon sublimation and bleach them as a result. Interestingly, we find that the number of terrylene molecules on the flake increases again if prior to molecule sublimation, the annealed samples are intentionally contaminated by the spin-coating of n-hexadecane, which is known to form monolayers on top of hBN.⁴⁹ On the one hand, contamination could help terrylene to find more anchors and favor immobilization. On the other hand, contamination present before annealing could prevent terrylene from finding a site where it can interact strongly with the hBN, for example with some defect in the top hBN layer. We speculate that these hBN defects might be responsible for the red-shifted molecules. They would be accessible only after annealing of the hBN, right before the terrylene molecules are sublimated. However, binding to specific defects cannot explain the large inhomogeneous broadening on its own. In section 5.6, we propose that (local) strain, which could also affect atomic distances for defects, could be a possible explanation for the large inhomogeneous broadening when the molecule conforms to the strained hBN. This could point to a strong interaction with hBN, possibly in the form of chemisorption. For further studies, the need for special anchoring points could possibly be avoided by in-situ evaporation of terrylene on cold hBN surfaces, preferably performed in high vacuum and in-situ annealing of the surface. However, none of these steps are possible

in our setup. The nature of the defects that provide anchoring for terrylene could be also studied by intentionally creating defects in the lattice to see whether the concentration of the red-shifted molecules increases. However, the available methods to create defects also tend to create a lot of active emitters, and not only in the upper layer, such as observed with ion beams,⁵⁰ oxygen plasma⁵¹ or with electron beams.³¹

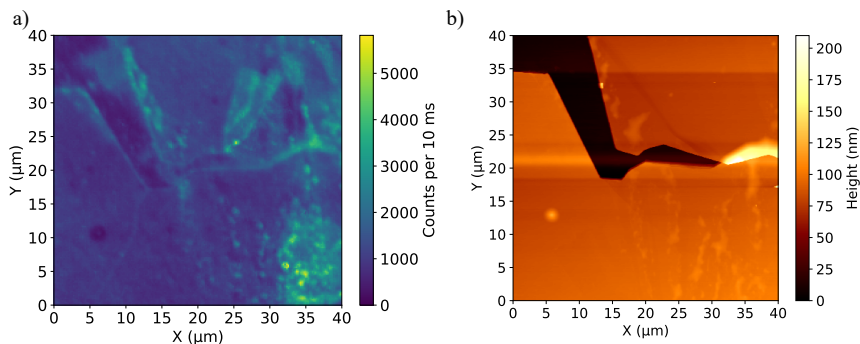


Figure 5.12.: (a) Fluorescence image and (b) AFM image corresponding to same area of a hBN flake that was annealed at 500 °C for 12 hours. The region in (a) for $25 < X < 30 \mu\text{m}$ and $23 < Y < 35 \mu\text{m}$ appears to have changed with respect to the same region in b), perhaps due to a folding of a part of the flake by the AFM tip.

5.3.4. SPECTRAL DIFFUSION

Part from changes in the inhomogeneous distribution, we also find that annealing of the hBN flakes, prior to deposition of molecules, improves the spectral stability of the single emitters, reducing the number of (tunneling) two-level systems (TLSs). This observation is consistent with our hypothesis that these TLSs may have been located in the organic contaminants. The improvement of the spectral stability is most clear when we used an annealing temperature of 500 °C up to 750 °C, but much less clear for higher temperatures of up to 900 °C. An evident case of coupling of a molecule to a single TLS is shown in Figure 5.13a, which traces the 0-0 ZPL position over time at gradually-increased excitation intensities. In Figure 5.13b, the number of spectral jumps observed in a time window of 200 s is related to the power density of the laser spot at the position of the molecule and follows the same relation as the fluorescence intensity of the 0-0 ZPL. Therefore, these spectral jumps are laser-induced in one-photon processes. Later, we will show that the spectral jumps are also observed by resonant excitation, which requires power densities of at least two orders of magnitude weaker, due to the narrow width of the 0-0 ZPL with respect to the width of a vibronic transition.

In some experiments, we noticed that the spectral diffusion also depends on the location of the molecule. Figure 5.14 shows an example of the observed spectral diffusion of 0-0 ZPLs of single molecules with corresponding locations on the hBN

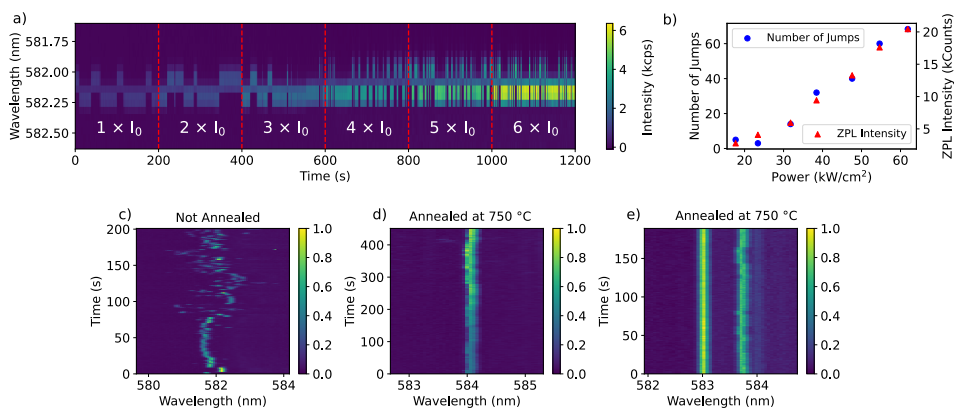


Figure 5.13.: A 0-0 zero-phonon line (ZPL) of a terrylene molecule in the main site followed for 20 minutes on an hBN flake that was annealed at 750 °C for 12 hours, excited by a vibronic transition with 532 nm light. The excitation intensity is raised after each frame of 200 s. The associated power densities, relative to the initial intensity I_0 , are shown in (b), together with the number of spectral jumps that are observed in the 200 s time window and the integrated intensity of the 0-0 ZPL for a period of 1 s. Without annealing, the spectral time trace typically exhibits complex spectral diffusion as shown for example in (c). In this case, the molecule initially wanders around a relatively narrow spectral region, but extends over a much wider region from about 70 s. After annealing, the amplitude of spectral diffusion is typically strongly reduced, as in (d), even though the laser power is doubled at each 100 s interval. Some molecules do not show any spectral diffusion on the scale resolved by the spectrometer, as is the case for the leftmost molecule in (e). The spectra in (c) are measured on a different sample than the spectra in (d) and (e).

flake, depicted in the middle. The two left series of spectra were recorded around an outer edge and inner edge, possibly a step edge, and show apart from a higher concentration of emitters, an increased rate of spectral diffusion with a higher number of spectral positions. The stabler emitters were, however, found in the central regions of the flake, where the surface is generally flat, as shown before with AFM in Figure 5.5. Interestingly, a similar effect was observed by Noé *et al.*⁵² for luminescent carbon nanotubes (CNT) that were grown onto an hBN substrate, and located either close to the edge or in the center regions. The stability of the emitter in the CNT was found to be much better in the center of the flake than close to the edge.⁵² As a possible reason for this observation, Noé *et al.* pointed to a higher concentration of dangling bonds around the edges and possible accumulation of catalyst particles originating from the chemical vapor deposition of CNTs to contribute to fluctuations in charge. Unfortunately, in our case, the spatial resolution is limited by our confocal microscope, while Noé *et al.* could

observe the distance of their CNT from the edge by AFM imaging.

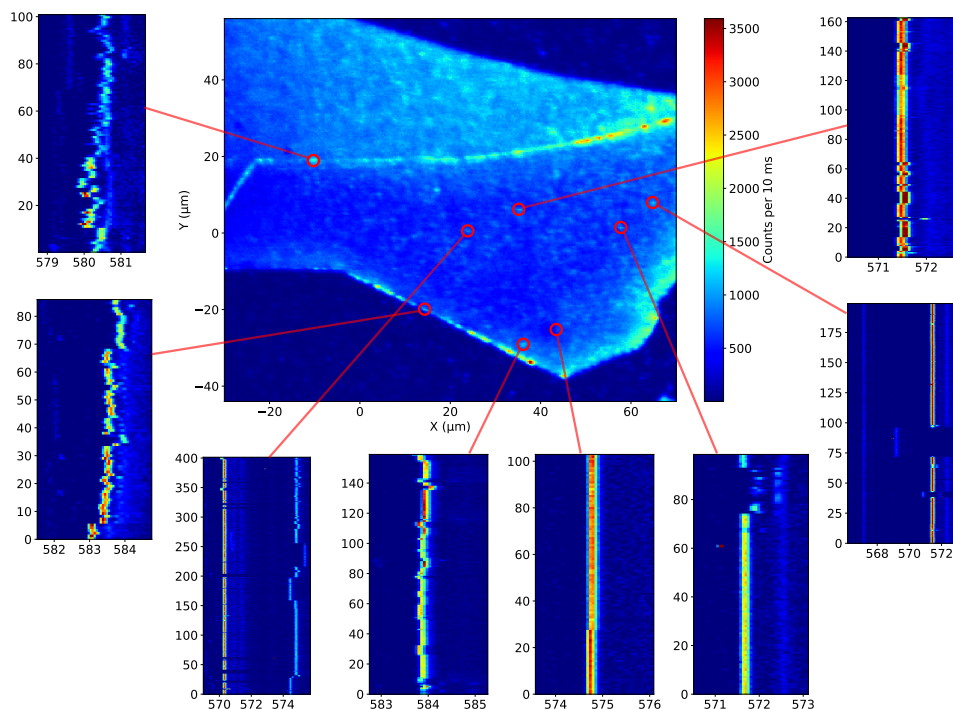


Figure 5.14.: Shown in the middle is a fluorescence image of an annealed (750 °C for 12 hours) hBN flake (NIMS, Japan). The red circles with connected lines correspond to the molecule(s) in the plotted series of spectra, with focus on the 0-0 ZPL. The two spectra on the left correspond to molecules located close to an edge, while the remaining spectra are recorded on extended terraces. The horizontal axes of the spectra correspond to the wavelength and the vertical axes correspond to the spectrum number, where each spectrum was integrated for 1 s with a 1200 lines/mm grating at a 96 μm slit size.

Whether the spectral diffusion that we observe is merely a charge-induced phenomenon, as explained by Noé *et al.*, seems unlikely, based on our previous observations, such as an increased spectral diffusion upon a re-contamination of the surface with *n*-hexadecane and the effect of thermal annealing. Other sources, beyond remote TLSs, were considered as well, such as a slow spatial diffusion of the molecule itself, over the surface. As an initial test, we monitored the polarization of the molecule's fluorescence with a polarizing beam splitter, to observe both the horizontal and vertical component. The relative intensities of these two components showed that there was no

change in the angle of terrylene's long axis (Figure 5.15a and 5.15c). However, without rotation, translational motion is still a possibility. To consider translational motion, we recorded confocal images of two molecules over the course of 90 minutes and fitted their point-spread functions (PSF) to obtain a measurement of distance between the two molecules over time. The position of both molecules was deconvoluted by fitting the PSF to a 2D Gaussian of the form:

$$G(x, y) = B + A \exp(-((x - x_0)^2 + (y - y_0)^2)/\Sigma). \quad (5.2)$$

The term B resembles the background counts, A the amplitude of the PSF, x_0 and y_0 the position of the molecule and Σ the spread of the PSF. The results of the distance between the two molecules, as obtained from the PSF fits, is shown in Figure 5.15g and shows that there is no clear departure from the mean, as expected from random walk behaviour. Hence, if there is any spectral diffusion at all, it is likely very limited. Another source that we checked is the substrate. For defects in hBN, it was shown that coating the silica substrate with a thin layer of alumina would substantially reduce the spectral diffusion,¹² through surface passivation. However, their hBN was only 13 nm thick and thus the emitters, not necessarily present in the top layer, would be much closer to the substrate. Still, we tested whether a sapphire substrate would result in stabler emission, but this is not the case. Finally, we could rule out influences of the substrate on the spectral diffusion when we found an hBN flake that did not completely attach to the substrate. The molecules located on the free-standing part of the flake were still equally unstable as the molecules that were located on the attached part.

Thermal annealing, before deposition of molecules, is the only method that consistently improved the spectral stability of the molecules. In general, we observe a decrease in the number of spectral positions, while also the amplitude of spectral diffusion decreases (Figure 5.13a, 5.13d and 5.13e). Without annealing, the spectral jumping is in general much more complex, consisting of many, possibly coupled, levels, whose population rates could change over time (Figure 5.13c). The scale of the spectral jumps, extending up to a few THz in some cases, and the lack of correlation between spectral diffusion of emitters in the same focal area, points to events in the close vicinity of the molecule. As discussed before, the molecule is likely anchored to (aggregates of) contaminants on the surface or possibly to a defect itself. This (nonfluorescent) contamination itself can be responsible for the spectral jumps, i.e. by a group of atoms tunnelling between two spatial positions, perturbing the optical transition of the terrylene molecule by the electrostatic or elastic dipole-dipole interaction. The contamination likely nucleates around an hBN defect and could explain why we observe more spectral diffusion, as well as more terrylene molecules that anchor to the surface, in the more defect-rich edges of the hBN, as in Figure 5.14. However, the exact nature of these TLSs remains unknown due to the random environment around the molecule.

5.3.5. RESONANT EXCITATION OF THE 0-0 ZPL

The work that I presented so far only shows molecules that were excited by a vibronic transition and not resonantly through the narrow 0-0 ZPL. Moreover, the 0-0 ZPL linewidth resolved in the emission spectrum is limited by the spectrometer resolution

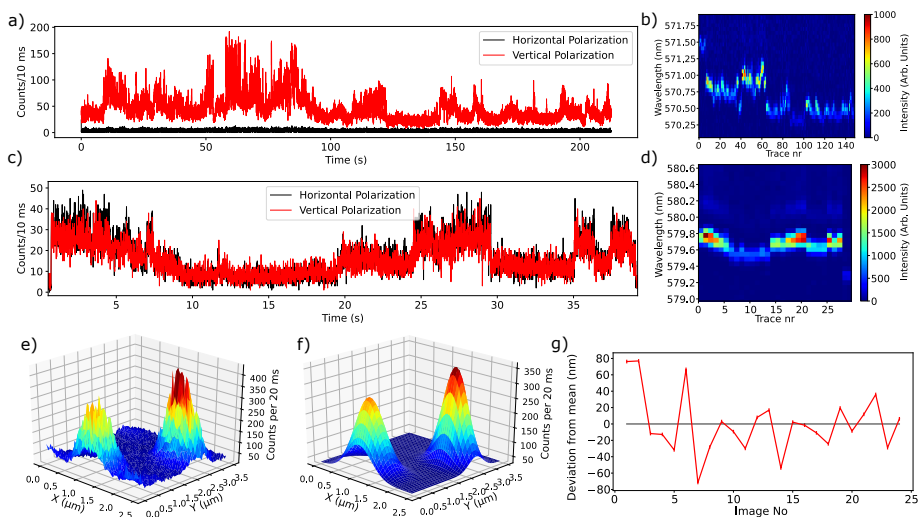


Figure 5.15.: a,b) Fluorescence time trace and spectra of a molecule whose fluorescence is nearly perfectly oriented with the vertical polarization component. Spectral jumps during the time trace have no influence on the horizontal polarization component. c,d) Shows the time trace and spectra of another molecule with comparable intensities in both polarization channels. Also here the spectral jumps have no influence on the ratio of the two polarization components. Around 28 s, the molecule jumps to a spectral position where the excitation was much less efficient, the signal dropped considerably, and therefore the data was cut here. The spectra in b) and d) were recorded with a 1 s integration time. The time scales of the fluorescence time trace and of the spectra are different, due to some delay between the recorded spectra. Panel (e) and (f) show respectively the experimental and fitted point-spread functions of two molecules that are approximately $2 \mu\text{m}$ apart from each other and do not (or barely do) overlap with the PSFs from other molecules. A single scan consisted of 100×100 pixels over a range of $5 \times 5 \mu\text{m}^2$ and took about 200 s to acquire with the scanning mirror. In total, 24 of these images were acquired over the course of 90 minutes with short pauses in between. Panel (g) shows the distance between the two molecules extracted from 24 consecutive confocal images, as in panel (e). The average error of the fit is just a few nm, but the measurements likely have a larger error due to spectral jumps occurring while recording the PSF. For all fitted data, the distance appears to revert around a mean value of $2.18 \mu\text{m}$, and shows no clear trend. Hence, if there is any spatial diffusion, its extent is very limited.

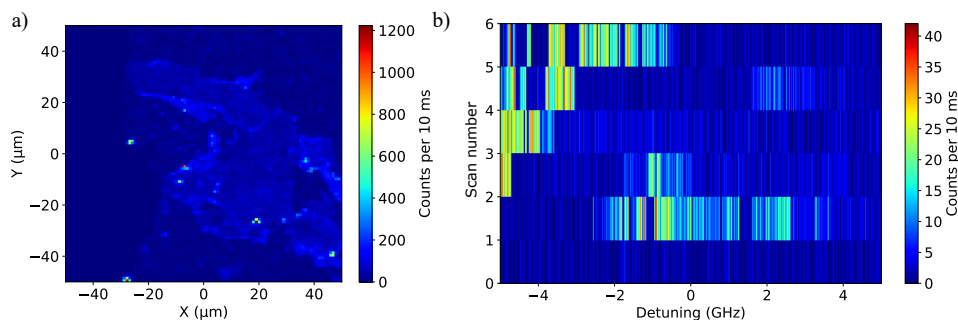


Figure 5.16.: a) Confocal fluorescence map of a collection of hBN flakes, taken at an excitation wavelength of 582.38 nm at a relatively high laser intensity of 350 W/cm^2 . The brightest spot, around $(X = 20, Y = -25)$ corresponds to the emission of the molecule in Figure 5.18. b) Common behavior of a molecule shown in a series of excitation spectra. The series of spectra were taken with the procedure mentioned in the text. In the second line of the scan, the laser was pointed to the position of the molecule. The strong spectral diffusion and blinking makes it difficult to extract a linewidth from this measurement.

($51 \pm 3 \text{ GHz}$ per pixel), while the linewidth of terrylene is expected to be up to three orders of magnitude narrower, around $45 \pm 3 \text{ MHz}$, if it is limited by the measured fluorescence lifetime of $3.6 \pm 0.2 \text{ ns}$. With a tunable dye laser (linewidth of a few MHz) we excited terrylene molecules resonantly. In many cases, the molecule jumped out of resonance with the excitation laser, already in the first scan or the molecule showed such strong spectral diffusion that the molecule appeared intermittently over the full scanning range (Figure 5.16b). With lower excitation intensities of a few W/cm^2 , we could follow the molecules longer. A procedure that worked well consisted of tuning the laser to some wavelength around the peak of the inhomogeneous broadening (Figure 5.10a and 5.10c) and record a fluorescence map of the flake, covered with a high concentration of terrylene. The molecules that are in resonance with the excitation laser will appear as bright spots on the flake region, as shown in Figure 5.16a. Then we start a scan of the laser and while it is running we move the laser to the position of the molecule.

For the remainder of the molecules, not showing behavior as in Figure 5.16b, it was possible to extract a linewidth of the 0-0 ZPL. In general, a Lorentzian distribution fits best to the excitation spectrum's profile (Figure 5.17d). However, in some exceptions, possibly due to fast spectral diffusion, a Gaussian distribution provided a better fit, such as in Figure 5.17b. One of the narrowest linewidths that we could find is shown in Figure 5.17d. In this figure, the Lorentzian fit extracts a linewidth of $390 \pm 10 \text{ MHz}$, which is less than a factor 10 away from the lifetime-limited linewidth of $45 \pm 3 \text{ MHz}$. Furthermore, the molecule has a resonance split into two Lorentzian distributions that are separated by 1.1 GHz. This could be the result of a fast-switching two-level system.

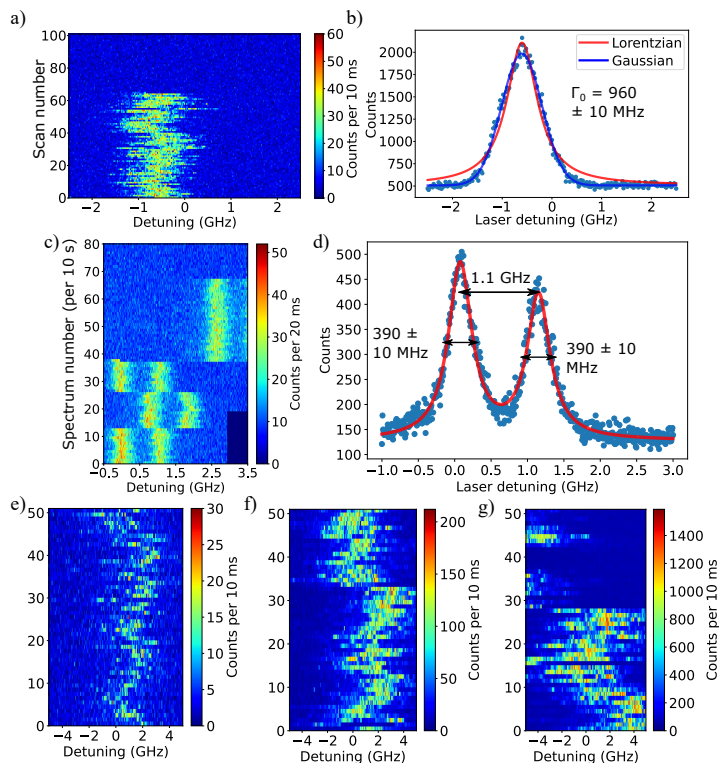


Figure 5.17.: (a) Series of excitation spectra of a molecule at 581.96 nm, taken with 11 W/cm^2 laser intensity. (b) The summed intensity of all the spectra in (a) builds up the figure. The excitation spectrum is fitted with both a Lorentzian and Gaussian distribution. The Gaussian distribution fits best and yields the indicated linewidth. (c) One of the narrowest resonances that are found on hBN is shown in this series of excitation spectra. (d) A fit of two Lorentzian distributions for the two resonance lines present in (c). (e), (f), (g) Spectral diffusion of a molecule recorded at increasing excitation intensities of 1 W/cm^2 in (e), 14 W/cm^2 in (f) and 250 W/cm^2 in (g).

At longer timescales, the molecule also jumps to different spectral positions and jumps out of the scan range after about 10 minutes. This behavior is very common and happens for instance also for the molecule in Figure 5.17c. In rare cases, the molecule stays within the scan region or can be recovered by slightly adjusting the center of the scan. The molecule in Figure 5.17e, 5.17f and 5.17g remains within the scan region, but shows an increasing spectral wandering upon an increase of the excitation laser intensity. A broadening of the linewidth is expected with a higher laser intensity, but the extent of broadening is further increased by a photo-induced spectral diffusion.

The most stable molecule that we found is shown in Figure 5.18a. This molecule

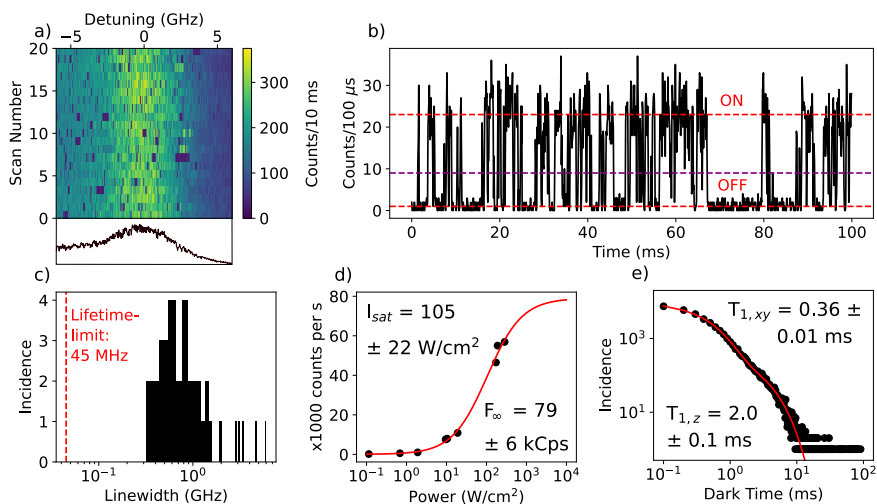


Figure 5.18.: a) Excitation spectrum of the 0-0 ZPL of a single molecule that did not jump out of resonance with the laser, even at higher excitation intensities. The homogeneous linewidth is about 4.7 ± 0.3 GHz and is measured with a scan rate of 5 seconds per row. The line plot underneath the figure shows the asymmetric profile of the 0-0 ZPL. A time trace of the fluorescence signal of this molecule in (b) shows characteristic quantum jumps due to intersystem crossing to the triplet state. However, in some cases the molecule remained dark for much longer times than the triplet lifetime, as is also visible in (a). These long dark times may be attributed to a relatively short spectral jump back and forth between another (out-of-range) spectral position. The purple line represents the threshold set between the ON and OFF state of the fluorescence. c) Distribution of 0-0 ZPLs linewidths found for molecules on different flakes. The red dashed vertical line represents the lower limit set by the fluorescence lifetime. Due to the large distribution of linewidths, the horizontal axis has been set to a logarithmic scale. d) Saturation curve of the fluorescence of the molecule in (a), fitted with $F(I) = F_{\infty}(I/I_s)/(1 + I/I_s)$, where I_s is the saturation intensity of the laser and F_{∞} is the maximum fluorescence rate. The saturation intensity is 105 ± 22 W/cm², 2 orders of magnitude larger than typically obtained with our setup for near-lifetime-limited emitters. This is explained by the 2 orders of magnitude broader linewidth, as the saturation intensity scales linearly with the linewidth of the transition. e) Distribution of dark periods in the resonance fluorescence signal, recorded over 60 s with 100 μ s time bins (as in (b)). The characteristic timescales of the fit (red curve) are shown on the top right and bottom left.

remained at the same resonance frequency, regardless of the excitation intensity. The molecule has a relatively broad linewidth of 4.7 ± 0.3 GHz and an asymmetric profile of the 0-0 ZPL, as shown in the bottom plot of Figure 5.18a. The asymmetric profile might be the result of spectral diffusion to one side. As the molecule remained in resonance, we could record a fluorescence time trace at resonance with the 0-0 ZPL, as shown in Figure 5.18b. The time trace shows quantum jumps that can be assigned to intersystem crossing. The blinking events of longer duration, extending up to tens of ms, are likely from another source, such as jumps back to and from another out-of-range spectral position. To analyze the characteristic time scales of these quantum jumps, we determined a threshold between the ON and OFF state, where a crossing of this threshold would indicate a change from ON to OFF or vice versa. For a time trace of 60 s, the lengths of the period where the molecule was OFF are plotted into a histogram, shown in Figure 5.18e. The histogram is best fitted by a bi-exponential decay, with characteristic triplet lifetimes of 360 ± 10 μ s and 2.0 ± 0.1 ms. We attribute the short decay time to the indistinguishable decays of the in-plane triplet states T_{xy} , while the remaining long decay corresponds to the out-of-plane state T_z .⁵³ The triplet lifetimes agree well with terrylene in the extensively studied hosts *p*-terphenyl⁵⁴⁻⁵⁶ and anthracene.⁵⁷

5

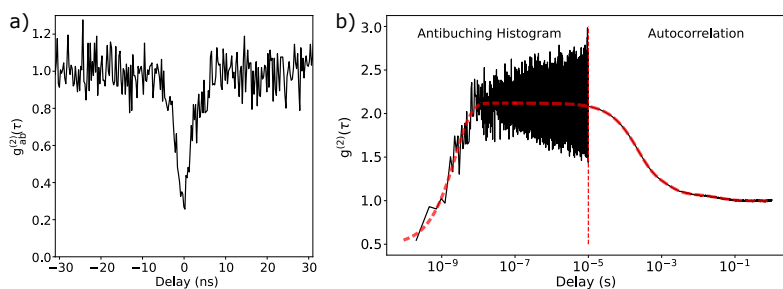


Figure 5.19.: Normalized antibunching histogram of the molecule in Figure 5.18a, measured at resonance with the 0-0 ZPL. No Rabi oscillations are present, but the characteristic time of the exponential increase to unity is shorter than for the off-resonant excitation, indicating that stimulated emission reduces the antibunching time scale. b) The full extent of the correlation function is composed for the left side by a renormalized antibunching histogram and for the right side by the calculated autocorrelation of the fluorescence signal, both recorded with an excitation intensity of around 100 W/cm^2 (see Figure 5.18d for reference).

We continued by recording an antibunching histogram of the resonance fluorescence (Figure 5.19a). No Rabi oscillations are observed in the histogram, which is expected when the linewidth is significantly broadened by dephasing. The measured linewidth of 4.7 ± 0.3 GHz would correspond to a lower bound of the decoherence time T_2 of about 68 ± 4 ps. Combined with the autocorrelation of fluorescence, recorded with 10μ s time bins, we could renormalize the antibunching histogram and extend the full autocorrelation to over 9 orders of magnitude in time (Figure 5.19b).

Although we extensively studied terrylene as a model molecule for characterizing hBN as a potential host, we have tried to measure several other molecules on hBN. The convenience of terrylene emerged particularly due to its broadband absorption at the fixed 532 nm wavelength of the excitation laser, while this was not the case for many other molecules. In this part of the chapter, I will show results of the other molecules that we measured and were either intentionally or unintentionally placed on hBN.

5.4. BEYOND TERRYLENE: OTHER MOLECULES ON HBN

5.4.1. MOLECULE X

On the samples that were prepared by spin coating fluorescent molecules on the hBN flakes, there was regular contamination with fluorescent impurities. One of these impurities, sometimes denoted as molecule X, is particularly present in polymers⁵⁸ and solvents,⁵⁹ such as toluene.⁶⁰ The latter is the solvent that we use in our spin-coating procedure as a transfer solvent for other fluorescent molecules. A spectrum of molecule X on hBN is shown in Figure 5.20 and has the same vibrational fingerprint as found in the literature. Similar to terrylene, the 0-0 ZPLs of these impurity molecules were found over a broad range of wavelengths, extending from 618 nm up to 640 nm, for the 24 molecules that we measured. Similar to terrylene, this wide range of wavelengths for the 0-0 ZPLs of molecule X designates a large inhomogeneous broadening.

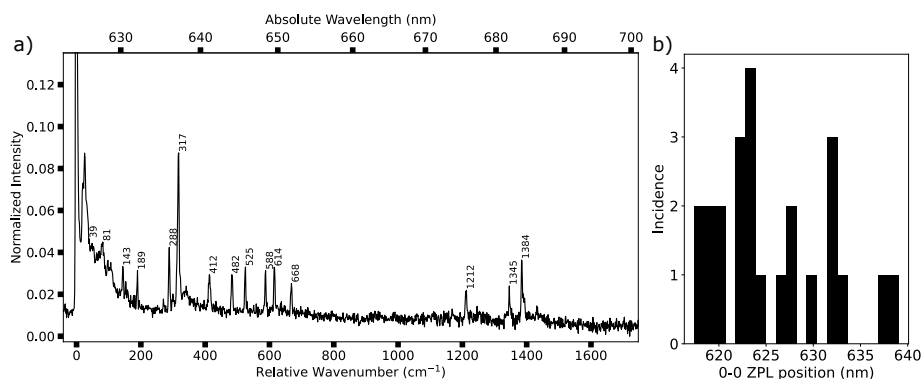


Figure 5.20.: (a) Fluorescence emission spectrum of molecule X with annotated vibrational peaks, normalized to the intensity of the 0-0 ZPL. The excitation frequency was 532 nm. (b) Histogram of the location of the 0-0 ZPL of 24 molecules that shared the vibrational fingerprint as in (a).

As this molecule arises from contact with organic solvents, it can easily end up on the hBN upon “cleaning” it with solvents. There are several reports of emission from hBN, attributed in the papers to defects, that have a similar emission peak.^{8,61} The paper by Ronceray *et al.* treats the activation of emission from hBN by solvent molecules that are possibly binding to hBN surface defects, as the measurements takes place with

hBN submerged in organic solvents. Interestingly, the observed peak of the emission spectrum is in the same region as molecule X. The paper also describes that this effect is observed in many other organic solvents. The fluorescent impurity molecules in those solvents may bind to the hBN, giving off clear point-like emission in wide-field images as they stay longer in one place. Ronceray's reported mechanism of emission, if truly from fluorescent organic impurities in solvents, is interesting. It shows that molecules may possibly prefer to bind to surface defects than on pristine hBN. Therefore, it would be interesting to repeat their experiment with a known dye dissolved in the organic solvent, such as terrylene.

5.4.2. GRAPHENE QUANTUM DOTS

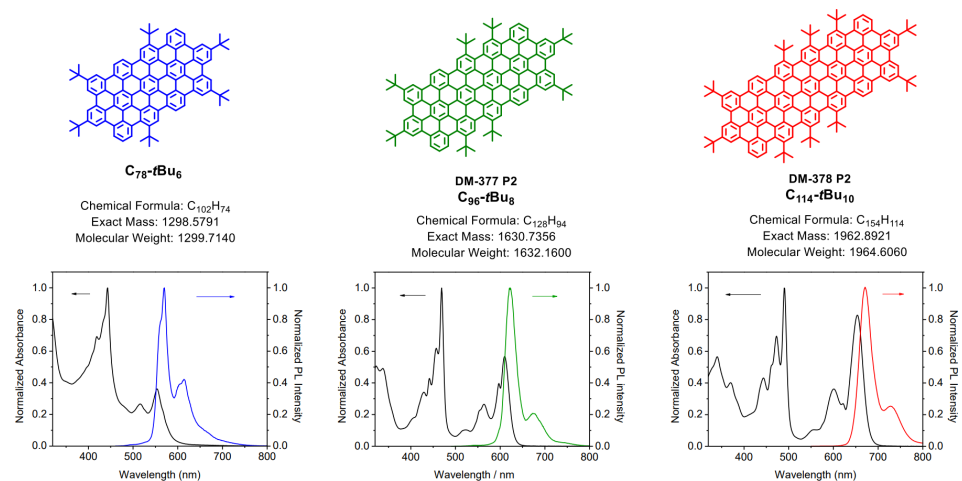


Figure 5.21.: Shown on the top are the chemical structures of the three graphene quantum dots with below their corresponding absorption (black) and fluorescence emission spectra (in color). The image was provided to us by the group of prof. J.S. Lauret from Paris Saclay university. The spectra were measured with 1,2,4-trichlorobenzene as the solvent.

A part from unintentionally placed molecules, such as molecule X, we also performed experiments on a novel family of fluorescent molecules, namely graphene quantum dots (GQDs), in the shape of ribbons (see structures of the three types in Figure 5.21). These molecules were synthesized at Paris Saclay university⁶² and studied by the research group of prof. J.S. Lauret for their strongly fluorescent properties.^{63,64} So far, observing narrow spectra of the GQDs at low temperature is a challenge. A measurement of triangular GQDs in a polystyrene matrix showed broad emission lines that did not reveal the fine structure of the emission spectrum.⁶⁵ The GQD molecules are much bigger than the typical aromatic fluorescent molecules used in single-molecule spectroscopy, and thus finding a suitable host for them to obtain significant line-narrowing of the emission

spectra is a challenge. Apart from the flat ribbon structure there are tert-butyl chains that prevent the molecules from aggregation and thus promote solubility. As such, the molecules could be easily dissolved in toluene. Subsequently, with the GQDs diluted to sub-nM concentrations, we could spin coat them onto annealed hBN flakes. At room temperature, the molecules are easily found using an excitation wavelength of 532 nm. In particular, we focused on the C78 and C96 GQD, where the number represents the amount of carbon atoms present in the aromatic part of the molecule, thus excluding the chains. The room-temperature emission spectra of these two types of GQDs, in ensembles, are shown in Figure 5.22 and reveal that the emission peaks and structure of the spectra are similar to those observed in a 1,2,4-trichlorobenzene solution.

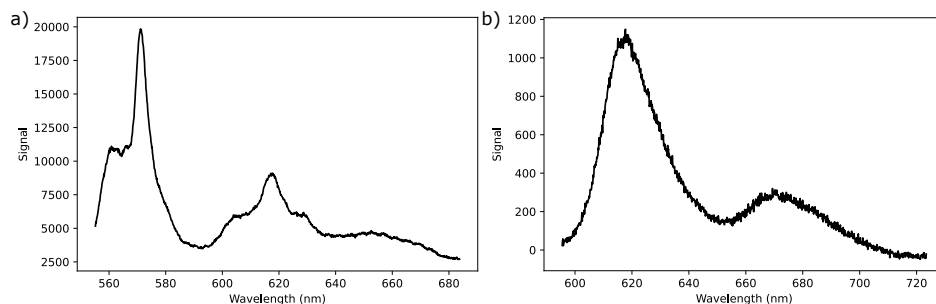


Figure 5.22.: Fluorescence emission spectra of ensembles of respectively the C78 GQD in panel (a) and the C96 GQD in panel (b). Both spectra were taken at room temperature with a 532 nm excitation laser. The spectrum in (a) peaks around 571 nm and the spectrum in (b) has a peak around 618 nm.

Upon cooldown and subsequent line narrowing, the signal from the GQDs was diminishing, probably due to weak or no absorption at all around 532 nm. To improve the signal we required the dye laser for excitation. The dye laser is best optimized for use with the C96 GQD, where a good absorption was measured for some molecules around 570 nm. In the case of Figure 5.23a, the 0-0 ZPL of the C96 QGD is around 615.8 nm, excited with 570.54 nm. The difference of 1288 cm^{-1} is close to the series of vibrational lines around 1300 cm^{-1} in the emission spectrum. The spectrum in Figure 5.23a and 5.23b is likely from a single molecule, as at some point the molecule jumped out of resonance and the signal was lost. The spectra are characterized a large number of vibrational modes, with most of them at low frequency. In part, this could be due to the large size of the molecule, as the number of vibrational modes scales with the number of atoms, while the large size of the molecule can also decrease the energy of some modes. The strongest mode around 128 cm^{-1} in Figure 5.23b is, analogous to the extension mode in other aromatics, where the molecule's length oscillates around equilibrium. For the C78 GQD we were only able to detect a signal at elevated temperatures of around 80 K. Due to the broadened spectrum it is difficult to resolve the vibrational spectrum of this molecule, as shown in Figure 5.23c.

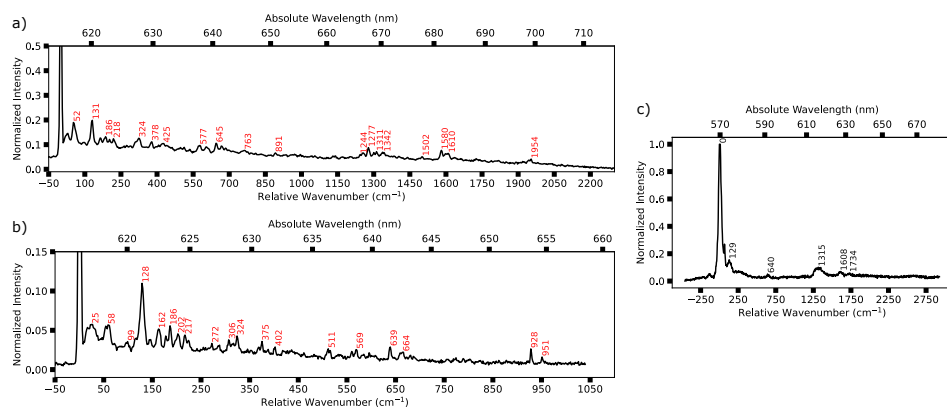


Figure 5.23.: Panel (a) shows the full emission spectrum of the C96 GQD at 2 K, excited at 570.74 nm and taken with a 600 lines/mm grating at a 0.1 mm slit size. The higher resolution spectrum, taken with a 1200 lines/mm grating and a 0.1 mm slit size, is shown in panel (b). In panel (c) an emission spectrum of the C78 GQD is shown, which was only observed at elevated temperatures. In this case the temperature is around 80 K and is responsible for the broadened linewidth. The C96 GQD molecule in (a) and (b) has a 0-0 ZPL around 615.8 nm and the C78 GQD molecule in (c) has a 0-0 ZPL around 569.7 nm.

5

The spectra of GQDs on hBN show that hBN is a promising host for other molecules than only terrylene. In particular, the notion that hBN can be applied for rather bulky molecules such as GQDs may underpin the universality of hBN as a host matrix for fluorescent molecules. Moreover, many properties of these GQDs are still unknown, such as their photophysical parameters (triplet blinking) and could in best case, such as for terrylene in Figure 5.18, be studied at the single-molecule level. However, it is very important to consider what excitation wavelength is optimal for each type of molecule. In addition, GQDs (and molecule X) are showing the same type of spectral diffusion as observed for terrylene, which can quickly move the molecules out of resonance with the laser. Terrylene, on the other hand, stayed most of the times in resonance with the 532 nm laser. As a possible solution for the elimination of spectral diffusion we considered adding another layer on top of the hBN, thus encapsulating the molecules.

5.5. ENCAPSULATION OF TERRYLENE

5.5.1. TRANSFER OF LARGE AREA HBN

In case the spectral diffusion is primarily caused by degrees of freedom for the organic contamination present on the surface, then perhaps this spectral diffusion could be suppressed by passivating the environment through encapsulation by another hBN layer. In fact, encapsulation by hBN is already a common procedure to for example improve

the linewidth of emission from excitons in transition metal dichalcogenides (TMDs).^{66,67} The encapsulation of large structures such as TMDs is not difficult, but for small-sized molecules, such as terrylene, the encapsulation could push away the molecules. This self-cleaning method is in most cases desired for having a clean interface in stacked structures. As mentioned in section 5.3.1., the encapsulation may also cause pile-up of residues and our fluorescent molecules into air pockets/bubbles.²⁸ Intuitively, the encapsulation could be best performed with a thin layer or monolayer of hBN, to have easier adaption of the top layer to the part to encapsulate, without exerting much pressure on the bottom hBN. To this end, we used 13 nm hBN grown by chemical-vapor deposition onto a copper foil (obtained from the company Graphene Supermarket). The copper foil can be slowly (typically less than an hour) dissolved in an etchant solution (10% ammonium persulfate in water). As the copper is dissolved, a slide of teflon with a hole in the middle floats in the water and creates surface tension (Figure 5.24a), which will keep the hBN floating on the water surface after the copper is completely dissolved. Then the sample is slowly pushed towards the water and the whole layer attaches to the substrate as it gets into contact. The procedure for hBN transfer from copper foil is based on this work.⁶⁸ Although the transfer was successful and allowed the encapsulation of many flakes at once (the monolayer can be millimeters large, see Figure 5.24b), this rather “dirty” method left behind a lot of emission on our samples, which made it difficult to distinguish emission from terrylene.

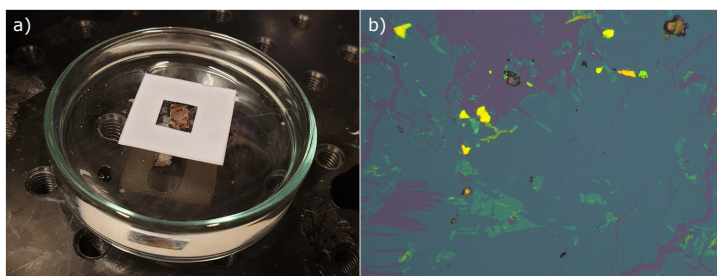


Figure 5.24.: Panel (a) shows a piece of copper foil, coated with a 13 nm thick hBN layer, floating in the middle of a hole in a Teflon slide that also floats on an etchant solution of 10% ammonium persulfate in water. Panel (b) shows hBN flakes on a substrate (most of them in yellow or green color), with areas that are encapsulated covered by a bluish film. Note that upon transfer the sheet tears and does not cover all parts of the substrate.

5.5.2. FLAKE-ON-FLAKE ENCAPSULATION

Another method for encapsulation is the use of the stamping technique. This method is very similar to exfoliation in the sense that a polymer layer (polycarbonate (PC) or PDMS) is used to pick up a flake (for example from a substrate or exfoliated on tape) and positioned above (using a microscope that has two independent micromanipulators) and pushed towards another flake that is already on a substrate.

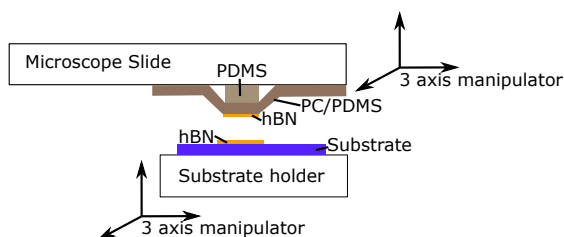


Figure 5.25.: Schematic of the stamping procedure with two microscope slides connected to individual micromanipulators. The substrate with the exfoliated hBN is attached to a substrate holder by vacuum. A microscope slide is prepared with a small piece of PDMS gel (from Gel-Pak) to support a layer of polycarbonate (PC) or PDMS tape (from Gel-Pak as well), with exfoliated hBN attached to it. The manipulators can be used to position the two flakes on top of each other and to approach.

5

The procedure for stamping of hBN flakes, and many other 2D materials, is schematically shown in Figure 5.25. The hBN for transfer is prepared by the scotch-tape method, as described before. A piece of PC or PDMS tape is then pressed on the scotch tape, such that some hBN flakes attach to it. Subsequently, the PDMS tape is fixed to the microscope slide, where the PDMS gel makes sure a part of it is suspended. This needs to be the region with the flakes of interest present. The flake to transfer is then positioned on top of the flake that needs to be covered and the two flakes are moved towards each other until there is slight contact of the film with the substrate. Subsequently, the sample is heated till 60-90 °C, such that thermal expansion creates full contact between the PDMS or PC film and the substrate. Then the sample is cooled back to room temperature, while the thermal contraction makes the film lose contact again with the substrate. When transfer of the flake was not successful the procedure was repeated with or without some minor changes in the parameters.

The result of the encapsulation using the stamping method is shown in Figure 5.26a and 5.26b. When the molecules are encapsulated, annealing was not performed anymore. However, we could anneal the bottom flake before deposition of molecules and encapsulation, as was done for the flake in Figure 5.26b. Interestingly, we found a large number of terylene molecules on the non-annealed flake in the encapsulated part, but only one terylene molecule was found on the encapsulated part of the annealed flake. Moreover, the background fluorescence was much higher for the case of the annealed bottom flake. This could be a result of the annealing, which may cause the formation of molecule emitters due to the presence of organic contamination between the interface of silica and hBN.¹⁵ However, none of this emission was narrow at low temperature. The narrow emission that we could find was due to the presence of terylene. However, the spectral diffusion is still a problem in the encapsulated areas of the hBN flake, as shown in Figure 5.27. The only molecule that we could find on the annealed flake, covered by a non-annealed flake, shows spectral diffusion (Figure 5.27a). Similarly, the

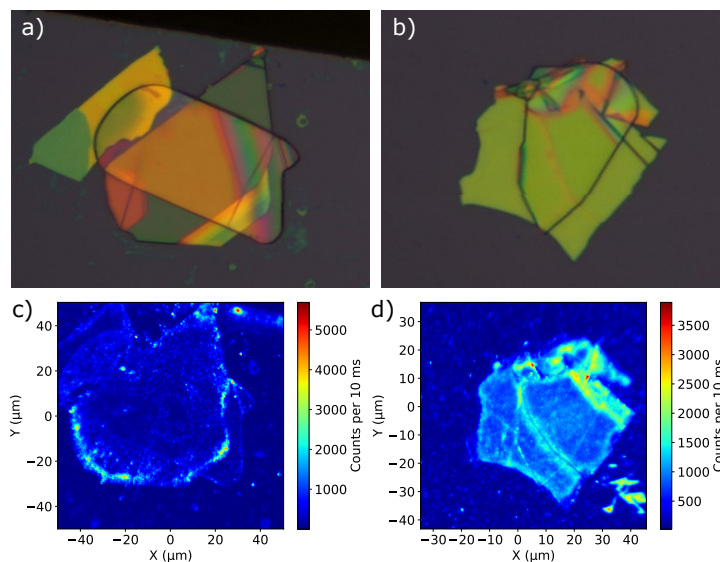


Figure 5.26.: Examples of encapsulation of an hBN flake by another flake of hBN, by the stamping method. In panel (a) the bottom hBN was not annealed and in panel (b) the bottom hBN was annealed. In both cases, molecules were deposited by sublimation before encapsulation (and annealing). The corresponding fluorescence maps of the flakes in (a) and (b) are respectively shown in panel (c) and (d). Note that the background is much higher for the annealed flake (d) compared to the non-annealed flake in (c). Hundreds of terrylene molecules were found on the non-annealed flake, while only a single terrylene molecule was found on the annealed flake.

molecules on the non-annealed flake show spectral diffusion as well (Figure 5.27b and 5.27c), on a scale that we regularly observe on non-encapsulated hBN flakes. Hence, the encapsulation of the molecules does not seem to improve the spectral stability, which might be due to the pile-up of contamination in areas where terrylene is also located. Of course, many parameters in the preparation of these encapsulated samples can be varied and may lead to different results. This can be for example the amount of force that we exert during stamping or the amount of heating we provide to make the top layer stick well.

There are possibly alternatives to the encapsulation methods that we used so far. This could be for instance exfoliation in a high vacuum environment, to keep all the layers in very clean condition. This could be combined with in-situ evaporation of the fluorescent molecules on a cold hBN surface. However, this would require sophisticated equipment. Another appealing alternative is the use of boron nitride nanotubes, which have proven to be able to encapsulate dye molecules and protect them from photodegradation at room temperature.⁶⁹

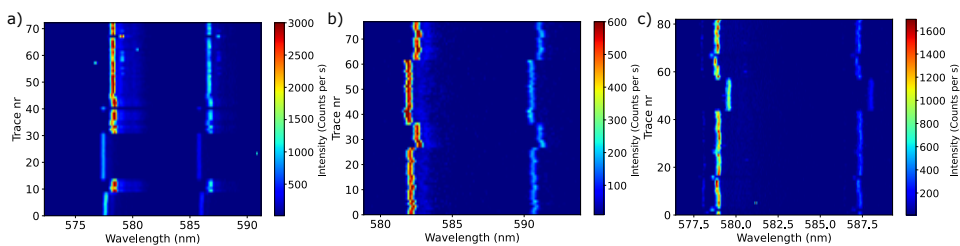


Figure 5.27.: Series of emission spectra of encapsulated molecules. The molecule in panel (a) was located in the encapsulated part of the annealed bottom flake. It was also the only molecule that we could find on this sample. Panel (b) and panel (c) show examples of spectral diffusion that we observed for molecules that were located on the non-annealed hBN flake, inside the encapsulated region.

5

5.6. WHAT CAN WE LEARN FROM THE LITERATURE ON HBN 'DEFECTS'?

Although the origin of emission of many emitters associated to hBN is unknown and some of them are disputed to originate from defects, but possibly organic molecules, we can still learn from the various experiments that have been undertaken to improve the emitter's quality and tuning of its properties. In particular, if the experiments are indeed performed unintentionally on molecule emitters, the experiments are very relevant.

Comparing the spectral properties of single terrylene molecules on hBN to the properties of hBN emitters, the similarities are striking. Homogeneous linewidths of about 1 GHz on average are also typical for other reported emitters associated to hBN.^{38,39,70,71} Moreover, spectral diffusion, large enough to observe with a spectrometer, is also frequently reported for hBN emitters.^{12,38,39,71–73} Methods of improvement for the quality of hBN emitters could therefore be possibly applied to our molecules as well. In the following part, I will show two experiments from the literature that are interesting candidates for follow-up experiments for terrylene on hBN, which we have tried to build up as well.

Interesting work by the group of Atwater⁷⁴ shows that high electric fields can improve the spectral properties of an hBN emitter, leading to almost lifetime-limited linewidths. This improvement was achieved by creating a heterostructure of graphene/hBN/hBN/graphene, where both graphene layers would act as independent electrodes, while the emitter was located in one of the hBN layers (or between). The explained mechanism of their work is that the very high electric field, in the order of 1-2 MV/cm, would deplete charge traps in the hBN, causing a strong reduction in charge noise, analogous to reports on the reduction of charge noise in semiconductor quantum dots using electric fields.⁷⁵ Even more surprising is the measured temperature dependence of the linewidth. The linewidth of the emitter is still below 1 GHz at a

temperature of 100 K, while the broadening is purely phonon-induced and lacks a linear component, i.e. a pure T^3 -dependence. This could suggest that the electric field greatly suppresses the activity of two-level systems (TLSs) at higher temperatures as well, and cancels the linear broadening term that we also observe for our molecules. In section 5.5 we have shown that it is possible to encapsulate molecules between hBN. However, there is no definitive proof that the molecules are indeed in the encapsulated region. With a similar stack of hBN encapsulated molecules between graphene electrodes we could also prove that the molecules are really in-between the hBN flakes when their fluorescence is not quenched through contact with the graphene.

We also tried to make a similar heterostructure of hBN in between graphite (or multilayer graphene) electrodes (Figure 5.28a). In the first attempt we noticed that the thickness of the top graphite layer is very important for the measured fluorescence. If the layer is too thick, the fluorescence cannot penetrate the layer, as well as excitation light is only weakly transmitted (absorption is about 2.3% per layer in the visible). Consequently, the area where all layers overlap does not show any fluorescence (Figure 5.28b).

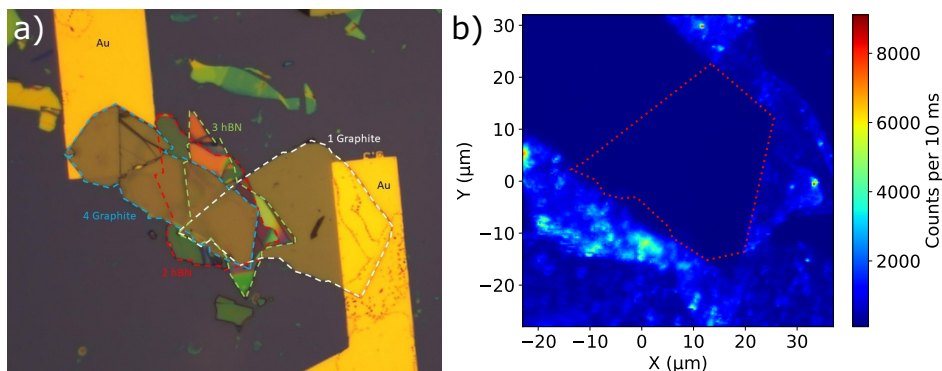


Figure 5.28.: a) Microscope image of the heterostructure with at the bottom a layer of graphite in contact with one of the gold electrodes. Followed by two hBN flakes on top of each other, with molecules deposited in between and a top graphite layer connected to the other electrode. Panel (b) shows the fluorescence image of the region where all layers overlap, bordered with a red dashed line. The fluorescence signal in this region is very weak, which is possibly due to the low transparency of the top graphene layer. See also the low contrast on the left electrode in (a), where the top graphene layer overlaps with the highly-reflecting gold.

With a thinner graphite layer, as shown in Figure 5.29, we were able to detect some fluorescence within the overlap region. However, the signal was relatively weak and recording a spectrum required an integration time of about 30 seconds at a high excitation intensity ($> 100 \text{ kW/cm}^2$). Consequently, the spectrum of the terylene molecules is less

well visible due to overlap with strong Raman signals from graphene. No spectral shift or stabilization of the fluorescence signal was observed on the spectrometer. This could be related to the intensity of the field, which depends on the voltages applied (10 V over the junction area) and the thicknesses of the hBN layers. However, the fact that we can detect fluorescence from single terrylene molecules indicates that the emitters are not quenched by the graphene and are likely located between the hBN layers. With better control over the thicknesses of the hBN layers and the top graphite layer the experiment can be improved, while spectral shifts are more easily visualized by resonant excitation of the 0-0 ZPLs.

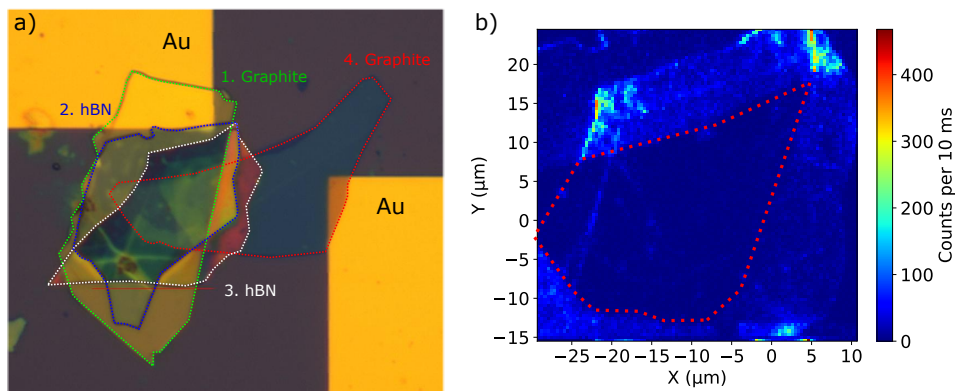


Figure 5.29.: Panel (a) shows a heterostructure with a thinner top graphite layer (see better contrast of overlap on the right electrode). Panel (b) shows the middle area of the heterostructure where all layers overlap. Some fluorescence signal is visible in the overlap region, bordered with the red dashed line.

One of the marked observations of terrylene on hBN is the existence of a very large inhomogeneous broadening, which also exists for molecule X. Compared to organic matrices, hBN can have significant tensile or shear strain in the layer, which can be present on nanometer scales.⁷⁶ Moreover, a report on the stretching of hBN has revealed that the emission wavelength of an emitter can be red-shifted up to tens of nm.⁷⁷ The experiment works by using an elastic substrate, such as PDMS, for the hBN, which can be stretched up to a few percent. Of course, the exact stretching of hBN itself is not known, as it depends on how well hBN conforms to the substrate. The notion that tensile strain, in this particular case, can strongly affect the emission wavelength, could be an appealing explanation for the large inhomogeneous broadening, i.e. large variations in the local environment of the molecule within diffraction-limited areas, that we observe for terrylene on hBN. We therefore propose a similar experiment that can test this hypothesis. For an optimal resolution of the spectra, this experiment could be best carried out at low temperature, using a piezo actuator to controllably exert strain and a structure that can amplify the expansion/contraction of the piezo. We have tried

a quick test at room temperature, by using hBN exfoliated onto PDMS. However, the large amount of Raman signal from the PDMS and the weak contrast of hBN flakes on PDMS (no interference effects giving colored flakes) made it difficult to observe the signal from single terrylene molecules.

5.7. CONCLUSION AND OUTLOOK

We have shown that terrylene molecules adsorbed on the surface of hBN become narrow emitters at low temperature, with linewidths as narrow as a few 100 MHz up to a few GHz. Their relative spectral stability, in contrast to single molecules adsorbed on any other surface so far, made it possible to observe 0-0 ZPLs on a surface. Moreover, we have found a way to considerably improve the spectral stability by annealing the hBN substrates before the molecules were deposited, which points to dynamics in the (organic) contamination as a potential source of the spectral jumps. Our work shows that narrow emission can also be observed for other molecules, if the right excitation wavelength is used. For example, the narrow emission from bulky graphene quantum dots was never observed before in other host matrices. This could indicate that hBN might be a host matrix for potentially many fluorescent molecules. This requires, however, more study on different types of molecules.

In future experiments, a well-known system such as terrylene could help shed light on the various issues of spectral instabilities and dephasing mechanisms, in order to improve the quality of other emitters hosted by hBN. For that reason, we propose two experiments that are based on experiments already conducted for the unknown emitters associated to hBN, to be repeated with terrylene molecules. The first experiment, which consists of applying large electric fields to the molecules, could potentially resolve the spectral diffusion and improve coherence properties of the molecules. In addition, if the action of two-level systems is completely suppressed by the large electric field, the strong linear broadening of the linewidth could be resolved as well, which may make narrow emission at higher-than-liquid-helium temperatures possible. The second experiment consists of the controlled application of strain on the hBN, to observe whether it would be possible to tune the molecule's resonance by strain. Moreover, it would be interesting to observe whether the molecular structure of terrylene can adapt to changes in the lattice parameters of hBN and whether this could be responsible for the reduced Franck-Condon factors that we observe for red-shifted molecules. In that way, the photon indistinguishability could perhaps be tuned and improved.

REFERENCES

- (1) Cassabois, G.; Valvin, P.; Gil, B. *Nature Photonics* **2016**, *10*, 262–266.
- (2) Gaudreau, L.; Tielrooij, K. J.; Prawiroatmodjo, G. E. D. K.; Osmond, J.; De Abajo, F. J. G.; Koppens, F. H. L. *Nano Letters* **2013**, *13*, 2030–2035.
- (3) Han, S.; Qin, C.; Song, Y.; Dong, S.; Lei, Y.; Wang, S.; Su, X.; Wei, A.; Li, X.; Zhang, G.; Chen, R.; Hu, J.; Xiao, L.; Jia, S. *The Journal of Chemical Physics* **2021**, *155*, 244301.
- (4) Hod, O. *Journal of Chemical Theory and Computation* **2012**, *8*, 1360–1369.
- (5) Chen, T.-A.; Chuu, C.-P.; Tseng, C.-C.; Wen, C.-K.; Wong, H.-S. P.; Pan, S.; Li, R.; Chao, T.-A.; Chueh, W.-C.; Zhang, Y.; Fu, Q.; Yakobson, B. I.; Chang, W.-H.; Li, L.-J. *Nature* **2020**, *579*, 219–223.
- (6) Maestre, C.; Toury, B.; Steyer, P.; Garnier, V.; Journet, C. *Journal of Physics: Materials* **2021**, *4*, 044018.
- (7) Watanabe, K.; Taniguchi, T.; Kanda, H. *Nature Materials* **2004**, *3*, 404–409.
- (8) Tran, T. T.; Bray, K.; Ford, M. J.; Toth, M.; Aharonovich, I. *Nature Nanotechnology* **2016**, *11*, 37–41.
- (9) Bourrellier, R.; Meuret, S.; Tararan, A.; Stéphan, O.; Kociak, M.; Tizei, L. H. G.; Zobelli, A. *Nano Letters* **2016**, *16*, 4317–4321.
- (10) Camphausen, R.; Marini, L.; Tawfik, S. A.; Tran, T. T.; Ford, M. J.; Palomba, S. *APL Photonics* **2020**, *5*, 076103.
- (11) Gu, R.; Wang, L.; Zhu, H.; Han, S.; Bai, Y.; Zhang, X.; Li, B.; Qin, C.; Liu, J.; Guo, G.; Shan, X.; Xiong, G.; Gao, J.; He, C.; Han, Z.; Liu, X.; Zhao, F. *ACS Photonics* **2021**, *8*, 2912–2922.
- (12) Li, X.; Shepard, G. D.; Cupo, A.; Camporeale, N.; Shayan, K.; Luo, Y.; Meunier, V.; Strauf, S. *ACS Nano* **2017**, *11*, 6652–6660.
- (13) Aharonovich, I.; Tétienne, J.-P.; Toth, M. *Nano Letters* **2022**, *22*, 9227–9235.
- (14) Dev, P. *Physical Review Research* **2020**, *2*, 022050.
- (15) Neumann, M.; Wei, X.; Morales-Inostroza, L.; Song, S.; Lee, S.-G.; Watanabe, K.; Taniguchi, T.; Göttinger, S.; Lee, Y. H. *ACS Nano* **2023**, *17*, 11679–11691.
- (16) Fleury, L.; Gruber, A.; Dräbenstedt, A.; Wrachtrup, J.; von Borczyskowski, C. *The Journal of Physical Chemistry B* **1997**, *101*, 7933–7938.
- (17) Gmeiner, B.; Maser, A.; Utikal, T.; Göttinger, S.; Sandoghdar, V. *Physical Chemistry Chemical Physics* **2016**, *18*, 19588–19594.

- (18) Vainer, Y. G.; Sobolev, Y. I.; Naumov, A. V.; Osad'ko, I. S.; Kador, L. *Faraday Discussions* **2015**, *184*, 237–249.
- (19) Basché, T.; Bräuchle, C. *Chemical Physics Letters* **1991**, *181*, 179–186.
- (20) Pazzagli, S.; Lombardi, P.; Martella, D.; Colautti, M.; Tiribilli, B.; Cataliotti, F. S.; Toninelli, C. *ACS Nano* **2018**, *12*, 4295–4303.
- (21) Schofield, R. C.; Burdekin, P.; Fasoulakis, A.; Devanz, L.; Bogusz, D. P.; Hoggarth, R. A.; Major, K. D.; Clark, A. S. *ChemPhysChem* **2022**, *23*, e202100809.
- (22) Faez, S.; van der Molen, S. J.; Orrit, M. *Physical Review B* **2014**, *90*, 205405.
- (23) Türschmann, P.; Rotenberg, N.; Renger, J.; Harder, I.; Lohse, O.; Utikal, T.; Götzinger, S.; Sandoghdar, V. *Nano Letters* **2017**, *17*, 4941–4945.
- (24) Shkarin, A.; Rattenbacher, D.; Renger, J.; Hönl, S.; Utikal, T.; Seidler, P.; Götzinger, S.; Sandoghdar, V. *Physical Review Letters* **2021**, *126*, 133602.
- (25) Ren, P.; Wei, S.; Liu, W.; Lin, S.; Tian, Z.; Huang, T.; Tang, J.; Shi, Y.; Chen, X.-W. *Nature Communications* **2022**, *13*, 3982.
- (26) Novoselov, K. S.; Geim, A. K.; Morozov, S. V.; Jiang, D.; Zhang, Y.; Dubonos, S. V.; Grigorieva, I. V.; Firsov, A. A. *Science* **2004**, *306*, 666–669.
- (27) Anzai, Y.; Yamamoto, M.; Genchi, S.; Watanabe, K.; Taniguchi, T.; Ichikawa, S.; Fujiwara, Y.; Tanaka, H. *Applied Physics Express* **2019**, *12*, 055007.
- (28) Haigh, S. J.; Gholinia, A.; Jalil, R.; Romani, S.; Britnell, L.; Elias, D. C.; Novoselov, K. S.; Ponomarenko, L. A.; Geim, A. K.; Gorbachev, R. *Nature Materials* **2012**, *11*, 764–767.
- (29) Zhang, G.; Chang, Y.; Yan, B. *Crystals* **2023**, *13*, 304.
- (30) Sonntag, J.; Li, J.; Plaud, A.; Loiseau, A.; Barjon, J.; Edgar, J. H.; Stampfer, C. *2D Materials* **2020**, *7*, 031009.
- (31) Choi, S.; Tran, T. T.; Elbadawi, C.; Lobo, C.; Wang, X.; Juodkazis, S.; Seniutinas, G.; Toth, M.; Aharonovich, I. *ACS Applied Materials & Interfaces* **2016**, *8*, 29642–29648.
- (32) Yim, D.; Yu, M.; Noh, G.; Lee, J.; Seo, H. *ACS Applied Materials & Interfaces* **2020**, *12*, 36362–36369.
- (33) Gasparutti, I.; Song, S. H.; Neumann, M.; Wei, X.; Watanabe, K.; Taniguchi, T.; Lee, Y. H. *ACS Applied Materials & Interfaces* **2020**, *12*, 7701–7709.
- (34) Navarro, P.; Tian, Y.; van Stee, M.; Orrit, M. *ChemPhysChem* **2014**, *15*, 3032–3039.
- (35) Tchénié, P.; Myers, A. B.; Moerner, W. *Chemical Physics Letters* **1993**, *213*, 325–332.
- (36) Kummer, S.; Kulzer, F.; Kettner, R.; Basché, T.; Tietz, C.; Glowatz, C.; Kryschi, C. *The Journal of Chemical Physics* **1997**, *107*, 7673–7684.
- (37) Navarro, P.; Bocquet, F. C.; Deperasińska, I.; Pirug, G.; Tautz, F. S.; Orrit, M. *The Journal of Physical Chemistry C* **2015**, *119*, 277–283.

- (38) Sontheimer, B.; Braun, M.; Nikolay, N.; Sadzak, N.; Aharonovich, I.; Benson, O. *Physical Review B* **2017**, *96*, 121202.
- (39) White, S.; Stewart, C.; Solntsev, A. S.; Li, C.; Toth, M.; Kianinia, M.; Aharonovich, I. *Optica* **2021**, *8*, 1153.
- (40) Vainer, Y. G.; Naumov, A. V.; Kol'chenko, M. A.; Personov, R. I. *physica status solidi (b)* **2004**, *241*, 3480–3486.
- (41) Banasiewicz, M.; Wiącek, D.; Kozankiewicz, B. *Chemical Physics Letters* **2006**, *425*, 289–293.
- (42) Nicolet, A. A. L.; Bordat, P.; Hofmann, C.; Kol'chenko, M. A.; Kozankiewicz, B.; Brown, R.; Orrit, M. *ChemPhysChem* **2007**, *8*, 1929–1936.
- (43) Grandi, S.; Major, K. D.; Polisseni, C.; Boissier, S.; Clark, A. S.; Hinds, E. A. *Physical Review A* **2016**, *94*, 063839.
- (44) Clear, C.; Schofield, R. C.; Major, K. D.; Iles-Smith, J.; Clark, A. S.; McCutcheon, D. P. S. *Physical Review Letters* **2020**, *124*, 153602.
- (45) Tchénio, P.; Myers, A. B.; Moerner, W. *Journal of Luminescence* **1993**, *56*, 1–14.
- (46) Li, C.; Xu, Z.-Q.; Mendelson, N.; Kianinia, M.; Toth, M.; Aharonovich, I. *Nanophotonics* **2019**, *8*, 2049–2055.
- (47) Zobelli, A.; Ewels, C. P.; Gloter, A.; Seifert, G. *Physical Review B* **2007**, *75*, 094104.
- (48) Chen, X.; Sun, H.; Zhang, W.; Tan, C.; Liu, X.; Zhao, J.; Hou, L.; Gao, Y.; Song, J.; Chen, Z. *Vacuum* **2022**, *199*, 110935.
- (49) Arnold, T.; Forster, M.; Fragkoulis, A. A.; Parker, J. E. Structure of Normal-Alkanes Adsorbed on Hexagonal-Boron Nitride, EN, research-article, 2014.
- (50) Glushkov, E.; Macha, M.; R ath, E.; Navikas, V.; Ronceray, N.; Cheon, C. Y.; Ahmed, A.; Avsar, A.; Watanabe, K.; Taniguchi, T.; Shorubalko, I.; Kis, A.; Fantner, G.; Radenovic, A. *ACS Nano* **2022**, *16*, 3695–3703.
- (51) Xu, Z.-Q.; Elbadawi, C.; Tran, T. T.; Kianinia, M.; Li, X.; Liu, D.; Hoffman, T. B.; Nguyen, M.; Kim, S.; Edgar, J. H.; Wu, X.; Song, L.; Ali, S.; Ford, M.; Toth, M.; Aharonovich, I. *Nanoscale* **2018**, *10*, 7957–7965.
- (52) No e, J. C.; Nutz, M.; Reschauer, J.; Morell, N.; Tsioutsios, I.; Reserbat-Plantey, A.; Watanabe, K.; Taniguchi, T.; Bachtold, A.; H ogele, A. *Nano Letters* **2018**, *18*, 4136–4140.
- (53) Lawetz, V.; Orlandi, G.; Siebrand, W. *The Journal of Chemical Physics* **1972**, *56*, 4058–4072.
- (54) Kummer, S.; Basch e, T.; Br auchle, C. *Chemical Physics Letters* **1994**, *229*, 309–316.
- (55) Basch e, T.; Kummer, S.; Br auchle, C. *Nature* **1995**, *373*, 132–134.
- (56) Banasiewicz, M.; Morawski, O.; Wiącek, D.; Kozankiewicz, B. *Chemical Physics Letters* **2005**, *414*, 374–377.

- (57) Nicolet, A.; Kol'chenko, M. A.; Kozankiewicz, B.; Orrit, M. *The Journal of Chemical Physics* **2006**, *124*, 164711.
- (58) Fleury, L.; Tamarat, P.; Kozankiewicz, B.; Orrit, M.; Lapouyade, R.; Bernard, J. *Molecular Crystals and Liquid Crystals* **1996**, *283*, 81–87.
- (59) Neumann, A.; Lindlau, J.; Thoms, S.; Basché, T.; Högele, A. *Nano Letters* **2019**, *19*, 3207–3213.
- (60) Trinh, C. T.; Lee, J.; Lee, K.-G. *Scientific Reports* **2018**, *8*, 8273.
- (61) Ronceray, N.; You, Y.; Glushkov, E.; Lihter, M.; Rehl, B.; Chen, T.-H.; Nam, G.-H.; Borza, F.; Watanabe, K.; Taniguchi, T.; Roke, S.; Keerthi, A.; Comtet, J.; Radha, B.; Radenovic, A. *Nature Materials* **2023**, *22*, 1236–1242.
- (62) Lavie, J.; Vu, V. B.; Medina-Lopez, D.; Dappe, Y.; Liu, T.; Rondin, L.; Lauret, J.-S.; Latil, S.; Campidelli, S. *Helvetica Chimica Acta* **2023**, *106*, e202300034.
- (63) Levy-Falk, H.; Capelle, O.; Liu, T.; Medina-Lopez, D.; Deleporte, E.; Campidelli, S.; Rondin, L.; Lauret, J.-S. *physica status solidi (b)* **2023**, *260*, 2300310.
- (64) Medina-Lopez, D.; Liu, T.; Osella, S.; Levy-Falk, H.; Rolland, N.; Elias, C.; Huber, G.; Ticku, P.; Rondin, L.; Joussetme, B.; Beljonne, D.; Lauret, J.-S.; Campidelli, S. *Nature Communications* **2023**, *14*, 4728.
- (65) Liu, T.; Carles, B.; Elias, C.; Tonnelé, C.; Medina-Lopez, D.; Narita, A.; Chassagneux, Y.; Voisin, C.; Beljonne, D.; Campidelli, S.; Rondin, L.; Lauret, J.-S. *The Journal of Chemical Physics* **2022**, *156*, 104302.
- (66) Ajayi, O. A.; Ardelean, J. V.; Shepard, G. D.; Wang, J.; Antony, A.; Taniguchi, T.; Watanabe, K.; Heinz, T. F.; Strauf, S.; Zhu, X.-Y.; Hone, J. C. *2D Materials* **2017**, *4*, 031011.
- (67) Wierzbowski, J.; Klein, J.; Sigger, F.; Straubinger, C.; Kremser, M.; Taniguchi, T.; Watanabe, K.; Wurstbauer, U.; Holleitner, A. W.; Kaniber, M.; Müller, K.; Finley, J. J. *Scientific Reports* **2017**, *7*, 12383.
- (68) Zhang, X.; Xu, C.; Zou, Z.; Wu, Z.; Yin, S.; Zhang, Z.; Liu, J.; Xia, Y.; Lin, C.-T.; Zhao, P.; Wang, H. *Carbon* **2020**, *161*, 479–485.
- (69) Allard, C.; Schué, L.; Fossard, F.; Recher, G.; Nascimento, R.; Flahaut, E.; Loiseau, A.; Desjardins, P.; Martel, R.; Gauffrès, E. *Advanced Materials* **2020**, *32*, 2001429.
- (70) Tran, T. T.; Kianinia, M.; Nguyen, M.; Kim, S.; Xu, Z.-Q.; Kubanek, A.; Toth, M.; Aharonovich, I. *ACS Photonics* **2018**, *5*, 295–300.
- (71) Konthasinghe, K.; Chakraborty, C.; Mathur, N.; Qiu, L.; Mukherjee, A.; Fuchs, G. D.; Vamivakas, A. N. *Optica* **2019**, *6*, 542.
- (72) Ngoc My Duong, H.; Nguyen, M. A. P.; Kianinia, M.; Ohshima, T.; Abe, H.; Watanabe, K.; Taniguchi, T.; Edgar, J. H.; Aharonovich, I.; Toth, M. *ACS Applied Materials & Interfaces* **2018**, *10*, 24886–24891.
- (73) Fournier, C.; Plaud, A.; Roux, S.; Pierret, A.; Rosticher, M.; Watanabe, K.; Taniguchi, T.; Buil, S.; Quélin, X.; Barjon, J.; Hermier, J.-P.; Delteil, A. *Nature Communications* **2021**, *12*, 3779.

- (74) Akbari, H.; Biswas, S.; Jha, P. K.; Wong, J.; Vest, B.; Atwater, H. A. *Nano Letters* **2022**, *22*, 7798–7803.
- (75) Somaschi, N.; Giesz, V.; De Santis, L.; Loredano, J. C.; Almeida, M. P.; Hornecker, G.; Portalupi, S. L.; Grange, T.; Antón, C.; Demory, J.; Gómez, C.; Sagnes, I.; Lanzillotti-Kimura, N. D.; Lemaitre, A.; Auffeves, A.; White, A. G.; Lanco, L.; Senellart, P. *Nature Photonics* **2016**, *10*, 340–345.
- (76) Hayee, F.; Yu, L.; Zhang, J. L.; Ciccarino, C. J.; Nguyen, M.; Marshall, A. F.; Aharonovich, I.; Vučković, J.; Narang, P.; Heinz, T. F.; Dionne, J. A. *Nature Materials* **2020**, *19*, 534–539.
- (77) Mendelson, N.; Doherty, M.; Toth, M.; Aharonovich, I.; Tran, T. T. *Advanced Materials* **2020**, *32*, 1908316.

6

A DOUBLE-RESONANCE EXPERIMENT ON PERYLENE

In this chapter, I will lay out a theoretical and experimental framework for the detection of a resonance of a very weak singlet-to-triplet transition, where the region to look for this resonance is deduced from the phosphorescence spectrum in Chapter 3. Compared to other host/guest systems, the case of perdeuterated perylene in dibenzothiophene is complicated by an additional parameter, namely reverse intersystem crossing (rISC). I will show that rISC can be both helpful and problematic in this experiment and I will show how future experiments could be designed.

6.1. INTRODUCTION

6.1.1. EXPERIMENTS ON TRIPLET STATES

Since the detection of phosphorescence from triplet states is experimentally difficult, no experiments have been done on the excitation of triplet states from the ground state on single molecules. However, the stochastic intersystem crossing to the triplet state, the difference in the lifetimes of the three sublevels, the zero-field splitting between the states and highly-allowed transitions between triplet sublevels are such that it is possible to detect transitions *between* triplet sublevels. These transitions are generally captured by changes in the fluorescence signal as a function of a microwave excitation source, performed in a scheme called optically-detected magnetic resonance (ODMR). The first experiments on a single-molecule level, in 1993,^{1,2} were already shortly conducted after the fluorescence signal from single molecules was detected for the first time in 1990.³ In both works, the experiments were performed on single pentacene molecules in a *p*-terphenyl host matrix. A few years later, the first hyperfine-coupled nuclear spin of a carbon-13 atom was detected in the ODMR signal for the same pentacene.⁴ Nowadays, ODMR is a common technique for reading out spin transitions in other systems, which typically allow for room-temperature operation, such as NV centers in diamond⁵ and more recently, spin centers discovered in hexagonal boron nitride.⁶ The latter two systems are different from single molecules in the sense that their ground state is already a triplet. Hence, no intersystem crossing or weak resonance to a spin state have to be involved. Systems such as NV centers have shown efficient coupling and control over many nuclear spins, where in extreme cases up to 50 nuclear spins could be mapped around an NV center.⁷ Unlike singlet states, triplet states can be employed as nanosensors of magnetic field.⁸

Recently, there has been some renewed interest in the manipulation of spins in single molecules, due to the versatility and diversity of molecular systems. Recent work consists for instance on spin manipulation in ensembles of rare-earth Eu^{3+} molecular complexes,⁹ organic radical molecules¹⁰ and, interestingly, also by atomic force microscopy on the good old pentacene.¹¹ One of the key benefits of using a neutral aromatic molecule with a singlet ground state for spin manipulation, in special that of hyperfine-coupled nuclear spins, is that the electron spin can be turned off by de-excitation. In that case, the electron spin will not be a source of decoherence anymore for the nuclear spin, which could potentially increase the nuclear spin's coherence time, of particular uses for quantum memories. Moreover, molecular crystals are easily prepared and transferred. Furthermore, molecular crystals can be well implemented into photonic structures¹² and microcavities,^{13,14} while dielectric antennas can boost collection efficiencies of photons close to unity.¹⁵ All these properties make molecular systems attractive candidates for spin-photon interfaces.

Before such a spin-photon interface with single molecules can be realized, the coherent optical control of spin states has to be experimentally proven. In chapter 3, we recorded the phosphorescence spectrum of perdeuterated perylene in order to pin-point the spectral region where the weak resonance for the singlet-to-triplet transition would be located. In this chapter, I will report on the experiments that we set up to find this

resonance and the experimental challenges that come with it, such as the influence of reverse intersystem crossing.

6.1.2. THEORETICAL DESCRIPTION OF A THREE-LEVEL SYSTEM

The fluorescence and phosphorescence studies of perdeuterated perylene (to be called perylene-d12 from now on) in dibenzothiophene, in respectively Chapter 2 and Chapter 3, have made it possible to select a spectral region for a double optical resonance experiment on a single perylene-d12 molecule. The scheme for this experiment, shown in Figure 6.1, is similar to optically-detected magnetic resonance experiments, but with the major difference that the approach is entirely optical and initiated from the ground state. An alternative to initiation from the ground state is, in analogy to atomic physics, the so-called Λ -scheme, where the singlet-to-triplet transition is initiated from the singlet excited state, thus $S_1 \rightarrow T_1$. Given the energy of the singlet excited state and the energy of the triplet state, deduced respectively from the fluorescence and phosphorescence spectra, the $S_1 - T_1$ energy gap would be approximately $9,261 \text{ cm}^{-1}$ (vacuum) or $1,080 \text{ nm}$ (air). The considerably shorter wavelength for the $S_0 - T_1$ energy gap, namely around 784 nm , is experimentally easier to work with in combination with blue light for the $S_0 \rightarrow S_1$ transition. Hence, we will work with the scheme that is initiated from the ground state, called the V-scheme. In the V-scheme, a probe laser produces coherent cycles between the ground singlet and excited singlet state, which results in a measurable fluorescence signal. A pump laser scans the near-infrared (NIR) region for the spin-forbidden transition from the ground singlet state to the triplet state. This NIR region was determined in chapter 3 by the measured phosphorescence spectrum of perylene in the dibenzothiophene host in a region of interest determined by the inhomogeneous broadening around the 0-0 zero-phonon line. As a function of the NIR laser's frequency, the fluorescence signal may decrease or increase in intensity, depending on the steady-state population of the triplet states. In addition, we cannot ignore contributions of reverse intersystem crossing (rISC), which incoherently reduces the population of the triplet when the probe laser strongly excites the molecule's singlet transition. Furthermore, we assume that the NIR beam itself does not influence the rISC rate. To obtain an idea of the influence of reverse intersystem crossing by the probe beam we have to consider the rate equations, including coherences, for this double-resonance experiment.

In principle, there are three triplet sublevels with each of them having different intersystem crossing rates and lifetimes, but for the sake of simplicity I will group them into a single level. The three-level system of coupled rate equations has the following matrix form:

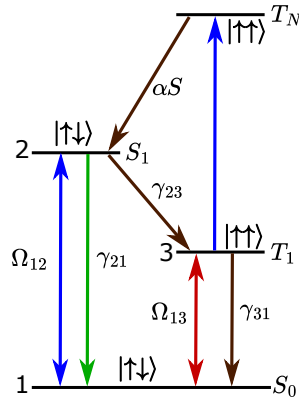


Figure 6.1.: Simplified Jablonski diagram of the three-level system, driven at resonance with the pump and probe laser. These resonances are indicated by a double arrow to account for stimulated emission. The relevant rates between the different levels are indicated next to the arrow. In addition, absorption from the probe laser to a higher triplet state is shown as the pathway for reverse intersystem crossing with total rate α proportional to the saturation parameter $S = I/I_s$ of the probe laser. The diagram is simplified in the sense that the three triplet sublevels are merged together.

6

$$\frac{d}{dt} \begin{bmatrix} p_{11} \\ p_{22} \\ p_{33} \\ p_{13} \\ p_{31} \\ p_{12} \\ p_{21} \end{bmatrix} = \begin{bmatrix} 0 & +\gamma_{21} & +\gamma_{31} & -\frac{1}{2}i\Omega_{13} & +\frac{1}{2}i\Omega_{13} & -\frac{1}{2}i\Omega_{12} & +\frac{1}{2}i\Omega_{12} \\ 0 & -\gamma_{21} - \gamma_{23} & +\alpha I & 0 & 0 & +\frac{1}{2}i\Omega_{12} & -\frac{1}{2}i\Omega_{12} \\ 0 & +\gamma_{23} & -\gamma_{31} - \alpha I & +\frac{1}{2}i\Omega_{13} & -\frac{1}{2}i\Omega_{13} & 0 & 0 \\ -\frac{1}{2}i\Omega_{13} & 0 & +\frac{1}{2}i\Omega_{13} & -\pi\Gamma_{13} & 0 & 0 & 0 \\ +\frac{1}{2}i\Omega_{13} & 0 & -\frac{1}{2}i\Omega_{13} & 0 & -\pi\Gamma_{13} & 0 & 0 \\ -\frac{1}{2}i\Omega_{12} & +\frac{1}{2}i\Omega_{12} & 0 & 0 & 0 & -\pi\Gamma_{12} & 0 \\ +\frac{1}{2}i\Omega_{12} & -\frac{1}{2}i\Omega_{12} & 0 & 0 & 0 & 0 & -\pi\Gamma_{12} \end{bmatrix} \begin{bmatrix} p_{11} \\ p_{22} \\ p_{33} \\ p_{13} \\ p_{31} \\ p_{12} \\ p_{21} \end{bmatrix} \quad (6.1)$$

The vectors contain the density matrix elements for the populations ρ_{11} , ρ_{22} and ρ_{33} of respectively the ground singlet, excited singlet and triplet states and the coherences captured in ρ_{13} , ρ_{31} , ρ_{12} and ρ_{21} . The parameters Ω_{12} and Ω_{13} are the Rabi frequencies of the $S_0 \rightarrow S_1$ and $S_0 \rightarrow T_1$ transitions. Furthermore, Γ_{12} and Γ_{13} are the homogeneous linewidths of both transitions, and are related to the decoherence times by $1/T_{2,12} = \pi\Gamma_{12}$ and $1/T_{2,13} = \pi\Gamma_{13}$. The rate γ_{21} is the decay rate of the excited singlet state, γ_{23} the intersystem crossing rate, γ_{31} the decay rate of the triplet and lastly, αI is the incremental decay rate of the triplet state due to reverse intersystem crossing, which is a function of the saturation parameter S of the probe laser. All detuning terms are ignored, as we plan to work at resonance. In Table 6.1, relevant parameters for equation 6.1 are listed. Most parameters have been acquired in our own experiments, but the linewidth of the $S_0 \rightarrow T_1$ transition has to be assumed. Although linewidths have been measured for ODMR transitions between triplet sublevels, nothing is known about the linewidth of an $S_0 \rightarrow T_1$ transition. Hence, we have to make the

assumption that the linewidth for the $S_0 \rightarrow T_1$ transition is similar to what is measured for transitions between triplet sublevels by ODMR. This, however, might not be true as ODMR transitions do not involve a change in molecular orbital. This, in principle, makes the $S_0 \rightarrow T_1$ transition sensitive to spectral diffusion that perturbs the $S_0 - T_1$ energy gap, on probably a similar timescale as for the $S_0 \rightarrow S_1$ transition. Assuming this spectral diffusion is negligible, the linewidth of the $S_0 \rightarrow T_1$ transition is given by the decoherence time $T_{2,13}$. In ODMR, the measured linewidth for hydrogenated molecules is typically in the order of a few MHz, while for deuterated molecules, the linewidth can narrow down to 100 kHz.⁴ This is, however, not the homogeneous linewidth, because the measured linewidth is affected by slow spin dynamics (spectral diffusion) that broadens the linewidth during the relatively long acquisition times of an ODMR spectrum (in the order of seconds¹⁶). However, the homogeneous linewidth can be deduced from measurements on the decoherence time. Recently, the decoherence time was measured by atomic force microscopy (AFM) and was found for hydrogenated pentacene to be around $2.2 \pm 0.3 \mu\text{s}$, extending up to $16 \pm 4 \mu\text{s}$ for deuterated pentacene.¹¹ Earlier pulse-sequence¹⁷ and Hahn-echo¹⁸ measurements confirm the $T_{2,13}$ found for hydrogenated pentacene with AFM. The measurements of the decoherence time indicate that the homogeneous linewidth of transitions between triplet sublevels is in the order of 150 kHz for hydrogenated pentacene and 20 kHz for deuterated pentacene, whereas the observed linewidths, respectively a few MHz and a few 100 kHz, are significantly broadened by spectral diffusion.

γ_{21} (s^{-1})	γ_{23}^{xy} (s^{-1})	γ_{23}^z (s^{-1})	γ_{31}^{xy} (s^{-1})	γ_{31}^z (s^{-1})	α (s^{-1})/ S	Γ_{12} MHz	Γ_{13} kHz
2.2×10^8	532	46	118	16	18	~ 58	~ 20

Table 6.1.: Parameters included in the system of rate equations. All but the last parameter have been measured in experiment. The expected homogeneous linewidth of the transition to the triplet state is estimated from a decoherence time measurement of deuterated pentacene for transitions between triplet sublevels.¹¹ The dominant ISC rates and decay rates of the xy-triplet substates are used as values for γ_{23} and γ_{31} in equation 1.

The system of rate equations (equation 6.1) can be solved using the Laplace transform and this was done in MATLAB. The solutions for the populations are so lengthy that I will not display them here, but rather go directly to the results using the parameters displayed in Table 6.1. The solution has two variables of interest, namely the Rabi frequencies, Ω_{12} , for the $S_0 \rightarrow S_1$ transition and, Ω_{13} , for the $S_0 \rightarrow T_1$ transition. In general, the Rabi frequency scales with the square root of the laser intensity, thus with the optical field's amplitude. The Rabi frequency as a function of the saturation parameter S , for the singlet transition, can be approximated by:

$$\Omega_{12}(S) = \sqrt{\gamma_{21}\pi\Gamma_{12}} \times \sqrt{S} \approx 201 \text{ MHz} \times \sqrt{S}. \quad (6.2)$$

The solutions in Figure 6.2 are expressed in terms of the saturation parameter S (ratio of I/I_s), which indicates the Rabi frequency Ω_{12} in units of 201 MHz (see equation

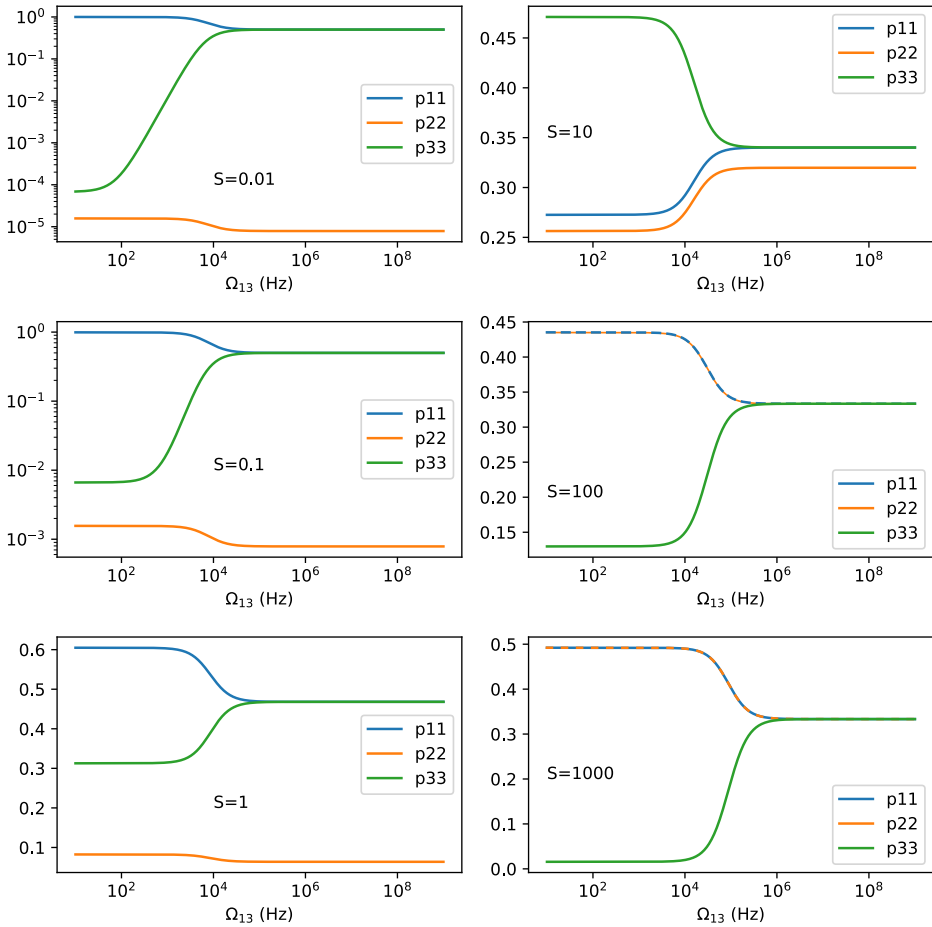


Figure 6.2.: Simulated fractions of populations of the three levels (their sum is always 1), where the triplet sublevels are grouped into a single level. The solutions have been processed for different levels of saturation for the singlet transition, given by the saturation parameter S , indicated in each figure panel. The Rabi frequency Ω_{12} as a function of the saturation parameter is determined by equation 6.2. At weak excitation, the population of the excited singlet is very low and therefore the populations are plotted on a log scale. At higher excitation intensities, starting from $S=1$, the populations are more comparable.

6.2). The saturation parameters, stretching from $S=0.01$ up to $S=1000$ are indicative of the experimentally attainable values, as measured in Figure 2.8 in Chapter 2. The

populations of the three levels are simulated as functions of how strongly we drive the $S_0 \rightarrow T_1$ transition and show where saturation of the triplet state occurs and in particular the effect it has on the excited state population ρ_{22} and thereby on the fluorescence signal. As a function of the saturation parameter S , there are three regimes that can be identified.

Regime 1. For the case of a weakly-excited molecule, thus $S \leq 0.1$ for Ω_{12} , the molecule spends most of the time in the ground state. In addition, intersystem crossing is not occurring frequently, as it grows linearly with the excited state population ρ_{22} . In that case, the coherent excitation of the triplet state would strongly increase the population, ρ_{33} of the triplet. Upon triplet excitation, the singlet excited state population is reduced and that leads to a decrease in the fluorescence signal. Of course, the model is simplified, and it is likely that the effect varies per triplet sublevel. Neglecting those variations per sublevel, the contrast of the $S_0 \rightarrow T_1$ transition's effect on the fluorescence can be up to 50% for $S=0.01$, decreasing slightly to 40% for $S=0.1$.

Regime 2. For the case of a moderately-excited molecule, thus $1 \leq S \leq 10$ for Ω_{12} , the higher saturation of the singlet excited state leads to strong intersystem crossing and a higher steady-state population for the triplet. At these excitation intensities, the effect of reverse intersystem crossing on the triplet state's population is still weak. Compared to regime 1, the effect of a coherent excitation of the triplet will now start to decrease the population in the triplet and in turn increases the fluorescence signal. The contrast in the fluorescence signal is relatively low, with only 10% for $S=1$ up to 20% for $S=10$.

Regime 3. For the case of a strongly-excited molecule, thus $S \geq 100$ for Ω_{12} , the effects of reverse intersystem crossing start to become noticeable. In steady state, the population of the triplet starts much lower due to shortened lifetimes. The coherent excitation of the triplet will, however, increase the population again and will therefore lower the fluorescence signal. The contrasts in the fluorescence signal are about 23% for $S=100$ and 32% for $S=1000$. For even higher excitation intensities, the populations of all three levels will equalize at a strong coherent excitation of the triplet. Hence, the theoretical maximum for the contrast is 33.3%. However, an important consequence of reverse intersystem crossing is that the Rabi frequency at saturation of the triplet rises as the lifetime of the triplet is shortened. In this regime, a higher saturation parameter S , will require more light intensity to induce enough transitions to the triplet state, which might be experimentally challenging.

The simplified model that I presented here will likely most resemble the case of strong excitation, where all three triplet sublevels have practically equal lifetimes due to reverse intersystem crossing (single exponential decay in the autocorrelation of fluorescence). All in all, given the three regimes in the simulation, the contrast of triplet absorption in the fluorescence will likely be optimal when working at low light intensity for the probe beam, which avoids both reverse intersystem crossing and strong intersystem crossing. However, the intermittent blinking of the fluorescence, with long duration times, will in

turn require relatively long averaging times of the fluorescence signal, as I will show in the next section.

6.1.3. EXPERIMENTAL CONDITIONS: CONTINUOUS WAVE EXCITATION

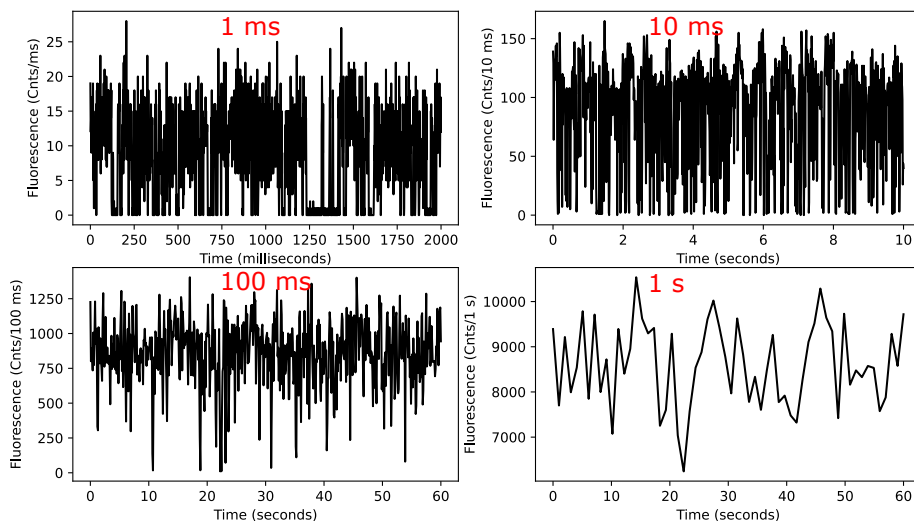


Figure 6.3.: Fluorescence signal from a single molecule, excited resonantly at $S=0.1$ and sampled to different time domains of 1 ms up to 1 s. Frequent blinking of the fluorescence due to intersystem crossing persists up to sampling rates of 10 Hz. Even at 1 sample per second the fluorescence signal fluctuates up to 20% around the mean. At 10 ms there are some periodic fluctuations present that might be due to external vibrations that couple to the cryostat.

There are two experimental routes for the double-resonance experiment. The simplest is to work in a continuous wave (CW) regime, where both lasers beams are always on. This is the basis for the simulations in Figure 6.2, which are solved for steady state. Another possibility is to perform the experiment in a pulsed scheme. This could potentially avoid reverse intersystem crossing, as long as the probe pulses are shorter than the rISC rate. However, the pulsed scheme has the disadvantage that the probe beam is only on for a short time and therefore the fluorescence signal is relatively low. The disadvantage of the CW regime is that the fluorescence signal tends to naturally fluctuate due to intersystem crossing and these fluctuations can last up to 100 ms. Hence, the fluorescence signal needs to be collected at low sampling rates. In Figure 6.3, some examples of sampling rates are shown. The figure shows that a 1 Hz sampling rate leads to a signal that fluctuates with a standard deviation of approximately 10%, with some single deviations of up to 20%. Even with this signal, a weak resonance with low contrast could be easily missed. Below $S=1$, the contrast of the fluorescence dip would

be at best 50% in the case of the simplified three level scheme, with a saturated Ω_{13} . Of course, beyond saturation of the $S_0 \rightarrow T_1$ transition, the linewidth will be power broadened. This power broadening scales with the square root of the laser intensity as:

$$\Gamma(I) = \Gamma_0 \sqrt{1 + I/I_s}. \quad (6.3)$$

At this point it is not clear whether we can obtain significant power-broadened linewidths with the experimentally attainable intensities of the NIR laser, which is in the tens of mW range or, in best case focused to a diffraction-limited spot, amounts to about 1-10 MW/cm². To make a guess of the saturation intensity of the triplet in order to find out how much we can power-broaden the linewidth, given the assumption that the linewidths are similar to those found in ODMR experiments, we can consider the following expression for the saturation intensity:

$$I_{s,13} \propto \frac{\gamma_{31}\Gamma_{13}}{|\mu_{13}|^2}, \quad (6.4)$$

where μ_{13} is not introduced before and describes the transition dipole moment for the $S_0 \rightarrow T_1$ transition. From experiment, we know the saturation intensity of the $S_0 \rightarrow S_1$ transition and therefore we can directly compare their values:

$$\frac{I_{s,13}}{I_{s,12}} = \frac{|\mu_{12}|^2 \gamma_{31} \Gamma_{13}}{|\mu_{13} \gamma_{21} \Gamma_{12}|^2} \approx \frac{|\mu_{12}|^2}{|\mu_{13}|^2} \times \frac{25 \times 10^3 \text{ Hz}}{58 \times 10^6 \text{ Hz}} \times \frac{118 \text{ s}^{-1}}{2.2 \times 10^8 \text{ s}^{-1}}. \quad (6.5)$$

It helps that the assumed linewidth of the $S_0 \rightarrow T_1$ transition of approximately 25 kHz with respect to the 58 MHz of the $S_0 \rightarrow S_1$ transition reduces the ratio. Also, the low rate of γ_{31} as compared to γ_{21} works in our advantage and reduces the ratio. However, the transition to the triplet is forbidden and therefore has a weaker transition dipole moment. An experiment on $S_0 \rightarrow T_1$ absorption for pure perylene crystals found an estimated oscillator strength of 10^{-10} ,¹⁹ which is proportional to the square of the transition dipole moment. The same group also estimated the oscillator strength of the $S_0 \rightarrow S_1$ transition of perylene to be around 0.44²⁰ and therefore we have 10 orders of magnitude difference. With these numbers we obtain a ratio of the saturation intensity for the T_{xy} triplet sublevels as compared to the saturation intensity of the singlet of about a factor 0.8, which makes them practically equal. For the T_z triplet sublevel the ratio would be 0.11. Physically this makes sense: although the transition is very weak, only a limited number of absorbed photons are necessary to saturate the level, because it is much longer lived than the singlet excited state. In addition, if the transition is very narrow this enhances absorption, as long as the laser linewidth is comparable or narrower. However, if there would be significant broadening of the homogeneous linewidth, to a value similar for the $S_0 \rightarrow S_1$ transition, the ratio would be around 2,400. With the power densities available of up to 1-10 MW/cm² as compared to the saturation intensity of the singlet of 22 W/cm² (see Chapter 2), we can supply 4-5 orders of magnitude higher intensities. This could broaden the transition by 100-300 times, leaving us in best case with a linewidth of 4.7-15 MHz for the T_{xy} triplet sublevels and 13-40 MHz for the T_z triplet substate. With a laser of 100 kHz linewidth (see section 6.2) and similar scan resolution per measurement point we could therefore pinpoint this transition out of the natural fluctuations present in the fluorescence signal. Of course, the

above argument, based on the assumption that the homogeneous linewidth is around 20 kHz, only works when rISC is negligible, because it increases the rate of γ_{31} and thus increases the amount of laser power that is necessary to obtain saturation of the triplet.

6.1.4. PULSED EXCITATION

To eliminate random fluctuations due to intersystem crossing (ISC) from the data, we could as an alternative method resort to pulsed excitation. In this case, the singlet transition is shortly excited and fluorescence is collected in the same time window. When photons are measured, the molecule is likely not in the triplet state. Hence, we can supply a pulse of NIR light to try to excite the triplet state. Subsequently, we can supply another pulse of blue light and measure if we are in the triplet state again, as then there would be no photons coming out if that would be the case. The duration of the blue pulse length should however be long enough to collect enough photons from fluorescence, while avoiding rISC, which is probably in the 1-100 μ s regime. With these pulse durations and excitation beyond saturation, we can record 0.5-50 photons for each pulse on average.

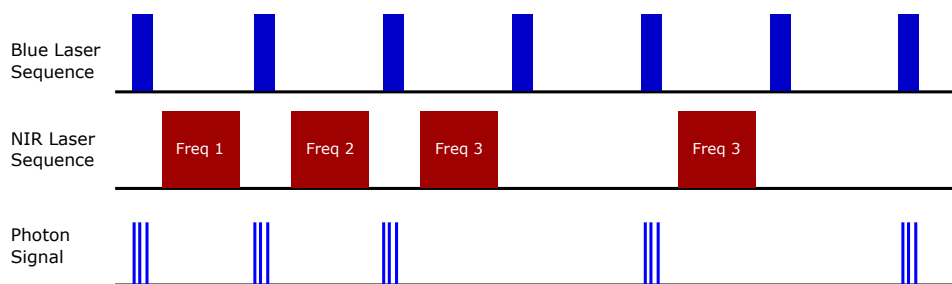


Figure 6.4.: Proposed sequence of pulses to detect a resonant transition to the triplet state. The blue laser pulse measures if the molecule is in the ground state by inducing fluorescence. With the NIR pulse we try to induce a transition to the triplet state. If the NIR pulse is at resonance with the triplet state, the subsequent blue pulse shouldn't generate any photon.

The duration of the NIR pulse is more difficult to determine, as it depends on the Rabi frequency that we obtain with the light intensity that we use. At saturation, the Rabi frequency of the triplet would be in the same manner as for the singlet, calculated to be around 2.7 kHz for the T_{xy} states and 1.0 kHz for the T_z state (equation 6.2). When we would have laser intensities of 1-10 MW/cm², the Rabi frequency would amount to 0.65-2 MHz for the T_{xy} states and also 0.65-2 MHz for the T_z state. Therefore, the frequency scale of the pulse can possibly be made shorter than the decoherence rate of around 62.5 kHz ($=\pi\Gamma_{13}$). For these very short pulses, the pulse length could fit integer multiples of a π -pulse + $2n\pi$ (additional Rabi cycles) and then the molecule would end up in the triplet state at the end of the pulse. However, if the pulse fits $2n\pi$ Rabi cycles,

the system would end up in the ground state. With effective π -pulses, we could obtain the best contrast in the signal. However, it is difficult to experimentally determine the Rabi frequency, without knowing anything yet about the coherent interaction of the NIR laser with the triplet state. Therefore it is best to employ a pulse duration that is significantly longer than the decoherence time (around 16 μ s). In that case, we firstly prevent that we unintentionally choose a pulse length that effectively de-excites the molecule and secondly, we prevent the case where our Rabi frequency would be overestimated and thus too low to excite the molecule into the triplet at all. However, for long pulses the contrast would be only 50%, as the molecule will be half the time in the excited triplet and half the time in the ground state at the end of the pulse.

Building up a setup that involves the use of pulses can be convenient for later experiments, once the resonances of the triplet are found, that use pulse sequences to probe the coherence properties of the triplet. However, coherence properties of the triplet states can also be measured in continuous wave using time-correlated single-photon counting, i.e. an antibunching histogram. Overall, a continuous-wave experiment is easier to setup and will therefore be part of the next section.

6.2. EXPERIMENTAL DETAILS

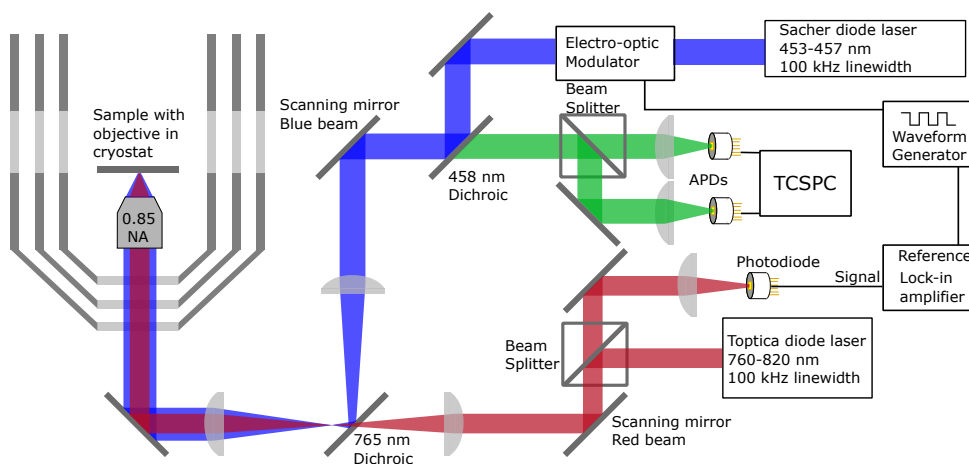


Figure 6.5.: Schematic of the experimental setup for the double-resonance experiment. The blue and red laser beam are combined at the 765 nm dichroic mirror and directed towards the objective in the cryostat. The avalanche photodiodes (APD's) collect fluorescence from the blue beam and the photodiode recovers the scattered light from a particle or gold film and transmits this signal to a lock-in amplifier. The blue beam can be modulated or pulsed using an electro-optic modulator. Both beams also have their own scanning mirrors for making small adjustments.

Whether we would resort to CW or pulsed excitations does not matter much for the basic experimental setup. In the experiment, the blue (Sacher diode laser 454-457 nm tunable range, 100 kHz linewidth) and near-infrared (NIR) laser (Toptica DL Pro HP, 760-820 nm tuning range, 100 kHz linewidth) beam will have to be focused onto the molecule to make sure that we can obtain the highest laser power densities possible. The required wavelengths for the two lasers, which are 454 nm and 784 nm, are quite far from each other and therefore we have to make sure that they are well overlapped in the focal plane and therefore are corrected for chromatic aberrations present in the optics. The overlapping of the two beams can be done through imaging of a small diffraction-limited particle, while trying to overlap the two images by moving one of the beams. Other methods include the use of pump-probe techniques. We considered using two-photon absorption, but the combination of photons from the two beams is in the ultraviolet (UV), which is not the right spectral region for our objective when we would have to collect UV fluorescence. Another possibility is the use of photothermal microscopy, but this principle has only been proved to work close to room temperature due to the required presence of a liquid. Fortunately, the effects of temperature on the alignment of our confocal setup are limited, as we always align at room temperature and directly use the setup for low temperature, without any further adjustments. Therefore we equipped the setup with components that make photothermal imaging possible. Figure 6.5 shows a schematic of the setup that we constructed. To maximize the excitation power and increase the amount of collected fluorescence we make use of dichroic mirrors, where a dichroic mirror at 458 nm (FF458-Di02-25x36, Semrock) passes the red-shifted fluorescence from perylene. The two laser beams are combined at a 765 nm long pass dichroic mirror (FF765-Di01-25x36x2.0, Semrock), which transmits the NIR light, but reflects the blue and fluorescence from perylene. Both laser beams have their own scanning mirror (Newport FSM-200) and therefore slight adjustments can be made for each beam separately. For the alignment procedure, we included an electro-optic modulator (Model 370 from Conoptics, controlled by a high-voltage amplifier DIV 20 from Qioptiq, which amplifies the signal from a waveform generator from Tektronix) in the beam path of the blue beam, which acts as the pump beam. With this EOM we can turn the beam on and off, to modulate heating of an object or surface, as part of the photothermal effect.²¹ In turn, we can also use this EOM to generate pulses for the pulsed excitation scheme. The NIR beam is directed to a photodiode, which measures the scattered light intensity from a particle that is being transiently heated by the pump beam. The modulated heating on the particle creates a modulated diffusion of heat around the particle and in turn modulates the refractive index of the immersion oil (Olympus, Type-F, $n=1.518$) around the particle. Changes in the immersion fluid's refractive index modifies the amount of light scattered from the particle. The signal of the scattered light onto the photodiode is connected to a Lock-in amplifier (SR844 from Stanford Research Systems), which extracts the photothermal signal in a narrow bandwidth around the modulation frequency. The amplitude of the lock-in signal is then a measure of the photothermal effect. By walking the two laser beams, we can find the maximum of this effect and that will be at the point where the two beams are well overlapped.

As the power of the blue laser is limited, the photothermal signal was rather weak, which in addition was lower due to the weak collection efficiency of the air objective (0.85 NA). The weak signal made it difficult to measure a photothermal signal from single, rather big, 80 nm gold spheres. However, the photothermal signal could be obtained on clusters of these spheres and on a 300 nm thick gold film. To obtain a good signal to noise for the photothermal signal, we used a gold film on glass, covered with another glass slip. At the interface we put a layer of immersion oil as the medium.

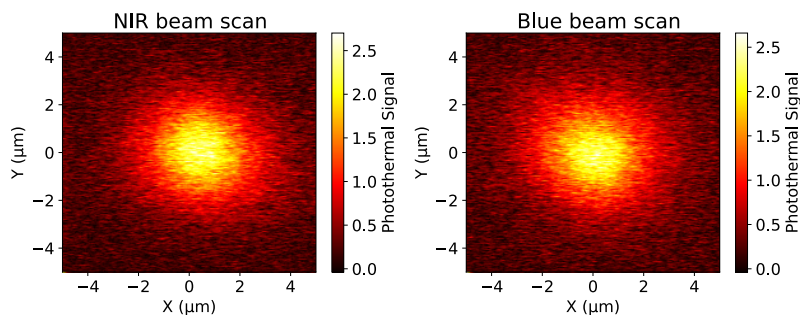


Figure 6.6.: Photothermal images of a gold film, measured at room temperature. The blue laser intensity is $80 \mu\text{W}$ at a 1 MHz modulation frequency and the NIR laser around 1 mW. The left image corresponds to a fixed blue beam (heating beam) and a scanned NIR beam (probe beam). On the right, the NIR beam is fixed and the blue beam is scanned. The images show a Gaussian point spread function with a width of about $2 \mu\text{m}$.

6.3. RESULTS AND DISCUSSION

6.3.1. EXPERIMENTS WITH STRONG REVERSE INTERSYSTEM CROSSING

Due to the limited time for experiments left before the end of my PhD trajectory, we decided to start the experiment in a simple way by profiting from the enhanced stability of the fluorescence signal by reverse intersystem crossing. A positive effect of rISC is that the fluorescence signal is steady, even for much shorter integration times compared to the necessary integration time of up to 1 second in Figure 6.3, in the case of weak excitation of the singlet. Moreover, the broader linewidth limits the influence of weak spectral diffusion, while the laser's frequency remains fixed (Figure 6.7). This also makes it unnecessary to employ a feedback algorithm that keeps the laser in resonance with the molecule. However, the negative effect is that the saturation intensity of the transition to the triplet increases as the triplet lifetime is reduced. Assuming that we have enough laser intensity available, this is not necessarily a bottleneck.

To make sure that we only have a single emitter present with good single-photon statistics and coherence properties, we can record the antibunching histogram of the

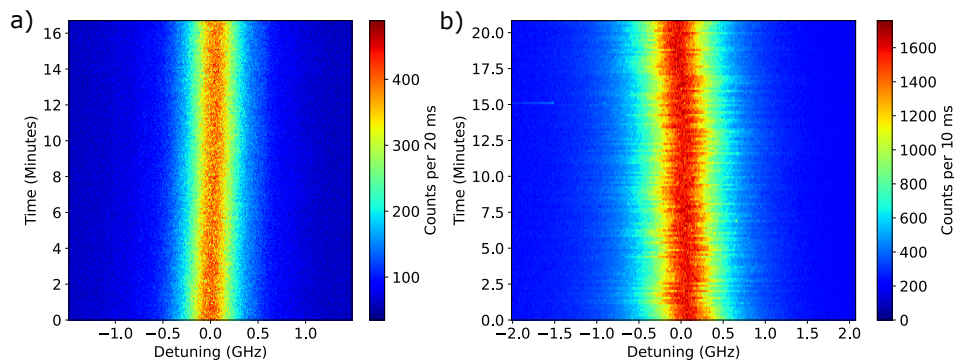


Figure 6.7.: Examples of time traces of excitation spectra, taken at high excitation intensities. The colors in the heatmap are relatively uniform due to shortened shelving in the triplet state. The molecule in panel (a) has a linewidth broadened to 496 MHz, at about 100 times saturation intensity. The molecule in panel (b) has a linewidth of 770 MHz, at about 225 times the saturation intensity. This molecule has a particularly uniform color in the excitation spectra, given that the integration time is only 10 ms and indicates very short dwell times in the triplet state. With the highest excitation intensity available, we could reduce triplet lifetimes down to 60 μs .

6

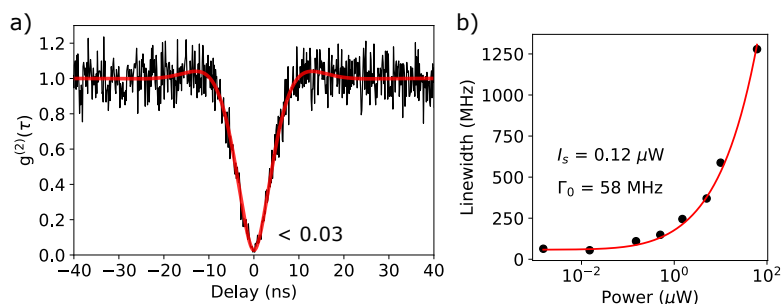


Figure 6.8.: Panel (a) shows an antibunching histogram at a low excitation intensity, showing a high single-photon purity with $g^{(2)}(0) < 0.03$. The fitted Rabi frequency Ω_{12} is around 200 MHz. Panel (b) shows linewidth broadening of a single perylene-d12 molecule at a range of excitation intensities. The fitted saturation intensity I_s , obtained by the of the experimental data to equation 6.3, amounts to $0.12 \pm 0.01 \mu\text{W}$.

fluorescence signal at resonance with the 0-0 ZPL. At low excitation intensities, we can limit the influence of background and obtain a high single-photon purity of more than 97%, as shown in Figure 6.8a. Furthermore, at high excitation intensities we can

observe clear Rabi oscillations in the photon statistics (Figure 6.9). This allows the extraction of the Rabi frequency, Ω_{12} , using equation A.8 in Appendix 1. The excitation intensities in the figure can be related to the saturation intensity extracted from the linewidth broadening curve in Figure 6.8b. The Rabi frequency at saturation is then estimated to be around 200 MHz for Figure 6.9c and 6.9d, which due to higher laser intensities have lower uncertainties in the measured laser power. This corresponds well to the calculated value in equation 6.2, which, based on intramolecular rates, states that the Rabi frequency at saturation is around 201 MHz. The homogeneous linewidth is 58 MHz, similar to the narrowest linewidths found for perylene-d12 in dibenzothiophene (see also Chapter 2).

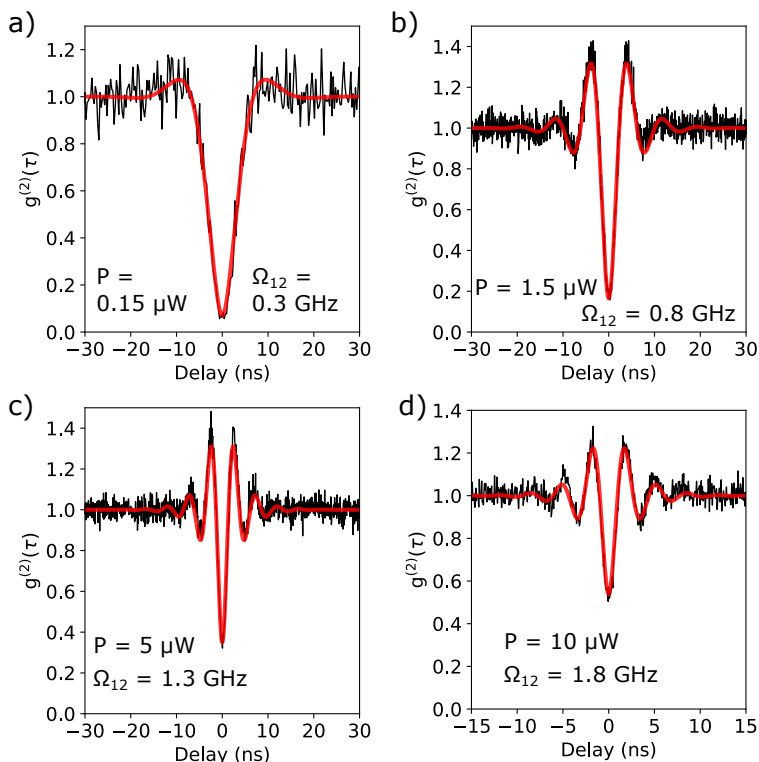


Figure 6.9.: Series of antibunching histograms of a single molecule, taken at increasing excitation intensities. Higher excitation intensities are possible, but the Rabi oscillations and dip will not be visible anymore due to uncertainty in the timing resolution caused by jitter of the detector (documented to be around 350 ps).

In experiments, it turned out to be a challenge to find a molecule that stays in resonance with the laser for more than a minute while the linewidth is (near) lifetime limited. However, a power-broadened linewidth in the order of 500 MHz was almost always enough to keep a steady resonance without additional feedback. The observed

spectral diffusion could be caused by the poor crystallization of the host through freeze-quenching, which could be improved by sublimation techniques or perhaps low-temperature annealing.

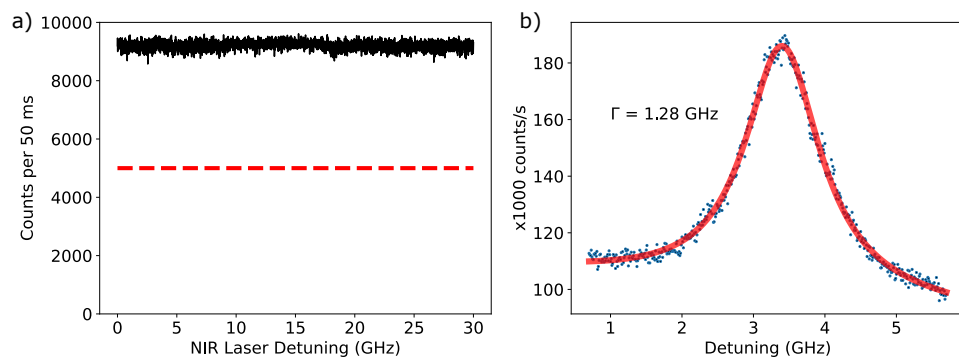


Figure 6.10.: a) Fluorescence signal of a single perylene-d12 molecule recorded at resonance with the 0-0 ZPL at a high excitation intensity ($S \approx 486$), while the NIR laser is scanned over 30 GHz. The background signal (red dashed line) amounts to a relatively high 100 kcnt/s, while the fluorescence signal (black data) is around 80 kcnt/s. The fluorescence signal is very stable within the relatively short integration time of 50 ms due to strong reverse intersystem crossing. No resonance with the triplet was detected in this scan. Panel (b) shows the Lorentzian profile of the molecule in panel (a). The strong excitation power-broadens the linewidth to 1.28 GHz, which from the homogeneous linewidth of about 58 MHz amounts to a saturation parameter $S \approx 486$. Given that rISC typically scales with a rate of 18 s^{-1} as factors of S , triplet lifetimes have probably reduced to around 110 μs .

As shown in Figure 6.10, the integration time of the fluorescence, recorded at resonance, can be scaled down to 50 ms, or perhaps less, without significant drops in fluorescence present. This is very different from the situation displayed in Figure 6.3, which describes the case of a weak excitation of the 0-0 ZPL. Unfortunately, we were not able to detect a resonance within a larger scan of more than 2 nm around the center of the inhomogeneous broadening of the 0-0 ZPL found in the phosphorescence spectrum, shown in Figure 6.11. The measurement shows that it is possible to remain at resonance with the 0-0 ZPL of the singlet transition for up to 2 hours (total scan duration) without inducing spectral diffusion due to the high intensity light of about 2 MW/cm^2 . At saturation of the triplet, a maximum contrast of 33 % is expected, yet no dip in the fluorescence signal is more significant than 10 %. There are some upward jumps present in the fluorescence signal, but they were not reproducible and might have originated from spectrally-diffusing molecules that intermittently jumped into resonance with the laser.

Compared to the usual saturation intensity of 22 W/cm^2 for the singlet, the intensity of 2 MW/cm^2 is a factor 10^5 higher. The linewidth could therefore, focusing on the T_{xy} triplet substates amount to 6.7 MHz , taking into account that the saturation intensity of the triplet is about a factor 0.8 compared to the singlet (equation 6.4). However, this value is based on the case without rISC and moreover, this only applies when both laser beams are at the same focal point and all the NIR laser power is focused onto the molecule. At the broadened linewidth, displayed in Figure 6.10b, the triplet lifetimes have reduced to around $110 \mu\text{s}$. Hence, the saturation intensity will scale up as well. The ratio of the saturation intensity with rISC as compared to the case without rISC is calculated by:

$$R(S) = \frac{I_{s,with\ rISC}}{I_{s,without\ rISC}} = \frac{\gamma_{31} + \alpha S}{\gamma_{31}}. \quad (6.6)$$

With $S \approx 486$, the ratio is approximately 75 . Taking into account this adjusted saturation intensity, the used laser power is only 1700 times higher than the theoretical saturation intensity and translates into a broadened linewidth of only 0.8 MHz , at best conditions. Hence, the step size of 6 MHz in the scan is too large. Still the experimental data shows that the experiment is conceptually feasible and that a molecule can be measured for prolonged times at resonance with the 0-0 ZPL, without significant drifts in the fluorescence signal. This indicates that the setup is mechanically stable enough. Moreover, no spectral diffusion was observed on the singlet resonance, despite the large intensity of the NIR laser beam.

6.4. CONCLUSION AND OUTLOOK

In this chapter, we have reported on the theoretical framework of the double-resonance experiment and first trial experiments. Although the presence of reverse intersystem crossing can be helpful by reducing the integration time needed for each data point, due to the enhanced stability of the fluorescence signal, it can also be a limiting factor in the experiments. The presence of rISC increases the required intensity to saturate the transition to the triplet and may suppress broadening of the linewidth at the laser intensities that we have available. This may in turn require smaller incremental steps in the laser frequency and increase the duration of the NIR region scan, around the center of the inhomogeneous broadening found in the phosphorescence spectrum.

The long duration of the scan in Figure 6.11, which due to strong rISC should perhaps be taken at smaller incremental steps, would in future require automatization. Therefore it would be better to perform this experiment in a closed-cycle cryostat, which can maintain a low temperature for a longer time without having to intervene manually. The use of solid immersion lenses could also help to increase the laser power densities on the molecule and increase the fluorescence signal. It can also be helpful to further reduce the background fluorescence in the signal to increase the contrast of transitions to the triplet, which could probably be achieved by lowering the concentration of perylene molecules inside the crystals.

Another possibility is the use of hydrogenated perylene (perylene-h12), instead of

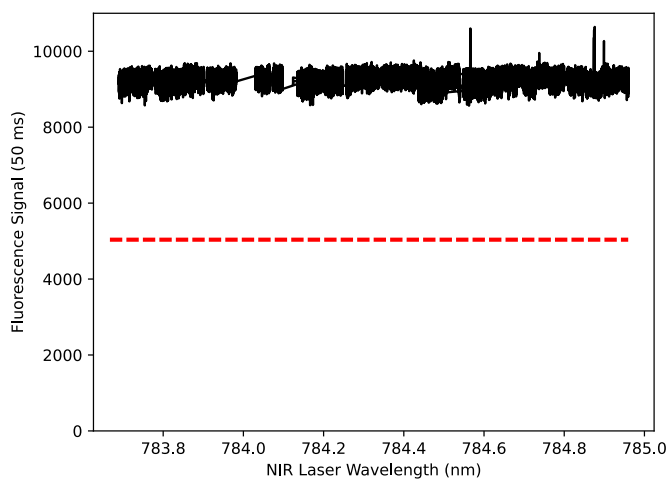


Figure 6.11.: Long range scan of the NIR laser with single-molecule fluorescence recorded at resonance with the 0-0 ZPL. The red dashed line represents the background level. There are sometimes gaps in the scan due to jumps in the laser. Peaks in the fluorescence were not reproducible and could be from spectrally-diffusing molecules. The scan was recorded with a 6 MHz resolution for the NIR laser, at a light intensity of 2 MW/cm^2 in a diffraction-limited spot of $1 \mu\text{m}$. The whole scan was recorded over a period of 2 hours.

6

perdeuterated perylene (perylene-d12). For perylene-h12, the linewidth is expected to be around 8 times broader due to the shorter decoherence time. However, the spectral sites of perylene-h12 may be shifted relative to those of perylene-d12, which was for instance measured to be in the order of tens of cm^{-1} for pentacene-h14 and pentacene-d14 in *p*-terphenyl.⁴ This may require a repetition of the phosphorescence experiment with perylene-h12.

REFERENCES

- (1) Köhler, J.; Disselhorst, J. a. J. M.; Donckers, M. C. J. M.; Groenen, E. J. J.; Schmidt, J.; Moerner, W. E. *Nature* **1993**, *363*, 242–244.
- (2) Wrachtrup, J.; von Borczyskowski, C.; Bernard, J.; Orrit, M.; Brown, R. *Nature* **1993**, *363*, 244–245.
- (3) Orrit, M.; Bernard, J. *Physical Review Letters* **1990**, *65*, 2716–2719.
- (4) Köhler, J.; Brouwer, A. C.; Groenen, E. J.; Schmidt, J. *Science (New York, N.Y.)* **1995**, *268*, 1457–1460.
- (5) Gruber, A.; Dräbenstedt, A.; Tietz, C.; Fleury, L.; Wrachtrup, J.; Borczyskowski, C. v. *Science* **1997**, *276*, 2012–2014.
- (6) Gottscholl, A.; Diez, M.; Soltamov, V.; Kasper, C.; Sperlich, A.; Kianinia, M.; Bradac, C.; Aharonovich, I.; Dyakonov, V. *Science Advances* **2021**, *7*, eabf3630.
- (7) Van de Stolpe, G. L.; Kwiatkowski, D. P.; Bradley, C. E.; Randall, J.; Breitweiser, S. A.; Bassett, L. C.; Markham, M.; Twitchen, D. J.; Taminiu, T. H. Mapping a 50-spin-qubit network through correlated sensing, 2023.
- (8) Taylor, J. M.; Cappellaro, P.; Childress, L.; Jiang, L.; Budker, D.; Hemmer, P. R.; Yacoby, A.; Walsworth, R.; Lukin, M. D. *Nature Physics* **2008**, *4*, 810–816.
- (9) Serrano, D.; Kuppusamy, S. K.; Heinrich, B.; Fuhr, O.; Hunger, D.; Ruben, M.; Goldner, P. *Nature* **2022**, *603*, 241–246.
- (10) Gorgon, S.; Lv, K.; Grüne, J.; Drummond, B. H.; Myers, W. K.; Londi, G.; Ricci, G.; Valverde, D.; Tonnelé, C.; Murto, P.; Romanov, A. S.; Casanova, D.; Dyakonov, V.; Sperlich, A.; Beljonne, D.; Olivier, Y.; Li, F.; Friend, R. H.; Evans, E. W. *Nature* **2023**, *620*, 538–544.
- (11) Sellies, L.; Spachtholz, R.; Bleher, S.; Eckrich, J.; Scheuerer, P.; Repp, J. *Nature* **2023**, *624*, 64–68.
- (12) Ren, P.; Wei, S.; Liu, W.; Lin, S.; Tian, Z.; Huang, T.; Tang, J.; Shi, Y.; Chen, X.-W. *Nature Communications* **2022**, *13*, 3982.
- (13) Wang, D.; Kelkar, H.; Martin-Cano, D.; Utikal, T.; Götzinger, S.; Sandoghdar, V. *Physical Review X* **2017**, *7*, 021014.
- (14) Pscherer, A.; Meierhofer, M.; Wang, D.; Kelkar, H.; Martín-Cano, D.; Utikal, T.; Götzinger, S.; Sandoghdar, V. *Physical Review Letters* **2021**, *127*, 133603.
- (15) Chen, X.-W.; Götzinger, S.; Sandoghdar, V. *Optics Letters* **2011**, *36*, 3545–3547.
- (16) Brown, R.; Wrachtrup, J.; Orrit, M.; Bernard, J.; von Borczyskowski, C. *The Journal of Chemical Physics* **1994**, *100*, 7182–7191.

- (17) Wrachtrup, J.; Von Borzyskowski, C.; Bernard, J.; Orrit, M.; Brown, R. *Physical Review Letters* **1993**, *71*, 3565–3568.
- (18) Wrachtrup, J.; von Borzyskowski, C.; Bernard, J.; Brown, R.; Orrit, M. *Chemical Physics Letters* **1995**, *245*, 262–267.
- (19) Clarke, R. H.; Hochstrasser, R. M. *Journal of Molecular Spectroscopy* **1969**, *32*, 309–319.
- (20) Hochstrasser, R. M. *The Journal of Chemical Physics* **1964**, *40*, 2559–2564.
- (21) Adhikari, S.; Spaeth, P.; Kar, A.; Baaske, M. D.; Khatua, S.; Orrit, M. *ACS Nano* **2020**, *14*, 16414–16445.

A

APPENDIX 1

The coincidence of photons on two detectors can be related to a steady-state solution of the following optical Bloch equations, where we ignore bunching due to the triplet state:¹

$$\dot{\rho}_{11} = \gamma_{21}\rho_{22} - \frac{i\Omega}{2}\rho_{12} + \frac{i\Omega}{2}\rho_{21} \quad (\text{A.1})$$

$$\dot{\rho}_{22} = -\gamma_{21}\rho_{22} + \frac{i\Omega}{2}\rho_{12} - \frac{i\Omega}{2}\rho_{21} \quad (\text{A.2})$$

$$\dot{\rho}_{12} = -\frac{i\Omega}{2}\rho_{11} + \frac{i\Omega}{2}\rho_{22} - \pi\Gamma_0\rho_{12} \quad (\text{A.3})$$

$$\dot{\rho}_{21} = \frac{i\Omega}{2}\rho_{11} - \frac{i\Omega}{2}\rho_{22} - \pi\Gamma_0\rho_{21}. \quad (\text{A.4})$$

The term Ω is the Rabi frequency, $\pi\Gamma_0$ is the decoherence rate and γ_{21} is the depopulation rate of the excited state. The series of coupled differential equations can be solved using the Laplace transform with the condition that the population initiates from the ground state. To relate the solution for the population of the excited state ρ_{22} to an experimental photon-coincidence histogram, we need to derive the steady-state solution of ρ_{22} :

$$g^{(2)}(\tau) = \rho_{22} / \lim_{\tau \rightarrow \infty} \rho_{22}. \quad (\text{A.5})$$

Without approximations and solved with MATLAB, the theoretical solution for $g^{(2)}(\tau)$ is of the following form:

$$g^{(2)}(\tau) = 1 - e^{-\frac{|\tau|}{2}(\pi\Gamma_0 + \gamma_{21})} [\cosh(\tilde{\Omega}|\tau|) + (\frac{\pi\Gamma_0 + \gamma_{21}}{2\tilde{\Omega}}) \sinh(\tilde{\Omega}|\tau|)], \quad (\text{A.6})$$

where $\tilde{\Omega}$ is given by:

$$\tilde{\Omega} = \frac{1}{2} \sqrt{(\pi\Gamma_0)^2 - 2\pi\Gamma_0\gamma_{21} - 4\Omega^2 + \gamma_{21}^2}. \quad (\text{A.7})$$

A

Rewriting $\tilde{\Omega} = \frac{1}{2}i\sqrt{4\Omega^2 - \gamma_{21}^2 - (\pi\Gamma_0)^2 + 2\pi\Gamma_0\gamma_{21}}$ and using the identities $\sinh(i\tilde{\Omega}) = -i\sin(\tilde{\Omega})$ and $\cosh(\tilde{\Omega}) = \cos(i\tilde{\Omega})$ we obtain the more common solution:²

$$g^{(2)}(\tau) = 1 - e^{-\frac{|\tau|}{2}(\pi\Gamma_0 + \gamma_{21})} [\cos(\tilde{\Omega}|\tau|) + (\frac{\pi\Gamma_0 + \gamma_{21}}{2\tilde{\Omega}}) \sin(\tilde{\Omega}|\tau|)], \quad (\text{A.8})$$

where the new $\tilde{\Omega}$ is $\frac{1}{2}\sqrt{4\Omega^2 - \gamma_{21}^2 - (\pi\Gamma_0)^2 + 2\pi\Gamma_0\gamma_{21}}$. When the two-level system is strongly excited, the magnitude of the Rabi frequency exceeds all other terms inside the square root and the term $\tilde{\Omega}$ in the cosine and sine term reduces to the Rabi frequency Ω itself.

REFERENCES

- (1) De Vries, H.; Wiersma, D. A. *The Journal of Chemical Physics* **1980**, *72*, 1851–1863.
- (2) Kummer, S.; Basche, T. *The Journal of Physical Chemistry* **1995**, *99*, 17078–17081.

ACKNOWLEDGEMENTS

In the four years that I have spent in the research group Molecular Nano-Optics and Spins (MoNOS) I have been well supported by my mentor prof. dr. Michel Orrit. His vast knowledge and insights on molecular physics and optics has been a great source of inspiration for me. I look back with gratitude for all the in-depth discussions that helped me during my PhD. I would like to specially thank him for his patience to explain everything in detail to me. On the experimental side, I would like to thank dr. Amin Moradi and dr. Zoran Ristanović for the extensive training they gave me for managing the lab and the experimental setup. They prepared me well for continuing on my own in the years after they left the group. Furthermore, I am thankful to have had the pleasure of working together fruitfully with students Maialen Ortego Larrazabal and Jil Hameury and the postdoc Arash Tebyani.

For the usage of fabrication facilities and the training for handling the equipment I want to thank Douwe Scholma, Marcel Hesselberth and Luc Wigbout. I'm also indebted to engineer and strongman Harmen van der Meer, who helped me lift up the heavy cryostat to repair one of the windows that had broken. Also, the electronics department has been of great help with solving various problems encountered with electronics. For achieving low temperatures I am grateful for Wilfred van der Geest's steady supply of liquid nitrogen and helium, which fueled my experiments.

For the nice lunch breaks, support and social meetings I would like to thank all of the (former) group members of MoNOS, which includes Arash, Amin, Christopher, Deep, Eduardo, Jacco, Jacqueline, Martin, Nasrin, Patrick, Priyanshi, Leonardo, Sergii, Subhasis, Theo, Xuxing, Zoran and Zohre. For all of the challenging administrative tasks, such as exporting a laser to the US for repair, I want to thank the group's secretary Henriëtte van Leeuwen for her support. Beyond the MoNOS group I would like to thank dr. Wolfgang Löffler and Matteo Fiscaro for kindly lending me their controller box for a laser and helping me use it. Within the institute I would like to thank dr. Semonti Bhattacharyya, prof. Sense Jan van der Molen, prof. Francesco Buda, Titus de Haas and prof. Jan van Ruitenbeek for participating in fruitful scientific discussions and collaborations. Outside of the institute I would like to thank prof. Bolesław Kozankiewicz, dr. Irena Deperasińska and prof. Jean-Sébastien Lauret for collaborations and scientific discussions.

Most of all I want to thank my partner and tower of strength Rolinde Hupkes. She has been my mental support throughout my PhD. Lastly, I also thank Limon for the many creative breaks!

CURRICULUM VITAE

Robert Smit

18-08-1990

Born in Velsen, the Netherlands

EDUCATION

2009–2013

Bachelor of Science in Physics
Leiden University

2013–2015

Master of Science in Physics and Science Based Business
Leiden University

February 2020 - March 2024

PhD in Physics
Leiden University

WORK EXPERIENCE

March 2015 –August 2015

Energy market analyst internship
Northpool B.V.

September 2015 – January 2020

Energy market trader and analyst
Brainchild Capital Investments B.V

March 2024 – Present

Postdoctoral researcher
Leiden University

LIST OF PUBLICATIONS

4. Smit, R.; Ristanović, Z.; Kozankiewicz, B.; Orrit, M. *ChemPhysChem* **2022**, *23*, e202100679
3. Smit, R.; Tebyani, A.; Hameury, J.; van der Molen, S. J.; Orrit, M. *Nature Communications* **2023**, *14*, 7960
2. Adhikari, S.; Smit, R.; Orrit, M. *The Journal of Physical Chemistry C* **2024**, *128*, 3–18
1. Smit, R.; Ristanović, Z.; Deperasińska, I.; Kozankiewicz, B.; Orrit, M. *ChemPhysChem*, e202300881